

033063

JPRS-CST-86-044

17 OCTOBER 1986

China Report

SCIENCE AND TECHNOLOGY

DISTRIBUTION STATEMENT A

Approved for public release;
Distribution Unlimited

DTIC QUALITY INSPECTED 4

FBIS

FOREIGN BROADCAST INFORMATION SERVICE

REPRODUCED BY
U.S. DEPARTMENT OF COMMERCE
NATIONAL TECHNICAL
INFORMATION SERVICE
SPRINGFIELD, VA. 22161

19981021 091

2
109
A06

NOTE

JPRS publications contain information primarily from foreign newspapers, periodicals and books, but also from news agency transmissions and broadcasts. Materials from foreign-language sources are translated; those from English-language sources are transcribed or reprinted, with the original phrasing and other characteristics retained.

Headlines, editorial reports, and material enclosed in brackets [] are supplied by JPRS. Processing indicators such as [Text] or [Excerpt] in the first line of each item, or following the last line of a brief, indicate how the original information was processed. Where no processing indicator is given, the information was summarized or extracted.

Unfamiliar names rendered phonetically or transliterated are enclosed in parentheses. Words or names preceded by a question mark and enclosed in parentheses were not clear in the original but have been supplied as appropriate in context. Other unattributed parenthetical notes within the body of an item originate with the source. Times within items are as given by source.

The contents of this publication in no way represent the policies, views or attitudes of the U.S. Government.

PROCUREMENT OF PUBLICATIONS

JPRS publications may be ordered from the National Technical Information Service, Springfield, Virginia 22161. In ordering, it is recommended that the JPRS number, title, date and author, if applicable, of publication be cited.

Current JPRS publications are announced in Government Reports Announcements issued semi-monthly by the National Technical Information Service, and are listed in the Monthly Catalog of U.S. Government Publications issued by the Superintendent of Documents, U.S. Government Printing Office, Washington, D.C. 20402.

Correspondence pertaining to matters other than procurement may be addressed to Joint Publications Research Service, 1000 North Glebe Road, Arlington, Virginia 22201.

JPRS-CST-86-044

17 OCTOBER 1986

CHINA REPORT SCIENCE AND TECHNOLOGY

CONTENTS

PEOPLE'S REPUBLIC OF CHINA

NATIONAL DEVELOPMENTS

- Computer Retrieval System Proposed for Standards Database
(Yu Shunzhong; ZHONGGUO BIAOZHUNHUA, No 3, Mar 86) 1

PHYSICAL SCIENCES

- Microcomputer Method for Simulating Transient Response of
Linear Differential Systems
(Huang Guangping, et al.; CHONGQING DAXUE XUEBAO,
No 3, Sep 86) 5
- Adhesive for Uranium in Natural Seawater
(Li Xuanru, et al.; HAIYANG XUEBAO, No 3, 15 May 86) 14
- Specular Direction of Sound Reflection on Rough Surface
(Qi Yirang, et al.; HAIYANG YU HUZAO, No 2, Mar 86) 19
- Characteristics of 1.3 Micron InGaAsP/InP DC-PBH Laser
(Zhao Songshan, et al.; BANDAOTI XUEBAO, No 3, May 86) .. 27
- Characteristics of 1.3 Micron Transverse InGaAsP/InP BH Laser
(Wang Wei, et al.; BANDAOTI XUEBAO, No 3, May 86) 31
- Hermitian Operator in Tensor Product Space Discussed
(Hu Shuan; ZIRAN ZAZHI, No 5, May 86) 34
- Computer Simulation of LiF-CsCl System by Monte Carlo Method
(Chen Nianyi, et al.; ZIRAN ZAZHI, No 5, May 86) 36

APPLIED SCIENCES

- Injury Threshold of Skin Irradiated With 308-NM Excimer
Laser Light
(Li Zhaozhang, et al.; ZHONGGUO JIGUANG, No 12, Dec 85) . 38

Picosecond, Femtosecond Spectroscopy in Semiconductors (Xu Zhongying; HONGWAI YANJIU, No 6, Dec 85)	44
Ultrafast Image-Converter Cameras: Powerful Tools for Transient Recording of Optical Phenomena (Zhou Xuan; WULI, No 3, Mar 86)	60
Beijing Electron-Positron Collider Project Detailed (Gu Mainan; LIAOWANG OVERSEAS EDITION, No 14, 7 Apr 86) .	70
The Time Projection Chamber: New Concept in Particle Detection (Chen Chaoqing; HE JISHU, No 5, May 86)	75
Safety Concept, Safety Design of Ship Nuclear Propulsion System (Yen Jun; HE DONGLI GONGCHENG, No 3, Jun 86)	84

ABSTRACTS

APPLIED SCIENCES

WULI XUEBAO / <u>ACTA PHYSICA SINICA</u> /, No 7, Jul 86	94
--	----

MEDICAL SCIENCE

ZHONGHUA WULI YIXUE ZAZHI / <u>CHINESE JOURNAL OF PHYSICAL MEDICINE</u> /, No 2, 25 Jun 86.....	98
---	----

NUCLEAR MEDICINE

ZIRAN ZAZHI / <u>NATURE JOURNAL</u> /, No 4, Apr 86	100
---	-----

OPTICS

GUANGXUE XUEBAO / <u>ACTA OPTICA SINICA</u> /, No 8, Aug 86	101
---	-----

PHYSICAL SCIENCES

ZIRAN ZAZHI / <u>NATURE JOURNAL</u> /, No 4, Apr 86	106
---	-----

/7310

NATIONAL DEVELOPMENTS

COMPUTER RETRIEVAL SYSTEM PROPOSED FOR STANDARDS DATABASE

Beijing ZHONGGUO BIAOZHUNHUA [CHINA STANDARDIZATION] in Chinese No 3, Mar 86
pp 19-20

[Article by Yu Shunzhong [0151 7311 0022], Qinghai Provincial Bureau of Standards: "Regarding Certain Problems in Overall Design of Computer Retrieval Systems for Standards"]

[Text] There have been precedents both within this country and outside it for using computers to retrieve standards. Initial explorations have also brought us certain results. To keep those in this profession from making the same mistakes and from duplicating our efforts, we are sharing what little experience we have accumulated and our views on the subject, all for the reference of others and to hear the opinions of others.

1. The problem of classifying standards documents

From one point of view, standards documents can be classified into two categories: one being the standards documents themselves (hereafter, just "standards") and the other reference books and periodicals for formulating and revising standards, as well as writing materials (hereafter, just "standards materials").

Because in comparison standards and standards materials are characterized by few categories and clear subclassifications, they should be handled specially in classifying and retrieving. We feel that standards should be stored according to issuing sequence number and that retrieval by category number is most appropriate; for standards materials it is the same as with ordinary books, where it is most appropriate to store and retrieve by the book classification number. This is to say that computer retrieval of standards is retrieval on a small scale in which it is best not to include the retrieval of standards materials, especially when using microcomputers.

2. The problem of writing records and their formats

Since a database is built in a computer for retrieval, it may be said that more should be available from what is retrieved than when retrieval is manual, and we have listed 22 items for the record table and used the contents of these record tables for retrieval. There should be no problems on non-

microcomputers, and on micros this can be managed even if using only floppy disks. However, because disks must be exchanged we may not retrieve according to free association of logical expressions. Therefore, I feel that it would be better when using microcomputers if databases are not built directly according to the standard issuing sequence number in accordance with the record table, but rather each item is only noted by the most essential subordinate material. We have experimented with this system, where for each item is only noted the most essential information, such as standard sequential number, the standard name, book format and page number, the location of the documents, and the date of implementation, as well as special category numbers. For example, GB2867.7-81 cold stamp thrusting movable punch shank [lengchongmo mobing tuirushi huodong mobing] A4-6 (HAN) 81-01 DAJGFBHE, where the fewest number of items satisfy the search for the most essential information desired for a standard.

In summary, whether or not the record table is to be used is a problem worthy of diligent deliberation, especially when using microcomputers.

3. The problem of formats for standard classification and retrieval

As we have stated above, the classification framework for standards should only be undertaken according to the issuing unit and the issuing sequence number. Because these two items both appear in the most conspicuous positions on the covers of standards documents, they are most easily recognized. Also, within a particular location the classification framework can only be undertaken according to a single sequence, for otherwise the arrangement of standards will be disorderly and unsystematic. Many different ways of retrieval may be used, as for example in the "microcomputer standards retrieval system" that we developed, where seven retrieval methods are used: standard sequence number, special classification number, UDC number, freely associated logical expressions, key words in items, first words, and identifiers. Actually, the number of retrieval methods is determined by the entry contents within a record, where the actual sequential format of the standard is not important. Even though, as we said above, we do not use record tables, the three retrieval methods by the standard sequential number, special classification number, and freely associated logical expressions may also be used. As to a detailed explanation of retrieval methods, one may refer to other specialty papers, because here we wish only to explain that the standards classification method and retrieval methods are mutually related and should be separately studied and used.

4. The problem of subclassifying standards

As for other methods of retrieval, the problem of subclassifying standards would not appear to be too important, but when searching according to special classification numbers there is simply no way to proceed unless the standards are subclassified. Because the person who is doing the search can only search according to special classification numbers, that cannot be as quick as searching directly by the standard sequence number. The most important characteristic when searching for special classification numbers (and the greatest advantage) is that the search can be made by hierarchical reduction

of scope. On the computer, the screen hierarchical prompting mode may be used, only by which may the goals of speed, accuracy, and completeness be met.

What is the most suitable way to subclassify? After subclassification, how should numbering be done? These are all problems that should be explored specially. Here, I will only mention the essentials of my own view: there should be large scale distinctions made between the international and national, and between the national and the various ministry commissions, provinces, municipalities, and prefectures, according to issuing units. Also, progressively finer distinctions should be made according to specialized classifications so that a standard article at the lowest level could be fully displayed on only one or two screens. Among classification numbering methods there are currently the alphabetic numbering system, the digital numbering system, and the alphanumeric numbering system, and the "international decimal classification system" in broad use is a digital plus carry classification numbering system. Seeing that there are advantages and disadvantages to the various methods currently in use in systems for the computer retrieval of standards, where it would be difficult to achieve the most satisfactory results from the use of just one, I advocate the adoption of a new alphabetic with carry classification numbering method, which is a "classification numbering method having 26 carry positions" composed of the 26 letters of the English alphabet that I have attached for the reader's perusal. By using this classification method various results such as a clear hierarchical concept, sufficient capacity at each level, and easily recognized symbols can be simultaneously attained.

5. The problem of what type of computer to use

Computer usage is primarily determined by time (speed) and space (internal and external storage), as well as by cost. Regarding time and space, non-microcomputers will naturally be more advantageous than microcomputers, but regarding price, the microcomputer will be much less expensive. As for the retrieval of books or of general scientific and technical materials, due to great demands on capacity, non-microcomputers should generally be chosen. As for the locations of standards materials of a national nature, and since the total number of world standards exceeds 1.2 documents, if they are to be stored as completely as possible, then the large scale mainframes must be used. But for a small to medium size standards information office at the province or city level, where databases are built in accordance with the format of our record tables, and where a location stores from 5 to 10 standards documents, then use of a microcomputer is entirely possible. If an IBM-PC/XT Apple [unclear how this is intended] is chosen, with 512K RAM and fitted with a 10 (or 20) megabyte hard disk, the total price will be about 10,000 yuan; in the case of the domestically produced Great Wall 0520C compatible, where the machine already has a 20 megabyte hard disk, another 20 megabyte hard disk can be added for a total current price of about 40,000 yuan. If our record table is not used and the standard's sequential numbering is used directly, some information will have to be added to the database, but the number of standards that can be stored will be greater by perhaps 10 times. And at the same time, when space allows, use of a microcomputer will have a series of advantages such as less investment, quick start up, low requirements for the operating environment, easy security, and ease in

learning. Therefore, we believe that one should proceed from the actual conditions of the total number of standards needed to be stored at a particular location. Where a microcomputer can be used, it should be. We need not think it necessary to have the biggest and most perfect.

6. Regarding the necessity of setting up auxiliary functions other than inquiry

In a standards retrieval system, there should be other auxiliary functions than just the two important ones of establishing databases and retrieval, functions such as revising, security, and printing.

Regarding the revising function, whether the error is discovered when setting up the database or during its use, it must be correctable. At this time there must first be deletion, then addition; there must also be random entry after the issuance of new standards, and this naturally requires extra space that can be used. If these functions do not exist there will be all sorts of disorder in altering and there will be many errors.

As for the security function, this is done by setting up encrypted passwords, where the encryption can be randomly altered as needed to prevent unauthorized personnel from operating the system. Otherwise, it is possible that when not careful relevant data in the database could be erased, or there could be a malfunction in the computer that would render the system unusable.

As for printing, that is for printing out the information that has been retrieved, because the ability to print is not only convenient for recording that which has been retrieved, but various management functions like library contents, lists by special topics, contents by date, and cards for manual retrieval can be printed out according to the results of freely associated local expressions.

In summary, the auxiliary functions of editing, security, and printing should also be available in a standards retrieval system, for without these functions the system will hardly be usable in a normal way.

12586
CSO: 4008/1074

MICROCOMPUTER METHOD FOR SIMULATING TRANSIENT RESPONSE OF LINEAR
DIFFERENTIAL SYSTEMS

Chongqing CHONGQING DAXUE XUEBAO [JOURNAL OF CHONGQING UNIVERSITY] in Chinese
Vol 8 No 3, Sep 85 pp 55-61

[Article by Huang Guangping [7806 0342 1627], Zheng Tikuan [6774 7555 1401],
and Wang Airen [3769 5676 0086], Department of Thermodynamic Engineering]

[Text] The augmented matrix method is an effective technique for solving high-order differential systems with stiffness, but the existing literature on the subject describes only the single-input form. The present paper describes a multiple-input form. The calculation method used combines time-step progression and iteration, achieving greater accuracy and greatly decreasing the amount of computation needed, so that it is highly suitable for numerical simulations on microcomputers.

I. Introduction

System simulation generally requires the solution of sets of differential and algebraic equations of the form

$$\begin{aligned}\dot{X} &= AX + BU \\ Y &= CX + DU\end{aligned}$$

where A, B, C and D are constant coefficient matrices. When the dimensionalities of the equations are rather large (e.g. 10 dimensions or more) and the stiffness is rather great (a factor of several hundred or more), such problems are rather difficult to solve.

Analog computers are effective in solving such systems of equations, but because systems of high dimensionality require large numbers of amplifiers, large analog devices become necessary. In addition, the accuracy of analog machines is low and it is generally hard to assure high accuracy. As digital

computers have developed and numerous high-level languages have appeared and come into widespread use, digital simulation has increasingly replaced analog simulation. For ease in making the transition from analog to digital simulation, numerous digital computer simulation languages have been developed, such as DAS, MIDAS, MIMIC, DSL, PACTOLUS, CSMP and CSSL [1-4]. These languages can be utilized directly by the user without spending large amounts of time on programming, and they are convenient to use. But the simulations can be run only on large computers and minicomputers, while microcomputers have been useless for the purpose.

The most widely used technique is direct numerical integration, e.g. the Runge-Kutta, Merson and Ji'er [phonetic] methods [5, 7]. But most integration methods are limited by the order of magnitude of the smallest time constant in the equations. A stable system whose stiffness is not very great is readily solved by the above method. But if the system has high stiffness and high dimensionality or if it is unstable, the usual integration methods such as the Runge-Kutta method may fail or have a high degree of error, and in addition will be very slow. Such problems are even more difficult to solve on microcomputers because of the short word length. Consequently microcomputer simulation requires increased simulation accuracy and decreased amounts of computation in order to increase simulation speed.

Taylor's augmented matrix method [8] is an effective method of solving stiff linear differential systems on microcomputers under certain specific input conditions. But his technique is only a single-input form, and it too requires large amounts of computation and a rather large amount of internal memory in the case of high-dimensionality systems. Below we expand the augmentation method to multiple inputs, subject to the requirement that every component of the input vector is the usual type of step, slope, acceleration or exponent input. In addition, some augmentations are possible when the multiple inputs are not simultaneously perturbed. In the case of high-dimensionality, large time scale problems, in order to increase numerical efficiency, the time-step progression method can be used at the beginning of computation, with later replacement by the iteration method, and if the optimum iteration time is determined the amount of computation needed can be minimized.

II. The Augmentation Method for Multiple-Input Equations

Suppose that the system to be simulated is

$$\begin{cases} \dot{X}(t) = AX(t) + BU(t) \\ Y(t) = CX(t) + DU(t) \\ X(0) = X_0 \end{cases} \quad (1)$$

where X is n -dimensional, Y is m -dimensional, and U is r -dimensional. In other words, the system is a multiple-input, multiple-output system.

We know from control theory [9] that the solution of a differential equation consists of two parts: the free terms and the forced terms. In numerical integration of the forced terms, assuring accuracy requires a rather large amount of computation (see Ref. 10). If homogeneous equations are involved, then the solution has only free terms and accuracy can be satisfactorily guaranteed by choosing a suitable number of terms in the expansion of e^{At} . The principle of the augmented matrix method is that the forced input terms are converted to a state vector and nonhomogeneous equations are converted to homogeneous equations. As in the single-input augmentation matrix of Ref. 8, when every component of U is a step, slope, acceleration or exponent, the augmentation is easily realized.

Taking as an example the case in which the input vectors are all constants, we write

$$U(t) = K \quad (t \geq 0)$$

where

$$K = [K_1, K_2, \dots, K_r]^T$$

We define the $n+1$ -th, $n+2$ -th, ..., $n+r$ -th state vectors as

$$x_{n+1}(t) = u_1(t) = K_1, x_{n+2}(t) = u_2(t) = K_2, \dots, x_{n+r}(t) = u_r(t) = K_r$$

Then,

$$\begin{aligned} \dot{x}_{n+1}(t) &= 0, & x_{n+1}(0) &= 0 \\ \dot{x}_{n+2}(t) &= 0, & x_{n+2}(0) &= K_2 \\ \dots & \dots & \dots & \dots \\ \dot{x}_{n+r}(t) &= 0, & x_{n+r}(0) &= K_r \end{aligned}$$

Then, following augmentation, the state equation, output equation and initial conditions are

$$\begin{pmatrix} \dot{x}(t) \\ \dot{x}_{n+1}(t) \\ \dot{x}_{n+2}(t) \\ \vdots \\ \dot{x}_{n+r}(t) \end{pmatrix} = \begin{pmatrix} A & B \\ 0 & 0 \end{pmatrix} \begin{pmatrix} x(t) \\ x_{n+1}(t) \\ x_{n+2}(t) \\ \vdots \\ x_{n+r}(t) \end{pmatrix} \quad (2)$$

$$Y(t) = [C|D] \begin{pmatrix} X(t) \\ x_{n+1}(t) \\ x_{n+2}(t) \\ \vdots \\ x_{n+r}(t) \end{pmatrix} \quad (3)$$

$$\begin{pmatrix} X(0) \\ x_{n+1}(0) \\ x_{n+2}(0) \\ \vdots \\ x_{n+r}(0) \end{pmatrix} = \begin{pmatrix} X_0 \\ K_1 \\ K_2 \\ \vdots \\ K_r \end{pmatrix} \quad (4)$$

Let $X_{nr} = [x_{n+1}, x_{n+2}, \dots, x_{n+r}]^T$. Then the above equations can be simplified to

$$\begin{cases} \dot{\bar{X}}(t) = \bar{A} \bar{X}(t) \\ Y(t) = \bar{C} \bar{X}(t) \\ \bar{X}(0) = \bar{X}_0 \end{cases} \quad (5)$$

where

$$\bar{A} = \left(\begin{array}{c|c} A & B \\ \hline O & O \end{array} \right) \text{ is the augmented transfer matrix,}$$

$$\bar{C} [C|D] \text{ is the augmented observation matrix}$$

$$\bar{X} = \left(\begin{array}{c} X \\ \hline X_{nr} \end{array} \right) \text{ is the augmented state vector.}$$

Many of the systems that are simulated are multiple-input, multiple-output models. Some of them have numerous influencing factors, so that the input may

have tens or hundreds of dimensions. If we use the augmentation techniques described above, then the order of the matrix will be much greater after augmentation, which creates difficulty in calculating the matrix coefficients and takes up large amounts of internal memory. Actually, when a model is being investigated or a certain term is being simulated, far from all of the input quantities will be used; in addition, some input vectors will be zero. In order to decrease unnecessary calculations and increase numerical efficiency, we can confine ourselves to the relevant inputs in the augmentation process. If the input vector is

$$U(t) = \begin{pmatrix} U_A(t) \\ \hline U_B(t) \end{pmatrix}$$

where $U_A = [K_1, K_2, \dots, K_{r_1}]^T$ is an r_1 -dimensional constant vector

and $U_B = 0 = [0, 0, \dots, 0]^T$ is an $r - r_1 = r_2$ -dimensional zero vector,

and if for the corresponding B-matrix,

$$B = [B_1 \mid B_2]$$

where B_1 is an $n \times r_1$ matrix formed by the column vectors representing the nonzero inputs of U and B_2 is the $n \times r_2$ matrix formed by the remaining columns of U after elimination of B_1 , then the equation has the form

$$\dot{X} = AX + [B_1 \mid B_2] \begin{pmatrix} U_A \\ \hline 0 \end{pmatrix}$$

or

$$\dot{X} = AX + B_1 U_A \quad (6)$$

We now again perform augmentation by the above method; here, \bar{A} will be an augmented transfer matrix of dimensionality $(n + r_1) \times (n + r_1)$, the number of elements in which is smaller than that in the augmented full-input matrix by $(n + r)^2 - (n + r_1)^2 = 2(n + r_1)r_2 + r^2$, which greatly decreases the number of unnecessary calculations.

III. Combination of the Time-Step Progression and Iteration Methods

If the coefficients of the augmented transfer matrix are $\exp(\bar{A}h)$, where

$$\exp(\bar{A}h) = I + \bar{A}h + \frac{\bar{A}^2 h^2}{2!} + \dots + \frac{\bar{A}^N h^N}{N!} + \dots,$$

with h representing the time step (which is generally chosen rather small in order to assure convergence of the coefficients), then the augmented homogeneous equations can be solved by iteration, obtaining

$$\begin{aligned}\bar{X}(h) &= \exp(\bar{A}h) \bar{X}(0) \\ \bar{X}(2h) &= \exp(\bar{A}h) \bar{X}(h) \\ \dots &\dots \\ \bar{X}(nh) &= \exp(\bar{A}h) \bar{X}((n-1)h) \\ \dots &\dots\end{aligned}$$

and by using the "hopping" [kuitiao 6423 6426] technique we can obtain the time step progression solution

$$\begin{aligned}\bar{X}(h) &= \exp(\bar{A}h) \bar{X}(0) \\ \bar{X}(2h) &= \exp(\bar{A}h) \cdot \exp(\bar{A}h) \cdot \bar{X}(0) \\ &= \exp(2\bar{A}h) \bar{X}(0) \\ \bar{X}(4h) &= \exp(2\bar{A}h) \cdot \exp(2\bar{A}h) \cdot \bar{X}(0) \\ \dots &\dots \\ \bar{X}(2nh) &= \exp(n\bar{A}h) \cdot \exp(n\bar{A}h) \cdot \bar{X}(0) \\ \dots &\dots\end{aligned}$$

The first of these systems is the solution of the iteration problem, while the second gives the increase in the time step in the matrix coefficients obtained as a result of squaring. In the former solution the iteration errors will accumulate; and although the latter has no iteration errors, as the time lengthens, the steps will gradually increase, and eventually the steps will be too large and the resulting plots will be inaccurate. In terms of the amount of computation required, although the time-step progression method involves a small number of computation steps, each step entails multiplication of one matrix by another followed by multiplication by a vector, so that in the case of a high-order matrix the total number of calculations will be rather large. Although in the iteration process each step involves simply the multiplication of a matrix by a vector, for a large-time-scale problem the amount of computation required for the multiple iterations will also be rather large. An effective way of overcoming these deficiencies is to combine the two techniques, using the time-step progression method at the outset for small time scales, then changing to the iteration method after the time step reaches a certain length. If the initial step is h , the iteration interval is T , and the solution time scale is $[0, T_1]$, then the time progression is

$$h, 2h, 4h, 8h, \dots, \frac{1}{4}T, \frac{1}{2}T, T, 2T, 3T, \dots, T_1 - T, T_1$$

where $T = 2^K h$; K is the number of cumulations in the first stage. In order to minimize the amount of calculation, an optimum iteration time T can be chosen. Let there be a set of homogeneous equations (obtained by iteration as described above if the problem initially involved non-homogeneous equations):

$$\begin{aligned}\dot{X} &= AX \\ Y &= CX\end{aligned}$$

where X and Y are an n -dimensional and an m -dimensional vector respectively.

The number of steps in the time-step progression is $K = \log_2(T/h)$. The step size in the iteration calculation is $T_1/T - 1$. The number of multiplications performed in the time-step progression calculation is

$$P_1 = (n^3 + n^2 + n \times m) \cdot \log_2 \left(\frac{T}{h} \right)$$

The number of multiplications needed in the iteration calculation is

$$P_2 = (n^2 + n \times m) \left(\frac{T_1}{T} - 1 \right)$$

The total number of multiplications performed in the entire calculation (excluding the determination of $\exp(Ah)$) is

$$P = P_1 + P_2 = (n^3 + n^2 + n \times m) \cdot \log_2 \left(\frac{T}{h} \right) + (n^2 + n \times m) \cdot \left(\frac{T_1}{T} - 1 \right)$$

We find the poles of the above equation; then P is at a minimum when

$$T = \frac{(n + m) \ln 2}{n^2 + n + m} \cdot T_1$$

Because T must meet the condition $T = 2^K h$, if we first specify h , then the time obtained from equation (7) may fall between two values of T . Either the number of entries for the larger of the T 's can be decreased, making the grid somewhat sparser, or the grid for the slightly smaller T can be made more dense, but in the initial stage both cases are the same; the only difference is that one involves more steps than the other. As regards asymptotic stability, the former approach is more suitable; but if the duration of the process is too long and if peaks, oscillations and the like may occur in the latter part of the curve, the smaller value of T should be chosen. Conversely, if the optimum value of T is chosen from the formula and is used in turn to choose h , the best method is to work backward in a geometric progression, obtaining a value of h that is related to the convergence of $\exp(Ah)$.

Ref. 11 is an example of a solution using the method described here. It involves a model of a 200,000 kW fossil-fired power generating unit operating in the vicinity of the rated characteristics, with a 36-dimensional state vector, a 9-dimensional input vector, a non-state vector requiring 7 observables, and a dynamic process duration of 3000 seconds. When the input vector is all step values, the augmented matrix method is used to convert the non-homogeneous equations of the numerical model into homogeneous equations. Thus $n = 36 + 9 = 45$, $m = 7$, and $T_1 = 3000$ seconds. We find from equation (7) the optimum iteration step $T = 52.06$ seconds. In order to make the observations occur at suitable times, we choose $T = 50$ seconds. From the characteristics of the augmented transfer matrix, in order to make $\exp(Ah)$ converge rapidly, $h = 0.1$ seconds. For $T = 50$ seconds, we work backward in a geometric progression, choosing the suitable value $h = 0.09766$ seconds. Thus, we expand from 0.09766 seconds to 50 seconds in a 9-step progression and then proceed to 3000 seconds in 59 iterations with a 50-second time step. In an iteration process with a time step of 0.0766 seconds, a total of 30,719 iterations would be required to reach T_1 . If the number of observations is the same in both methods, then for the differential equations needed to solve this problem the number of multiplications required (not including determination of $\exp(Ah)$) would be $9.5985 \cdot 10^5$ for the mixed method and $6.2206 \cdot 10^7$ for the iteration method.

The latter method requires 65 times as many computations. Another extremely important point is that because the mixed method requires only 59 iterations, while the iteration method requires 30,791 iterations, the roundoff error of the iteration method will be greater than that of the mixed method.

IV. Conclusions

The use of the augmented matrix method to solve systems of linear constant differential equations is free of limitations on equation dimensionality and number of inputs and can be used to solve stable or unstable, stiff or nonstiff systems. In particular, its advantages over ordinary numerical methods show up most clearly when solving stiff systems. When the combination of the time-step progression and iteration methods described

above is used, the computation is rapid and accurate, internal memory requirements are low, the method is easy to program, so that it is particularly well suited for rapid numerical computations on microcomputers.

BIBLIOGRAPHY

1. Hartnett, R. T., F. J. Sanson, and L. M. Warshowsky. "MIDAS, an Analog Approach to Digital Computation," SIMULATION, Vol 3, No 5, May 1964.
2. Brennan, R. D. "PACTOLUS, a Simulator Language Which Makes a Digital Computer Feel Like an Analog Computer," SIMULATION, Vol 6, No 2, August 1964.
3. Sci Software Committee. "The Sci Continuous System Simulation Language, SIMULATION, December, 1967.
4. Xiong Guangleng [3574 0342 2807]. "Kongzhi xitong shuzi fangzhen" [Numerical Simulation of Control Systems], Qinghua University Press, 1982.
5. Chacz, A. S., and G. H. Burgin. "Comment on the Runge-Kutta-Merson Algorithm," SIMULATION, August, 1976.
6. Gear, C. W. "Simultaneous Numerical Solution of Differential-Algebraic Equations," TRANS. IEEE/PGCT, Vol CT-18, No 1, January 1971.
7. Feng Kang [7458 1660], et al. "Shuzhi jisuan fangfa" [Numerical Computation Methods], National Defense Industry Publishers, 1978.
8. Taylor, Fred. J. "Transient Response Analysis of Linear Differential Systems on Minicomputers," SIMULATION, January 1977.
9. Li Youshan [2621 0645 0810]. "Zidong kongzhi yuanli" [Fundamentals of Automatic Control], National Defense Industry Publishers, August 1981.
10. Hitz, K. L., and T. E. Fortmann. "An Introduction to Linear Control Systems," Marcel Dekker, Inc., 1977.
11. Huang Guangping [7806 0342 1627]. "Numerical Simulation of the Dynamic Characteristics of a 200-MW Boiler and Turbine Unit," CHONGQING DAXUE XUEBAO [Journal of Chongqing University], No 1, 1985.

8480

CSO: 4008/1017

PHYSICAL SCIENCES

ADHESIVE FOR URANIUM IN NATURAL SEAWATER

Beijing HAIYANG XUEBAO [ACTA OCEANOLOGICA SINICA] in Chinese Vol 7 No 3
15 May 85 pp 313-316

[Article by Li Xuanru [2621 6513 1171], Chen Lianzhi [7115 6647 1807], Liu Shiyu [0491 4258 3768], and Hong Yuying [3163 3768 5391]: "Use of Alkaline Zinc Carbonate Adsorbent for Adsorption of Uranium in Natural Seawater"; paper received 15 November 1983]

[Text] The experimental results in this paper show:

1. The following relationship exists between the concentration of uranium in the adsorbent and the uranium contained in the natural seawater used:
 $C = 8.51 \times 10^{-1}(u^*)^{0.49}$.

2. When the amount of adsorbent basically does not change, as the amount of seawater passed through the adsorbent column increases, the amount of uranium adsorbed by the adsorbent, the uranium concentration in the adsorbent and the concentration of uranium which remains in the natural seawater after uranium adsorption constantly increases; the recovery rate of uranium constantly decreases; after the distribution coefficient decreases to a certain value as the volume of seawater passed through the adsorbent column increases it rises again slightly.

There are currently very few papers abroad dealing with the adsorption of uranium in seawater using alkaline zinc carbonate. This paper used an experiment passing water through a cylindrical tube to bring the adsorbent directly into contact with a large quantity of natural seawater and at set intervals sampled, analyzed and measured the amount of uranium adsorbed by the adsorbent, and from the results of the experiment explain the laws of adsorption of uranium in natural seawater using alkaline zinc carbonate.

Let u be the amount of uranium adsorbed by the adsorbent (in grams); u^* is the amount of uranium contained in the natural seawater used (in grams); G is the weight of the natural seawater used (in grams); T is the amount of adsorbent used (in grams); C_0 is the concentration of uranium in the natural seawater (gram/gram); the average concentration of uranium in seawater from the Xiamen harbor is 2.8×10^{-9} grams of uranium/grams (of seawater); C is the concentration of uranium in the adsorbent (gram/gram); C_{\max} is the

amount of saturated uranium adsorbed by the adsorbent (gram/gram); Q is the amount of seawater used/the amount of adsorbent used (gram/gram); R is the uranium recovery rate; k_d is the distribution coefficient; k and n are constants.

On the basis of the above assumptions, we can obtain the following series of equations:

$$u = CT ; \quad (1)$$

$$u^* = C_o G ; \quad (2)$$

$$Q = G/T ; \quad (3)$$

$$C_o^* = \frac{u^* - u}{G} = \frac{C_o G - CT}{G} = C_o - C/Q = C_o(1 - R) ; \quad (4)$$

$$C = k_d C_o^* = k_d (C_o - C/Q) ; \quad (5)$$

$$R = \frac{u}{u^*} = \frac{CT}{C_o G} = \frac{C}{C_o Q} ; \quad (6)$$

$$k_d = \frac{C}{C_o^*} = \frac{R}{1 - R} Q = \frac{1}{C_o/C - T/G} ; \quad (7)$$

$$C_{max} = \lim_{Q \rightarrow \infty} C = \lim_{Q \rightarrow \infty} k_d (C_o - C/Q) = k_d C_o. \quad (8)$$

I. Experiment Part

(1) Adsorbent manufacturing conditions

A specific quantity of 0.6M $ZnSO_4$ solution was added to a small quantity of such organic additives as 5-nitro-2-amino phenol, and while boiling and constantly stirring it, a 1.0M Na_2CO_3 concentration of the same mass as the $ZnSO_4$ concentrations was added, and the boiling continued for 20 minutes, then it was cooled and aged for 22 hours. The adsorbent was thoroughly washed until there were no sulphuric acid roots, then filtered, dried, and ground through a screen to 40-80 μ [4158] adsorbent.

(2) A water pump was used to draw natural seawater into a holding pool, and after clarification, it was drawn into a sand filtration pool and filtered, then the filtered seawater was drawn into plastic foam filter and further refined. The refined seawater was passed through the adsorption column with its flow velocity controlled to a set speed by a rotameter, brought in direct contact with a set amount of adsorbent, and after exchange adsorption, the seawater was expelled from the upper end of the adsorption column.

The amount of adsorbent used in this experiment was 419 grams, the seawater flow velocity was 8.0 kg/min. After analysis and measurement, it was determined that the average amount of uranium contained in Xiamen harbor seawater was 2.8 μ g uranium/kg (seawater), then each day about 32.26 mg of uranium was passed through the adsorption column, and each day samples were taken

and the amount of uranium adsorbed by the adsorbent was analyzed and measured. The results are given in Table 1.

Table 1. Relationship of the Number of Days Water Was Passed Through the Adsorbent (419 g) and the Amount of Uranium It Adsorbed

Number of days water passed (days)	Amount of uranium adsorbed (μg uranium/grams)
4	272
5	302
6	336
7	340
8	354
9	382
12	429
13	437
14	469
15	514
16	518

From the experimental results it can be proved that the alkaline zinc carbonate adsorption of uranium in natural seawater is little influenced by the seawater temperature. Thus, on the basis of the results of this experiment, the relationship between the amount of uranium adsorbed by the adsorbent and the amount of uranium in the seawater which was passed through the adsorption column are in Figure 1.

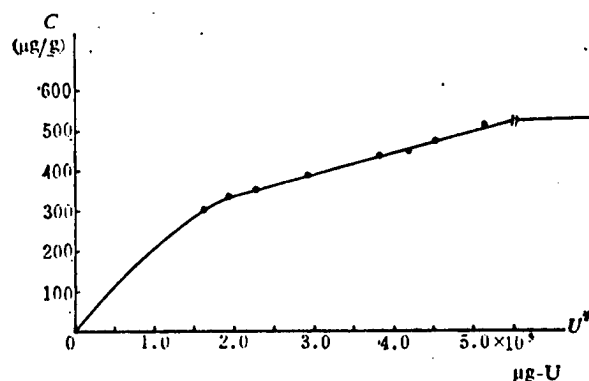


Figure 1. Relationship of C and u^*

From this it is clear that the alkaline zinc carbonate adsorption of uranium in natural seawater basically conforms to the temperature equation of Freundlich et al., and its adsorption equation can be expressed as follows:

$$C = k(u^*)^n,$$

in which the two constants k and n can be solved on the basis of the data in Table 2 serving as the diagram of the relationship of $\log C$ and $\log u^*$ (Figure 2).

Table 2. Relationship of Number of Days Water Passed Over Adsorbent and G , u , u^* , Q , C , C_0^* , R , and k_d

(1) 通水天数 (天)	G (10^6 克) (2)	T (克) (2)	u (10^{-6} 克) (2)	u^* (10^{-6} 克) (2)	Q (10^3 克/克) (3)	C (10^{-6} 克/克) (3)	C_0^* (10^{-6} 克/克) (3)	R ($\times 10^{-2}$)	k_d ($\times 10^3$)
5	57.60	419	126538	161280	137.47	302	0.603	78.46	500.70
6	69.12	419	140780	193536	165.00	336	0.763	72.75	440.50
7	80.64	419	142460	225792	182.46	340	1.033	63.09	329.02
9	103.68	419	160058	290304	247.45	382	1.256	55.13	304.08
12	138.24	419	179751	387072	329.93	429	1.500	46.44	286.10
13	146.76	419	183103	419328	357.42	437	1.577	43.67	277.05
14	161.28	419	196511	451584	384.92	469	1.582	43.51	269.54
16	184.32	419	217042	516096	439.90	518	1.622	42.05	319.26

Note: T is actually not constant because when the amount of uranium contained in the adsorbent was analyzed, each time we needed to take a sample of about 1 gram for analysis, but its impact on the calculations in the table is not substantial.

Key:

1. Number days water passed over adsorbent
2. Grams
3. Grams/grams

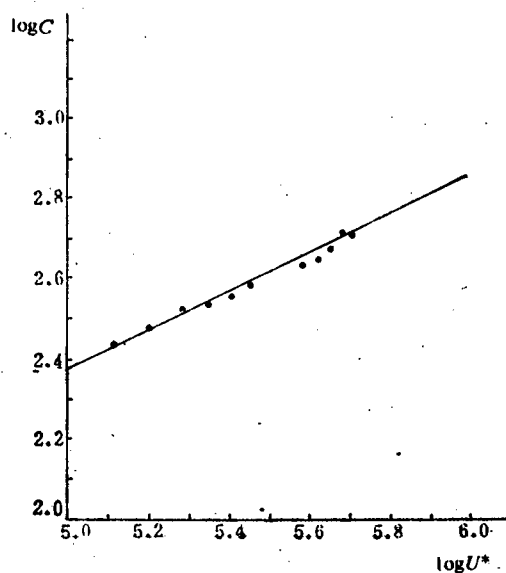


Figure 2. Relationship Diagram of $\log C - \log u^*$

Linear slope:

$$n = \frac{2.8600 - 2.3700}{6.0000 - 5.0000} = 0.49,$$

intercept: $\log k = -0.07$, $k = 8.51 \times 10^{-1}$.

Therefore, the equation is: $C = 8.51 \times 10^{-1}(u^*)^{0.49}$.

Carrying out test calculations on C on the basis of the experimental data, the results are as follows:

C (original)	272	302	336	340	514	518
C (calculated)	272	303	331	357	517	536

C (original) is experimental test data; C (calculated) is data calculated on the basis of the above equations.

II. Results and Discussion

1. When the amount of adsorbent (T) used does not change, as the amount of water (G) which is passed through the adsorbent column increases, the amount of uranium (u) which is adsorbed by the adsorbent, the concentration of uranium (C) in the adsorbent and the concentration of uranium (C_0^*) which remains in the seawater after the uranium is adsorbed increases; thus the uranium recovery rate constantly decreases. However, after the distribution coefficient (k_d) increases and decreases to a certain point, it rises again slightly.

2. The adsorption of uranium in natural seawater by the alkaline zinc carbonate adsorbent under the conditions in this paper basically conforms to the Freundlich equation:

$$C = 8.51 \times 10^{-1}(u^*)^{0.49}.$$

REFERENCES

1. Wei Fangsheng [1442 2455 2573], KAISUICHO NO YURAN NO SAISHU (VI), CHITANSAN NI YORU KAISUICHO NO YURAN NO KYUCHAKU, Nihon Genshiryoku Gakkaishi, 13 (1971), 3:121-127.

8226/6091

CSO: 4008/1096

SPECULAR DIRECTION OF SOUND REFLECTION ON ROUGH SURFACE

Beijing HAIYANG YU HUZAO [OCEANOLOGIA ET LIMNOLOGIA SINICA] in Chinese Vol 17, No 2, Mar 86 pp 111-116

[Article by Qi Yirang [2058 6095 6245], Lu Deming [6424 1795 2494], Xu Liezhong [1776 3525 1813], Wei Xiaoyuan [5898 1321 3123], Li Jiangji [2621 3068 0679], and Wang Meifen [3769 2734 5358], Shandong College of Oceanology, Qingdao: "The Sound Reflection in Specular Direction on a Rough Surface"; draft receipt date: 28 April 1984]

[Text] English abstract: The reflected sound in specular direction on a rough surface was investigated in laboratory wind-driven tank. The probability density function (PDF) of the rough surface deviated from the Gaussian function to different extent. The measured results were compared with the results calculated by the aid of the Gaussian function and Gram-Charlier series. There is a linear relationship between $\ln \frac{\bar{p}}{p_0}$ and $2(\gamma\sigma)^2$ in the range of small value of $\gamma\sigma$ ($\gamma\sigma < 1$) where \bar{p} and p_0 are the average amplitude of sound pressure reflected on rough surface and the amplitude of sound pressure reflected on smooth surface, respectively and

$\gamma = \frac{\lambda}{2\pi} \sin\theta$ where θ is the glancing angle and λ is the sound wave length.

The slope of the linear relationship is smaller than that predicted by the Eckart theory. The standard deviation σ_w measured by wave-height meter is close to the value obtained from our experimental relationship but larger than that calculated by the aid of the Gaussian type PDF.

The reflection characteristics of rough water surface on sound waves is determined by the probability distribution of the rise and fall of the surface. Eckart^{1,4} used the probability density function (PDF) of rough surface to calculate the average reflected sound pressure and hypothesized that the PDF was Gaussian. But the Gaussian PDF with regard to wind-driven water surfaces is an approximate description⁶. Clay, Medwin and Wright³ carried out analog sea surface tests in a water tank. They used plastic spread on the water surface to create an air passage about 15.2 cm high and

Note: This work was carried out with the support of Professor Yang Youfan [2799 2589 2868]. While measuring waves, Comrade Gao Shenyue [7559 1957 2588] of this institute's Department of Physical Oceanography provided enthusiastic assistance and we express our deepest gratitude.

produced waves using a fan. Their work showed that the average reflected sound pressure is very sensitive to PDF and the very slight deviation of the form of the PDF with regard to the Gaussian function will clearly influence the reflected sound pressure.

We researched the problem of reflection of wind-driven water surface on sound waves and on the basis of the average reflected sound waves measured during the experiments we predict the standard deviation of the undulation of the water surface.

I. Experiment Method

The experiments were carried out in the wind-driven water tank of our institute's Dynamics Laboratory. The water tank is 120 m long and 2 m wide. By changing the rotation speed of the wind machine different wind velocities can be produced and thus obtaining different water surface situations. To eliminate reflection waves from the two ends of the water tank we placed wave elimination material at the two ends. In the region where the sound measurements were conducted, the two sides and the bottom of the tank were covered with rubber wedge acoustical material. The overall length of the measurement area was 5 m, and a 0.5 m-high damper was used to divide the area laterally into emission and reception areas. The damper was also covered with rubber wedges thus effectively eliminating interference from direct sound waves. During the measurements, the water depth was maintained at about 0.75 m and the top of the damper was about 0.25 m above the water surface. The water surface sound photographing area was in the middle of the square measurement area on the damper. Figure 1 is a photograph of the measurement area.

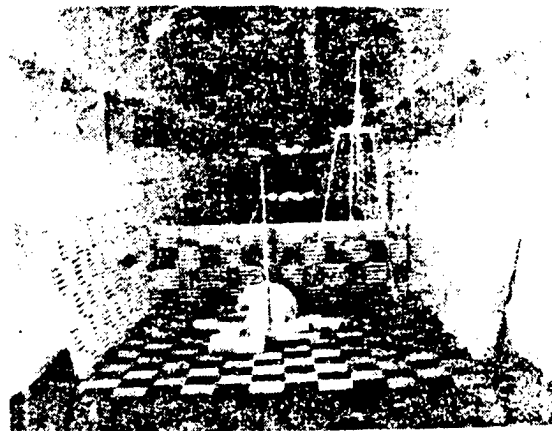


Figure 1. Test Area

The acoustical emitter was made up of an emission transducer and a reflector cover. The transducer component was a ring made of PZT-5 material with an outer diameter of 20 mm and an inner diameter of 10 mm. The ring was placed in a shell of organic glass filled with organic silicone oil. The double-layered right-angle cone type reflector cover was made of 2 mm thick aluminum plate. Between the two layers of aluminum plate was air. The diameter of

the opening was 250 mm, and the transducer was placed on the symmetrical axis of the right-angle cone. The directionally characteristic acuteness of the angle of the acoustical emitter was about 12° . The electrical excitation signal was a single frequency packed pulse signal, with a pulse width of 0.5 ms, a repeated frequency of 20 Hz, and a packed signal frequency change range of 30-170 kHz.

The acoustical receiver was a hollow spherical hydrophone with an outer diameter of 10 mm. During the measurements, the hydrophone's position had to be adjusted so that the smooth surface reflected signals it could receive were maximized. When the glancing angle was 30° and 45° , the distance between the hydrophone and the emitter was 2.4 m and 1.5 m respectively. The received signal was observed directly with an oscilloscope and recorded photographically. Examples of smooth surface and rough surface reflected signal are illustrated in Figure 2.



Figure 2. Photograph of Rough and Smooth Water Surface Sound Reflection Signal
Glancing angle 30° , packed signal frequency 100 kHz. On top is the smooth water surface sound reflection signal; below is the rough water surface sound reflection signal (water surface undulation standard deviation $\sigma = 5$ mm)

Measurement precision using a tantalum capacitor wave-height device to measure water surface undulations was ± 0.3 mm, when the measurement probe was within 20 cm of the sound photographing area. The measurement system was corrected by using the method of gradually submerging the probe by changing the height of the water surface. The acoustical signal and water wave signal were recorded at the same time, taking about 1 minute of recording time for each record. The water wave record curve was sampled at intervals of 0.025 seconds, the wave surface coordinate read and then they were processed using a computer. Figure 3 is a block diagram of the measurement system.

II. Measurement Results and Discussion

1. Wave Measurement

On the basis of the wave surface measurement data we computed the standard deviation σ , bias coefficient C_s and the peak coefficient C_E .²

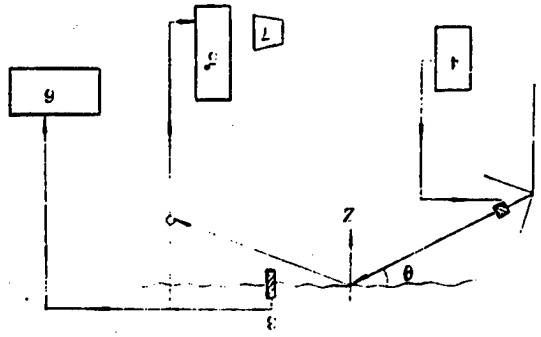


Figure 3. Block Diagram of Sound Signal and Wave Measurement System
1--Sound emitter; 2--Water listening device; 3--Wave height meter probe; 4--Emitter; 5--Oscilloscope; 6--Wave height meter; 7--Photographic system. (The circle in the diagram is 2)

$$\sigma = N^{-\frac{1}{2}} \left[\sum_{i=1}^N (Z_i - \bar{Z})^2 \right]^{\frac{1}{2}} \quad (1)$$

$$C_s = N^{\frac{1}{2}} \frac{\sum_{i=1}^N (Z_i - \bar{Z})^3}{\left[\sum_{i=1}^N (Z_i - \bar{Z})^2 \right]^{3/2}} \quad (2)$$

$$C_E = N \frac{\sum_{i=1}^N (Z_i - \bar{Z})^4}{\left[\sum_{i=1}^N (Z_i - \bar{Z})^2 \right]^2} \quad (3)$$

in which N is the data where $N > 1600$; Z_1 is the wave surface coordinate reading, where Z_1 tends downward it is positive (see Figure 3). \bar{Z} is the average water surface position. Figure 4a is an example of the wave record curve, Figure 4b is the corresponding wave surface coordinate probability distribution, the experiment points are the results of wave height measurement, and the Gaussian probability distribution curve is also drawn. From the figures it can be seen that the actual wave surface coordinate probability distribution is clearly different from the Gaussian curve. The peak of the former is near $Z/\sigma = 0.5$.

2. Acoustical Signal Measurement

We calculated the ratio of rough water surface average reflected sound pressure \bar{p} and the smooth water surface reflected sound amplitude p_0 on the basis of oscilloscope photographs of the rough and smooth water surface reflected signals under the same conditions. The relationship of $\ln(\bar{p}/p_0)$ and $2(\gamma\sigma)^2$ is as illustrated in Figures 5 and 6, in which $\gamma = k \sin \theta$;

$k = \frac{2\pi}{\lambda}$; θ is the glancing angle; λ is the sound wave wavelength and the velocity of sound is 1500 m/s. When measured at different frequencies,

since it is very difficult to make the water surface conditions completely identical, for each frequency we recorded the corresponding wave curve and found the corresponding value of σ . Within the range of $\gamma\sigma < 1$, the experimental results can be expressed approximately as a straight line:

$$\ln(\bar{p}/p_0) = -2A(r\sigma)^2 \quad (4)$$

in which $A = 0.34$.

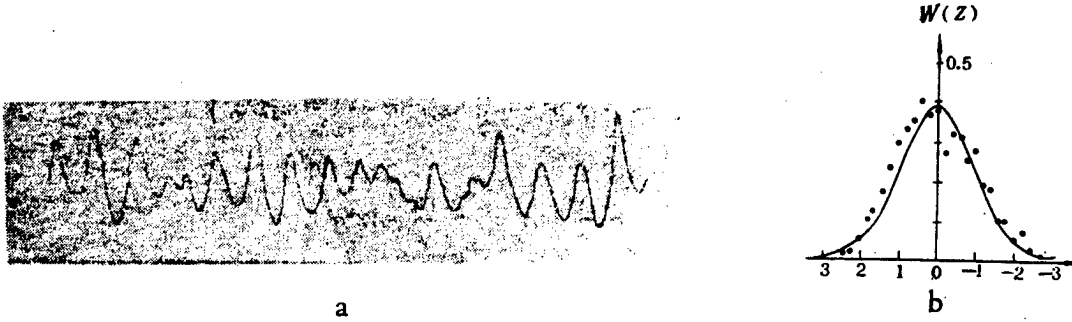


Figure 4. Wave Record Curve Example and Its Corresponding Wave Surface Coordinate Frequency Distribution
a--Wave record curve; b--Wave surface coordinate frequency distribution

... is the wave height meter measurement results, measurement conditions: $\sigma = 0.44$ cm, $C_S = 0.24$, $C_E = 2.6$; — Gaussian frequency distribution curve, for Gaussian distribution: $C_S = 0$, $C_E = 3$

On the basis of Eckart's theory⁴

$$\bar{p} = p_0 \int_{-\infty}^{\infty} \exp(-2irZ) W(Z) dZ \quad (5)$$

in which $W(Z)$ is the probability density function of a random surface;
 $\gamma = k \sin \theta$, $k = \frac{2\pi}{\lambda}$, θ is the glancing angle, and λ is the sound wave wavelength. For Gaussian surfaces

$$W(Z) = \frac{1}{\sqrt{2\pi}\sigma} \exp\left(-\frac{z^2}{2\sigma^2}\right) \quad (6)$$

Substituting Eq. (6) in Eq. (5), we get

$$\ln(\bar{p}/p_0) = -2(r\sigma)^2$$

and in Figures 5 and 6, Eq. (7) is expressed as a dotted line.

Huang and Long point out⁵ that the first four terms of the Gram-Charlier series can be used to express the probability density function of random surfaces:

$$W(Z) = \frac{1}{\sqrt{2\pi}\sigma} e^{-\frac{Z^2}{2\sigma^2}} \left(1 + \frac{1}{3} m_3 H_3 + \frac{1}{12} m_4 H_4 + \frac{1}{18} m_3^2 H_6 \right) \quad (8)$$

in which $m_3 = C_S/2$; $m_4 = (C_E-3)/2$. And H_n is the Hermitian multi-term expression:

$$\begin{aligned} H_3 &= t^3 - 3t; & H_4 &= t^4 - 6t^2 + 3; \\ H_6 &= t^6 - 15t^4 + 45t^2 - 15. \end{aligned}$$

In which $t = Z/\sigma$.

Substituting Eq. (8) in Eq. (4), we get

$$\frac{\bar{p}}{p_0} = e^{-2(\gamma\sigma)^2} \left(1 + \frac{4}{3} m_3 \gamma^4 \sigma^4 - \frac{32}{9} m_3^2 \gamma^6 \sigma^6 - \frac{i8}{3} m_3 \gamma^3 \sigma^3 \right) \quad (9)$$

whose amplitude ratio is

$$\begin{aligned} \frac{|\bar{p}|}{p_0} &= e^{-2\gamma^2 \sigma^2} \left(1 + \frac{8}{3} m_3 \gamma^4 \sigma^4 + \frac{16}{9} m_3^2 \gamma^8 \sigma^8 \right. \\ &\quad \left. - \frac{256}{27} m_3 m_3^2 \gamma^{10} \sigma^{10} + \frac{1024}{81} m_3^4 \gamma^{12} \sigma^{12} \right) \end{aligned} \quad (10)$$

The results of the calculations according to Eq. (10) are plotted in Figures 5 and 6, with C_S and C_E taken from Table 1.

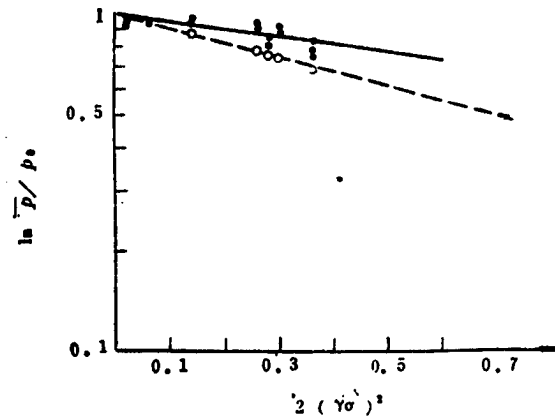


Figure 5. Relationship of $\ln(\bar{p}/p_0)$ and $2(\gamma\sigma)^2$ When Glancing Angle is 30°
 \dots is test result, each test point is the average of 100 pieces of data; $---$ represents Eq. (7); $\circ\circ\circ$ is the results of calculations using Eq. (10); $\gamma = k \sin \theta$ (in which $k = \frac{2\pi}{\lambda}$; θ is the glancing angle; λ is the sound wave long-wave)

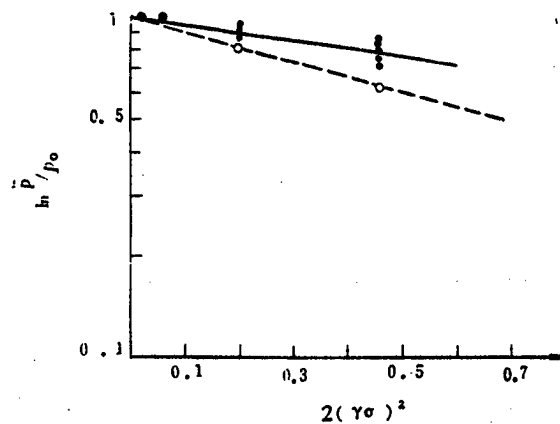


Figure 6. Relationship of $\ln(\bar{p}/p_0)$ and $2(\gamma\sigma)^2$ When Glancing Angle is 45°
(Examples in the illustration are the same as in Figure 5)

From Figures 5 and 6 it is clear that the actual measurement of the theoretical ratio of rough water surface reflected sound pressure is small. This is primarily due to the fact that the wave surface coordinate probability distribution tends to be a Gaussian distribution. Below it can also be seen that σ_{high} calculated according to the Gaussian probability density function is smaller than the σ_{wave} measured by the wave height meter.

3. Prediction of σ

On the basis of the relationship of $\ln(\bar{p}/p_0)$ and $2(\gamma\sigma)$ within the range $\gamma\sigma < 1$, acoustical methods can be used to measure the standard deviation of the wave surface undulations. Table 1 gives the reflected sound pressure measured in the experiment and the σ and σ_{high} calculated using Eqs. (4) and (7) and compares them with the σ_{wave} measured using the wave height meter.

Table 1. σ_{wave} Measured by the Wave Height Meter and the \bar{p}/p_0 Based on the Measurement and σ and σ_{high} Calculated Using Eqs. (4) and (7)

(1) 掠角 θ	(2) 声波频率 $f(\text{KHz})$	γ (cm^{-1})	$\frac{\bar{p}}{p_0}$	(3) σ_{high} (cm)	σ (cm)	(4) σ_{high} (cm)	C_s	C_E
30°	133	2.9	0.59	0.41	0.30	0.18	0.32	2.9
	111	2.3	0.53	0.49	0.42	0.24	0.40	2.9
	100	3.1	0.51	0.49	0.47	0.28	0.41	2.9
	74	1.6	0.63	0.45	0.51	0.30	0.29	2.8
	50	1.1	0.89	0.44	0.38	0.22	0.24	2.6
	41	0.9	0.84	0.43	0.55	0.32	0.19	2.8
45°	111	3.2	0.60	0.32	0.27	0.16	0.12	2.8
	100	3.0	0.67	0.29	0.26	0.15	0.06	2.9
	75	2.2	0.55	0.35	0.43	0.25	0.07	2.8
	38	1.1	0.92	0.37	0.31	0.18	0.04	2.6

Key:

- | | |
|-------------------------|---------------------------|
| 1. Glancing angle | 3. σ_{wave} |
| 2. Sound wave frequency | 4. σ_{high} |

From Table 1 it is clear that the σ_{high} calculated using the hypothesis of the Gaussian probability density function is generally larger than the offset of σ_{wave} and the σ measured using acoustical methods is rather close to σ_{wave} .

III. Conclusion

1. The wave surface coordinate probability distribution of rough water surface clearly influences the reflected sound pressure. In our experiments, the glancing angle was larger and the shielding effect should not play an important role. The difference between the $\ln(\bar{p}/p_0) \sim 2(\gamma\sigma)^2$ relationship obtained using the Gaussian probability density function and the experimental results is primarily due to the fact that the actual wave surface coordinate probability distribution tends to be a Gaussian distribution.
2. The standard deviation of the measured reflected sound pressure and the wave surface undulation calculated using the Gaussian probability density function is clearly smaller than the value measured using the wave height meter but the value of σ obtained by calculation according to Eq. (4) is basically the same as the latter. When the acoustical methods are used to measure standard deviation, the corresponding sound reflecting characteristics of different water surface situations should first be found.

REFERENCES

1. Wang Dezhaoh [3076 1795 2507] and Shang Erchang [1424 1422 2490], 1961. SHUISHENGXUE [AQUATIC ACOUSTICS], Kexue Chubanshe, pp 426-430.
2. Lin Shaogong [2651 1421 1362], 1978. JICHU GAILU YU SHULI TONGJI [BASIC PROBABILITY AND MATHEMATICAL STATISTICS], Renmin Jiaoyu Chubanshe, p 54.
3. Clay, C.S., H. Medwin, and W.M. Wright, 1973. SPECULARLY SCATTERED SOUND AND THE PROBABILITY DENSITY FUNCTION OF A ROUGH SURFACE, J. Acoust. Soc. Amer., 53:1677.
4. Eckart, C., 1953. THE SCATTERING OF SOUND FROM THE SEA SURFACE, J. Acoust. Soc. Amer., 25:566.
5. Huang, N.E., and S.R. Long, 1980. AN EXPERIMENTAL STUDY OF THE SURFACE ELEVATION PROBABILITY DISTRIBUTION AND STATISTICS OF WIND-GENERATED WAVES, J. Fluid Mech., 101:179.
6. Longuet-Higgins, M.S., 1963. THE EFFECT OF NON-LINEARITIES ON STATISTICAL DISTRIBUTIONS IN THE THEORY OF SEA WAVES, J. Fluid Mech., 17:459.

8226/6091
CSO: 4008/1093

CHARACTERISTICS OF 1.3 MICRON InGaAsP/InP DC-PBH LASER

Beijing BANDAOTI XUEBAO [CHINESE JOURNAL OF SEMICONDUCTORS] in Chinese Vol 7, No 3, May 86 pp 324-326

[Article by Zhao Songshan [6392 1529 1472], Wang Dechao [3769 1795 6389], Wu Youyu [0702 0645 1342], and Wang Yuzhang [3769 3786 4545] of Wuhan Research Institute of Post and Telecommunication: "A 1.3 Micron InGaAsP/InP Double-Channel Buried Heterostructure Laser"; paper received 22 April 1985]

[Text] Abstract: A 1.3 micron InGaAsP/InP double channel planar buried heterojunction laser device (DC-PBHLD) was fabricated by a super-cooling growth technique involving two liquid phase epitaxial (LPE) steps. The minimum threshold current at room temperature is 15 mA and the typical value is 20 mA. The maximum continuous working (CW) temperature is 80°C. The output power is 2 mW. At 4 times the threshold current, a stable longitudinal mode output could still be maintained.

The double channel planar buried heterojunction laser device (DC-PBH LD)¹ has an excellent current limiting P-N-P-N structure which is suited for continuous operation at low threshold current, high quantum efficiency and high temperature.

The process flow diagram of this DC-PBH laser is shown in Figure 1 and its structure is shown in Figure 1(e).

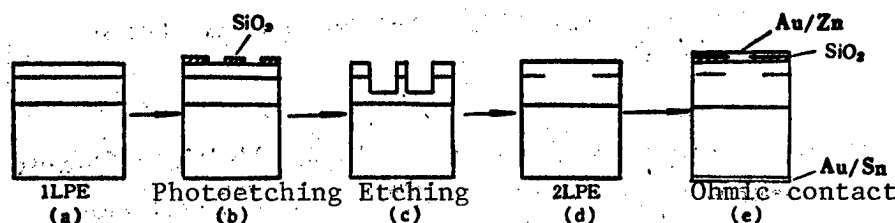


Figure 1. Process Flow of DC-PBH Laser

We employed a super-cooling growth technique. The first LPE step is to grow three layers on a Sn-InP (100) substrate: N-InP buffer layer ($1-2 \times 10^{18} \text{ cm}^{-3}$), undoped InGaAsP source layer and P-InP ($2-5 \times 10^{17} \text{ cm}^{-3}$) overlay. The wide contact threshold current density is approximately $0.7-2 \text{ KA/cm}^2$ and the

lasing efficiency is over 50 percent. SiO_2 is grown on top of the first LPE surface. The surface is photolithographically etched along the $\langle 011 \rangle$ direction. A $2\text{ }\mu\text{m}$ wide $2.5\text{ }\mu\text{m}$ deep platform was created by etching with HCl and bromomethyl alcohol^{2,3}. On either side of the platform, there is a $7\text{ }\mu\text{m}$ wide smooth bottom channel. The second LPE step grows four layers: P-InP ($1\text{--}3 \times 10^{17}\text{ cm}^{-3}$) and N^- -InP ($1\text{--}5 \times 10^{17}\text{ cm}^{-3}$) blocking layers, P-InP overlay and P^+ -InGaAsP (more than 10^{18} cm^{-3}) contact layer. A conventional ohmic contact technique was used. The P side is facing down and is soldered on a gold-plated copper heat sink.

The characteristics of this DC-PBH laser device are as follows:

1. Photoelectric Characteristics

The minimum threshold current at 20°C is 15 mA , the typical value is 20 mA and the linear laser power output is 2 mW ; as shown in Figure 2.

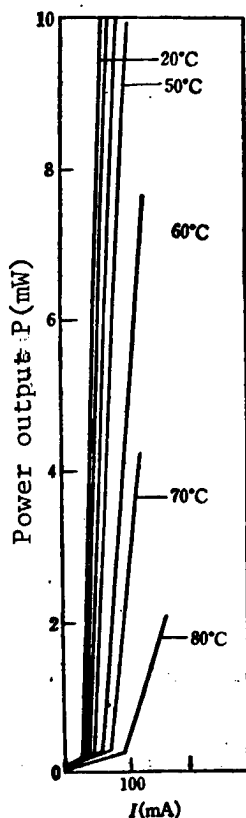


Figure 2. Light Intensity vs. Current

2. V-A Characteristics

The positive voltage drop at 1 mA is 0.8 volt . The minimum serial resistance is $R_s = 2.7\Omega$ and it is typically $3\text{--}4\Omega$. The reverse voltage drop at $1\text{ }\mu\text{A}$ is over 2 volts .

3. Spectral Characteristics

Figure 3 shows the laser spectra of the DC-PBH laser fabricated at different power output levels. When the injection current is between $1.3 I_{th}^{20^\circ C}$ and $4 I_{th}^{20^\circ C}$ (i.e., power output between 1 and 12 mW), it maintains a pure longitudinal lasing mode. The half width of the spectrum is less than 2 Å.

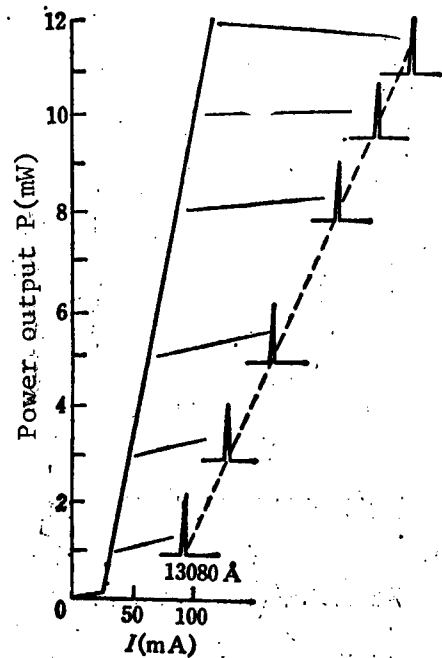


Figure 3. Spectra of DC-PBH Laser at Different Output Power Levels. Power Output 1-12 mW, Pure Longitudinal Mode.

4. Far Field Distribution

When the width of the DC-PBH laser is $1.5\text{--}2\text{ }\mu\text{m}$, the far field angle θ_{\parallel} and θ_{\perp} are almost equal. The light spot is circular. Figure 4 shows the far field distribution parallel to the junction surface at 1-10 mW. $\theta_{\parallel} \sim 13.5^\circ$. When coupling to an $0.2\text{ }\mu\text{m}$ diameter multi-mode optical fiber, the coupling efficiency reaches 90 percent.

If the width is less than $1\text{ }\mu\text{m}$, the behavior generally becomes poorer. The parallel and perpendicular far field angles θ_{\parallel} and θ_{\perp} increase and become unsmooth. In a few cases, double peak spectra were observed.

The authors wish to express their gratitude to Comrades Xu Guizhen [6079 2710 3791], Song Xianzeng [1345 2009 2582], Lin Liren [2651 4409 0088], and Wang Suqin [3769 4790 3830] for their assistance and support in the investigation.

The authors also wish to thank Comrades Wang Qimin [3769 0796 3046] and Peng Huaide [1756 2037 1795] for reviewing this manuscript.

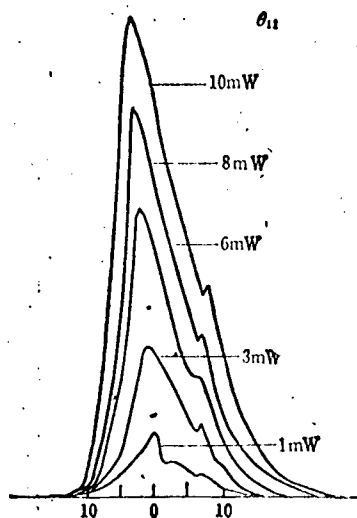


Figure 4. Distribution of DC-PBH Laser Parallel to the Junction ($T = 20^{\circ}\text{C}$)

REFERENCES

1. I. Mito, M. Kitamura, Ke. Kobayashi, and Ko. Kobayashi, ELECTRONICS LETTERS, 18, 953 (1982).
2. Sadao Adachi and Hitoshi Kawaguchi, J. ELECTROCHEM. SOC., 128, 1342 (1981).
3. L.A. Coldren, K. Furuya, B.I. Miller, and J.A. Rentchler, ELECTRONICS LETTERS, 18, 235 (1982).

12553/6091

CSO: 4008/1078

CHARACTERISTICS OF 1.3 MICRON TRANSVERSE InGaAsP/InP BH LASER

Beijing BANDAOTI XUEBAO [CHINESE JOURNAL OF SEMICONDUCTORS] in Chinese Vol 7, No 3, May 86 pp 337-339

[Article by Wang Wei, Zhang Jingyuan, Tian Huiliang, Wang Xiaojie, and the Device Technology Group at Institute of Semiconductors, Chinese Academy of Sciences: "A 1.3 Micron Low Threshold High Power Fundamental Transverse Mode BH InGaAsP/InP Laser"; paper received 18 December 1985]

[Text] Abstract: By using a two-step liquid phase epitaxial (LPE) process, we successfully developed a 1.3 micron low threshold current, high power output, fundamental transverse mode InGaAsP/InP BH laser. Its CW threshold current at room temperature is 10 mA and its single side differential quantum yield is 31 percent. The maximum linear power output is 20 mW*/facet. It can operate in a stable transverse mode at 2.5 times threshold current.

1. Device Structure

The structure of the BH laser device is shown in Figure 1. The source is buried in InP, which has a lower index of refraction among InGaAsP materials, to control the transverse mode¹. In the buried area, an InP junction in the reverse direction was prepared. A high impedance P layer is in contact with the source in order to have a good control of the current. The cross-sectional micrograph after the second epitaxy is shown in Figure 2. The source area of the laser is 0.3 μm thick and 2 μm wide. The cavity is 200-250 micron long. The preparation of the buried zone was reported in reference 2.

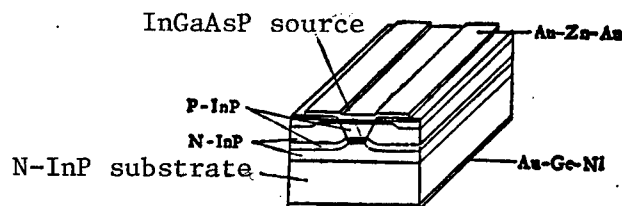


Figure 1. Schematic Diagram of the InGaAsP/InP Laser Structure

*The power output was determined by the Chinese Academy of Measurements.



Figure 2. Cross-Sectional Micrograph of the BH InGaAsP/InP Laser

2. Device Characteristics

The minimum CW threshold current of the 1.3 micron BH InGaAsP/InP laser under development is 15 mA. Typically, it is 20-30 mA. The maximum linear power output is over 20 mW/facet. The maximum single face differential quantum yield is 31 percent and it is typically 20 percent. The laser wavelength is 1.29-1.31 micron. The intensity vs. current curves at various ambient temperatures are shown in Figure 3. At 100°C, it still has a power output near 3 mW. Figure 4 shows the near range distribution of the device at different operating currents. It shows that the device can still operate in a stable transverse mode at 2.5 times the threshold current.

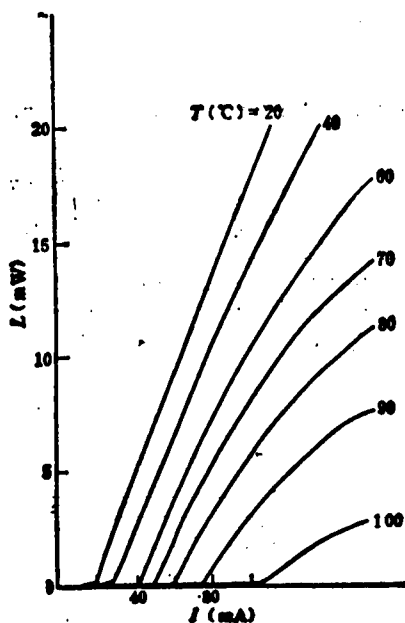


Figure 3. Light Intensity vs. Current at Different (Ambient) Temperatures

3. Conclusions

Recent experimental results show that our technique is repeatable. The yield of this low threshold device is high. Figure 5 shows the statistic CW threshold current distribution at 20°C of devices (256 in total which is

55 percent of the 446 core tubes made out of an epitaxial wafer (BH-135)). Our devices were aged at constant power at 50°C. Some have already passed 700 hours of test, equivalent to 10^4 hours of life at room temperature^{3,4}.

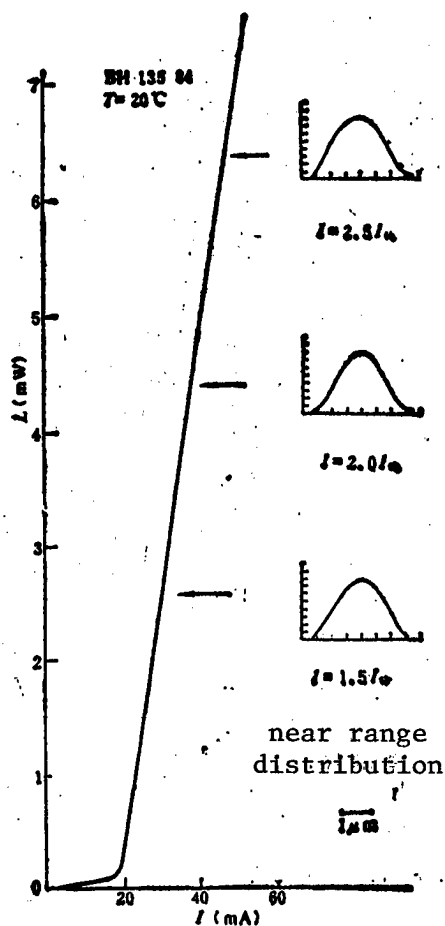


Figure 4. Near Range Distribution at Different Operating Currents

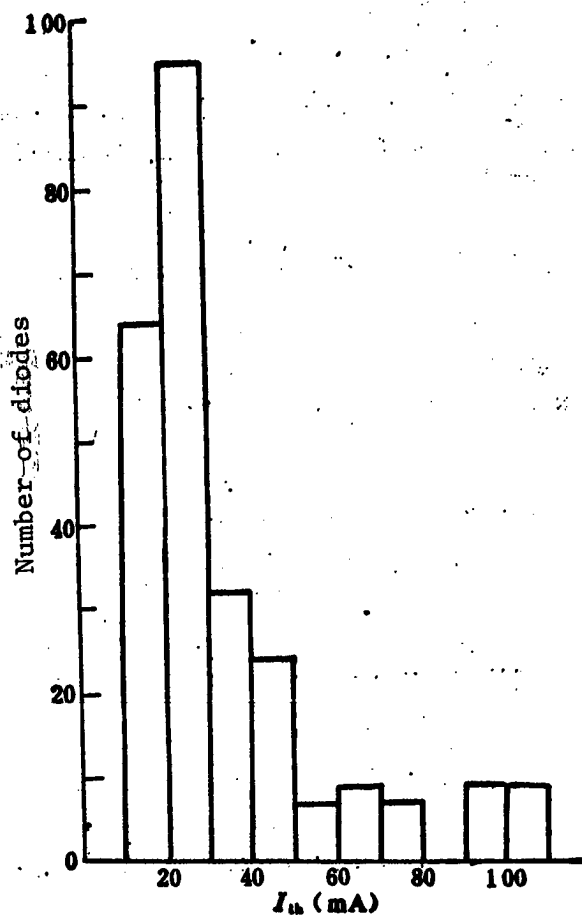


Figure 5. Statistical Distribution of Threshold Current at 20°C of Devices Made From BH-135 Epitaxial Wafer

REFERENCES

1. H. Kressel, J.K. Butler, Semiconductor Lasers and Heterojunction LEDs, Academic Press, §. 5.4 (1977).
2. Wang Wei, Zhang Jingyuan, Tian Huiliang and the Device Technology Group, this journal, 5, 679 (1984).
3. B.W. Hakki, P.E. Fraley, and T.F. Eltringham, AT&T TECHNICAL JOURNAL, 64, 771 (1985).

12553/6091
CSO: 4008/1078

HERMITIAN OPERATOR IN TENSOR PRODUCT SPACE DISCUSSED

Shanghai ZIRAN ZAZHI [NATURE JOURNAL] in Chinese Vol 9, No 5, May 86 p 394

[Article by Hu Shuan [5170 6615 1344], PLA Engineering College; Paper received 3 May 1985]

[Text] V is an n -dimensional unitary space. And $\otimes^k V$ is the k th tensor product space with the induced inner product defined on decomposable tensors $x^{\otimes} = x_1 \otimes \dots \otimes x_k, y^{\otimes} = y_1 \otimes \dots \otimes y_k$ by the formula $(x^{\otimes}, y^{\otimes}) = \prod_{i=1}^k (x_i, y_i)$.

K. Fan and Marcus [1, 2] have defined the numerical range of \mathcal{L} , the linear operator on $\otimes^k V$, as follows:

$$W^1(\mathcal{L}) = \{(\mathcal{L}x^{\otimes}, x^{\otimes}) | x_1, \dots, x_k, \text{ o. n.}\},$$

and studied a number of its basic properties.

Recently, Wang Boying [3769 0130 5391] [3] has proved that if $\mathcal{L} = A_1 \otimes \dots \otimes A_k, A_i \in L(V), i=1, \dots, k, k < n$, then \mathcal{L} is hermitian if $W^1(\mathcal{L}) \subseteq \mathbb{R}$. When $k = n = 2$, Wang argues that the above proposition is not true by presenting an invalid example. But he conjectures that the above proposition is still true when $k = n \geq 3$.

We proved Wang's conjecture by using the following lemmas:

Lemma 1. Let A, B , and C are three non-zero, non-scalar complex matrices. Then there exists a unitary matrix U such that all coefficients of U^*AU, U^*BU , and U^*CU are non-zero.

Lemma 2. Let $\mathcal{L} = A_1 \otimes A_2 \otimes A_3 - A_1^* \otimes A_2^* \otimes A_3^*$, Then $W^1(\mathcal{L}) = 0$, if $\mathcal{L} = 0$ in which $A_i \in L(V), \dim V = 3$.

It is not difficult to prove the following by induction.

Theorem 1. Let $\mathcal{L} = A_1 \otimes \dots \otimes A_n - A_1^* \otimes \dots \otimes A_n^*$, in which $A_i \in L(V), n \geq 3$. Then $W^1(\mathcal{L}) = 0$, if $\mathcal{L} = 0$.

Theorem 2. Let $\mathcal{L} = A_1 \otimes \dots \otimes A_n$, in which $A_i \in L(V)$, $n \geq 3$. Then $W^1(\mathcal{L}) \subseteq R$ if \mathcal{L} is hermitian.

FOOTNOTES

1. K. Fan, PROC. NAT. ACAD. SCI., U.S.A., 37 (1951) 760.
2. M. Marcus and B.Y. Wang, "LINEAR AND MULTILINEAR ALGEBRA," 9, 2 (1980) 111.
3. B.Y. Wang, SHUXUE NIANKAN [ANNALS OF MATHEMATICS], Vol A, No 6, 1 (1985) 79.

12922/7358

CSO: 4008/1085

PHYSICAL SCIENCES

COMPUTER SIMULATION OF LiF-CsCl SYSTEM BY MONTE CARLO METHOD

Shanghai ZIRAN ZAZHI [NATURE JOURNAL] in Chinese Vol 9, No 5, May 86 p 395

[Article by Chen Nianyi [7115 1819 6318] and Xu Chi [1776 7459], Shanghai Metallurgy Institute, Chinese Academy of Sciences, and Jiang Naixiong [3068 0035 7160], Shanghai Computational Technology Institute; Paper received 7 October 1985]

[Text] The Monte Carlo method is a very effective approach to study the structure of liquids and non-crystalline solids. Because ion pair potentials can be easily derived accurately, the computer simulation of ionic system is particularly successful. Though the simulation of two-dimensional system differs from the real system, it is valuable because its calculations are manageable and its results can be displayed on a plane so that changes can be observed directly. We have used the Monte Carlo method to simulate 64 two-dimensional ionic LiF-CsCl systems and observed their liquid structures and the process of the formation of "non-crystalline solid" by quick cooling. The Cs^+ , Li^+ , Cl^- , and F^- ions (treated as charged spheres with Pauling radii), 16 each, form an "ion cluster" with free boundary. Using the metropolis calculation method,^[1] the system at 1,300K reaches equilibrium after 10^5 operations. There is an obvious order in the distribution of ions at equilibrium: it can be roughly described as a mixture of the $\text{Li}_n^+\text{F}_m^-$ and $\text{Cs}_n^+\text{Cl}_m^-$ clusters. Most of the $\text{Li}_n^+\text{F}_m^-$ clusters are tightly packed with little space between Li^+ and F^- . The $\text{Cs}_n^+\text{Cl}_m^-$ clusters are relatively loosely packed with many holes inside. Individual ion clusters are not paired and there are many holes among them. Therefore, their free volume distribution is very uneven. At 1,300K, the total potential energy of the system is -719.08 kJ/mol.

Based on these, the process of the formation of non-crystalline solids by the quick cooling of liquids was simulated by computer. When the "liquid" reached equilibrium at 1,300K, the temperature term (TK) in the Boltzmann factor was substituted with 200K and the calculations were continued to simulate the quick cooling. The calculations show that the arrangement of ion changes rapidly when the temperature drops. After only 170 operations, the total energy drops from -719.08 to -750.73 kJ/mol and to -755.24 after 10,030 operations. After that, the change slows down rapidly. After 72,420 operations, it drops to

-759.34 kJ/mol. At the same time, the "area" of the ion clusters shrinks by about 10 percent and it becomes a "non-crystalline solid" with extremely slow relaxation.

It is generally believed that the structure of non-crystalline solids is the structure of liquid frozen by quick cooling. But actually only the "activation process" (e.g., the disruption of the existing clusters in liquids) that increases the total energy is frozen during quick cooling because the Boltzmann factor decreases. On the other hand, processes that cause a drop in total energy (e.g., opposite ions move closer to each other within a cluster to eliminate spaces between them) to speed up. The result is that the unpaired shrinking ion clusters are packed into a non-crystalline solid that lacks a long-range order.

FOOTNOTES

1. L.V. Woodcock and K. Singer, TRANS. FARAD. SOC., Vol 67, 1971 p 12.

12922/7358

CSO: 4008/1085

INJURY THRESHOLD OF SKIN IRRADIATED WITH 308-NM EXCIMER LASER LIGHT

Shanghai ZHONGGUO JIGUANG [CHINESE JOURNAL OF LASERS] in Chinese Vol 12 No 12
Dec 83 p 4

[Article by Li Zhaozhang [2621 0340 3864], Wu Jianu [0702 1367 1166] and Gai Baokang [5556 1405 1660], Laboratory of Laser Medicine, Shanghai No 2 Medical College, and Chou Zhengzhuo [0719 2398 0587], Shanghai Institute of Laser Technology]

[Text] ABSTRACT. Preliminary results of the use of an XeCl excimer laser to study ultraviolet erythema of the skin are reported. Using white pigs as test animals, it was found that the minimum reddening dose (MRD_{50}) was 45.97-63.05 mJ/cm² (95% confidence range).

Biological research on the effect of ultraviolet irradiation of the skin began in the early 20th century. The Danish physicist Niels Finsen was the first to use an artificial ultraviolet light source to treat patients suffering from the skin disease lupus. The West Germans Hausser and Vahle used a monochromatic light source consisting of a low-pressure mercury lamp and two quartz prisms for a detailed investigation of the effect of ultraviolet light of various wavelengths on human skin; they noted that erythema of the skin was produced most readily in the vicinity of 300 nm. In the 1930's Coblentz et al. measured the ultraviolet erythema producing spectrum and found that ultraviolet light between 200 and 280 nm produced distinct instantaneous erythema, while light at 254 and 297 nm most readily produced delayed erythema. In 1965, Everett et al. used a monochromatic source consisting of a xenon arc lamp and an optical grating to determine the erythema effect curve for humans in the range between 250 and 310 nm. They discovered that as the wavelength of the ultraviolet light increased, the minimum amount of energy needed to produce erythema also rose. When the wavelength was above 300 nm, the erythema-producing effect clearly decreased. In the 1970's, Parrish used a molecular nitrogen laser to irradiate the skin of white subjects and determined that the minimum exposure from a pulsed N₂ laser that produced erythema was 21.6±4.8 J/cm². Aufmuth (1979) reported the effect of a dye laser (tunable between 260 and 345 nm) on human skin; he determined that the

minimum reddening dose (MRD) for 300-nm ultraviolet laser light was 5 mJ/cm². Recently, Anderson and Parrish have begun research on the effect of short-pulse ultraviolet laser light on human skin. They have discovered that light-induced chemical reactions play an important role in the ultraviolet erythema reaction.

We have seen no reports, either Chinese or foreign, of experiments on the damage threshold for the exposure of skin to 308-nm excimer laser light. Research in this area is much needed in order to establish laser safety standards for China.

1. Materials and Method.

We used an XeCl excimer laser as a radiation source. The laser wavelength was 308 nm, the pulse width was 15 ns, and the maximum single-pulse output was 100 mJ; the dispersion angle was 12.8 mrad in the long-axis direction and 7.1 mrad in the short-axis direction.

The optical circuit of the irradiation device is shown in Fig. 1. During the experiments, the irradiation level was calculated from the energy meter reading and the beam-splitting ratio ($K = 2.1 \pm 0.087$). The energy meter that we used had been calibrated by the State Metrological Institute.

The environmental conditions were: room temperature $25 \pm 1.1^\circ \text{C}$, humidity $79.3 \pm 8.4\%$.

As experimental animals we used three Shanghai white pigs, each weighing 5.5 kg. Two hours before exposure they were anesthetized with 1 ml/kg of a 2.5% sodium amytal solution administered intraperitoneally, after which the skin was washed with warm water and soap. A surgical scalpel was used to shave off the bristles on the back. Forty 2x2 cm squares were drawn on both sides of the back 2 cm from the spine and the laser beam was directed onto the center of each square through a diaphragm 5 mm in diameter.

The erythema inspection was made primarily with the naked eye (the identification standard is not described here). The damage threshold under study in this experiment is indicated by a positive result for erythema (+); we sought the irradiation level at which there would be 50 percent positive results for erythema 24 hours after exposure. Seven exposure groups were examined under an optical microscope at different time intervals following exposure; the groups that were close to the damage threshold were also examined under the electron microscope.

A total of 230 spots were irradiated, of which 18 were used for histological examination; the other 212 points were subjected to probability analysis by group. The weighted regression method (on a PDP-11-23 computer) was used to obtain the minimum reddening dose for white pig skin for a 308-nm excimer laser (MRD₅₀) and the 95% confidence range.

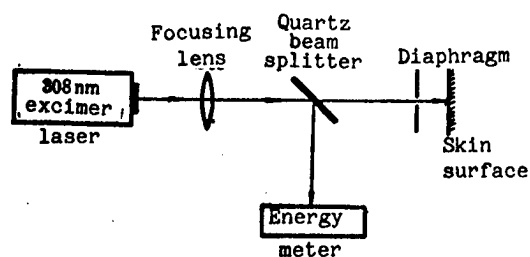


Fig. 1. Optical circuit of experimental apparatus

Table 1. Instantaneous erythema following exposure of pig skin to 308-nm excimer laser light

Exposure group	Avg. exposure \pm std. deviation, mJ/cm ²	Number of points exposed	Instantaneous erythema			Outcome
			Occurrence rate, %	Time to appear, seconds (") after exposure	Persistence, min ('), sec (")	
1	22.28 \pm 2.26	82	—	—	—	—
2	29.44 \pm 1.80	82	—	—	—	—
3	39.76 \pm 3.85	80	83.83	9"~18"	49"~2'17"	\pm
4	58.56 \pm 5.19	81	41.94	7"~12"	1'28"~2'26"	\pm
5	69.14 \pm 4.51	27	70.87	4"~13"	1'54"~5'	+
6	91.27 \pm 1.96	80	83.83	5"~15"	45"~8'42"	+
7	106.17 \pm 3.18	80	100.00	instantaneous to 15"	89"~10'	++

Table 2. Delayed erythema following exposure of pig skin to 308-nm excimer laser light

Exposure group	Avg. exposure \pm std. deviation, mJ/cm ²	No. of points exposed	No. of erythema points 24 hours after exposure	Delayed erythema rate, 24 hrs, %	Outcome
1	22.38 \pm 2.26	82	5	15.63	\pm
2	29.44 \pm 1.80	82	9	23.18	\pm
3	39.76 \pm 3.85	80	11	36.67	\pm^+
4	58.56 \pm 5.19	81	14	45.16	+
5	69.14 \pm 4.51	27	15	55.56	++
6	91.27 \pm 1.96	80	22	73.83	++
7	106.17 \pm 3.18	80	25	83.33	+++

2. Results and Analysis

Tables 1 and 2 present data on instantaneous and delayed reddening of skin after irradiation with 308-nm laser light. The delayed erythema generally appeared 8 to 9 hours after exposure, but in groups 6 and 7 it appeared at some irradiated locations 5 after exposure. The number of erythema spots reached a peak in all erythema groups 24 hours after irradiation, with a rather deep color; the spots generally persisted for 2 to 3 days. The spots in the sixth group had already become pigmented 48 hours after exposure, with the pigmentation persisting for 6 to 14 days. Scabs formed on about 63 percent of the delayed erythema spots in group 7.

The results of standard histological examinations of the skin of the exposure groups were as follows: sections of the delayed erythema points 24 hours after irradiation showed no evident signs of reaction in the first group; in groups 2-4 the capillaries in the dermis were dilated and congested to various degrees and small numbers of erythrocytes had been exuded. In the fifth group, in addition to the above phenomena, lymph cells appeared in the vicinity of the blood vessels. In group 6 the dermis contained exterior acervate inflammation cells; in group 7 the basal cells showed intracellular edema accompanied by small numbers of vacuoles, and the cells were rather loosely arranged. More detailed information is presented in the photographs (a-d). In groups 3, 4 and 5 the instantaneous erythema was studied under the optical and electron microscopes. The basic structure was normal. Photographs e and f are from the electron microscope examination.

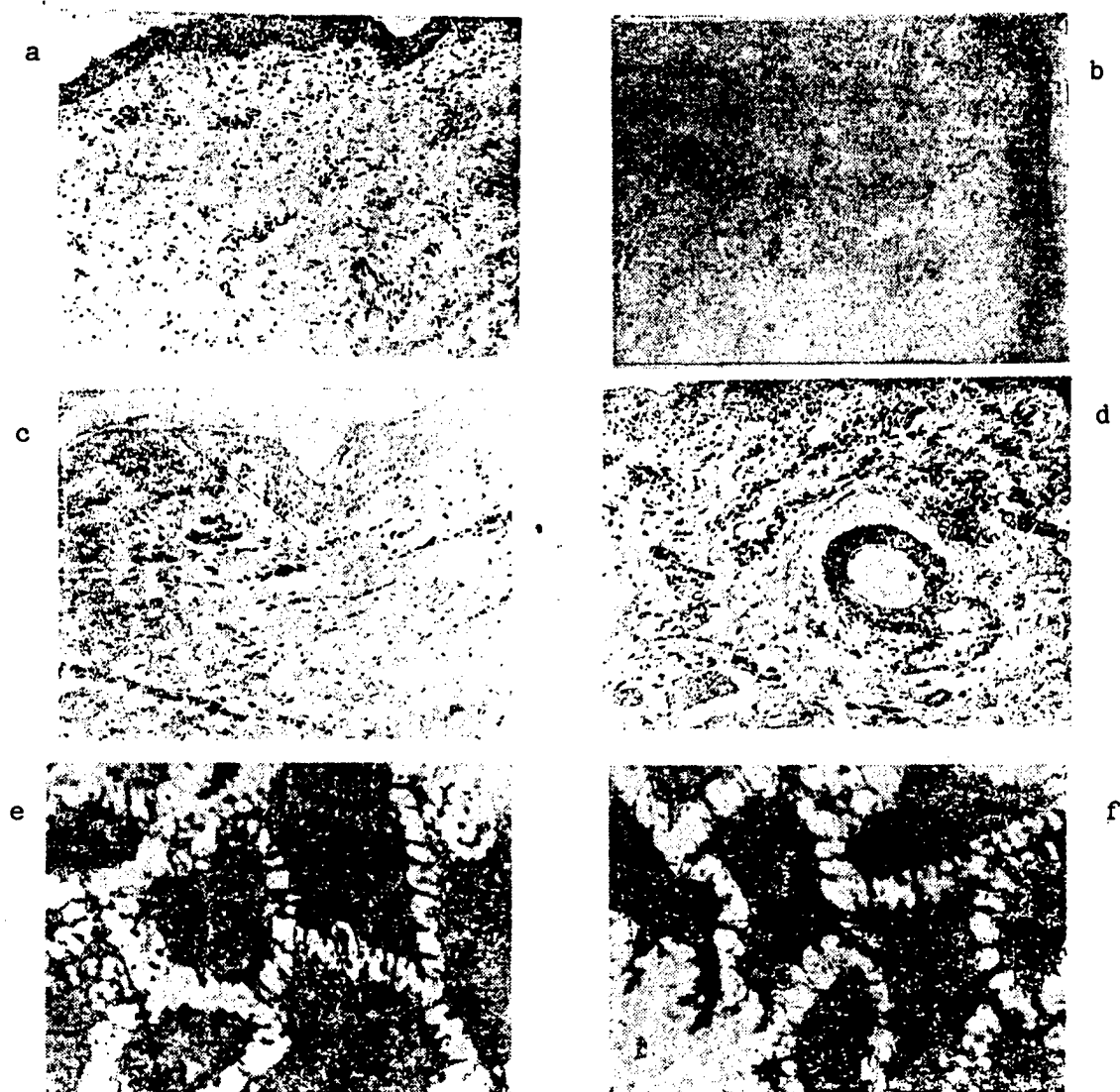
The MRD_{50} values and 95 percent confidence limits for irradiation with 308-nm laser light based on visual determination and weighted regression analysis are presented in Table 3 and Fig. 2.

The x axis is the logarithm of the exposure, while the y axis gives the delayed erythema occurrence probability. A chi-square test of the regression formula shown in the table gave satisfactory results.

3. Discussion

a. Two-Phase Erythema Reaction Produced by Short-Pulse Ultraviolet Laser Light

Ultraviolet irradiation causes a two-phase (instantaneous and delayed) skin erythema reaction, which was clearly evident in our experiment. The instantaneous erythema produced by 308-nm laser light appeared early and cleared up rapidly, persisting no longer than 15 minutes. This phenomenon may be produced by the pressure effect of short-pulse ultraviolet light: only when the pressure reaches some threshold value is blood vessel permeability altered, producing the instantaneous reaction. The delayed erythema appears only after a certain time interval: this is a characteristic of optically induced chemical reactions. Some foreign investigators have reported that histamine, serotonin, kinins and prostaglandins (E, F and G) may be the



Photographs. (a) Histologic examination of tissue of group 4, 24 hours after exposure (HE stain). Capillaries of dermis dilated and congested. (b) Histologic examination of tissue of group 5, 24 hours after exposure (HE stain). Capillaries of dermis dilated and congested. (c) Histologic examination of tissue of group 6, 24 hours after exposure (HE stain). Capillaries of dermis dilated and congested. Edema of epidermal cells. (d) Histologic examination of tissue of group 7, 24 hours after exposure (HE stain). Capillaries of dermis dilated and congested. Acervate inflammation cells. Edema of epidermal cells. (e) Specimen taken 5 minutes after level IV exposure. Gaps between epidermal prickle cells widened (electron microscope, 11,200X). (f) Specimen taken 5 minutes after level V exposure. Gaps between epidermal prickle cells widened (electron microscope, 11,200X).

products of the photochemical reaction that cause the delayed reaction. To gain a further understanding of the mechanism of ultraviolet-produced erythema, biochemical studies will be needed.

Table 4. Probability analysis of skin damage to white pigs resulting from exposure to 308-nm laser light

	Visual inspection	Weighted regression method
Regression formula		$y = 0.4759 + 2.6184x$
MRD ₅₀ (mJ/cm ²)	53.09	53.84
95% confidence interval, mJ/cm ²	43.36~65.00	45.97~63.05

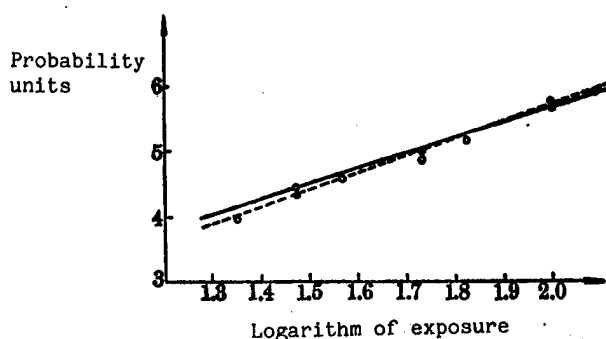


Fig. 2. Probability of development of erythema versus logarithm of exposure

Solid line represents results of visual examination; dashed line is weighted regression lines. Open circles represent experimental points, dark circles represent values calculated from weighted regression formula.

b. The Minimum Reddening Dose (MRD) and Laser Protection Standards

This experiment used white pigs to determine the damage threshold for the irradiation of skin with 308-nm pulsed ultraviolet laser light. MRD₅₀ was 53.84 mJ/cm², i.e. spots receiving this dose had a 50% probability of erythema. Similarly, from the regression equations we can also determine that the dose at which there will be a 10% incidence of erythema (MRD₁₀) is 6.91 mJ/cm². In existing international laser protection standards (IEC, ANSI, WHO Environmental Protection Standard 23 and the like), the maximum permissible irradiation dose for 308-nm pulsed laser light is 6.19 mJ/cm². The MRD₁₀ value is only 10% higher than the MPE (maximum permissible exposure), indicating that the boundary between nominal safety and possible damage is unclear. Consequently, to assure safety when using supershort-pulse ultraviolet lasers, reference must be made to existing maximum permissible exposure standards.

References omitted.

PICOSECOND, FEMTOSECOND SPECTROSCOPY IN SEMICONDUCTORS

Shanghai HONGWAI YANJIU [CHINESE JOURNAL OF INFRARED RESEARCH] in Chinese
Vol 4 No 6, Dec 85 pp 457-468

[Article by Xu Zhongying [1776 0112 5391], Institute of Semiconductors,
Chinese Academy of Sciences: "Picosecond and Femtosecond Spectroscopy in
Semiconductors"; Paper received 12 February 1985; revised manuscript received
29 May 1985]

[Text] Abstract: This paper describes various time-resolved nonlinear optical
techniques which are applicable to semiconductors, such as hot luminescence
correlation technique, transmission correlation technique, population mixing
technique, up-conversion gate, and pump-probe technique. The examples of
their applications to semiconductors are given.

I. Introduction

The development of modern picosecond (ps) technology provided an extremely
useful tool for research on fast nonequilibrium phenomena. These fast nonequi-
librium processes are generally extremely short, from several hundred pico-
seconds to several tens of femtoseconds (fs). This time domain has special
significance for solid-state physics. Many important physical phenomena, such
as thermoelectron relaxation, nonequilibrium thermophonon relaxation, and the
electron-hole collision process, occur within several picoseconds or even
shorter times.

When semiconductor material is excited by photons with energy of $h\nu_0$, a large
amount of nonequilibrium hot carrier¹ is produced. These hot carriers possess
extra energy $h\nu_0 - E_g$, in which the electron extra energy is $\Delta E_g = (h\nu_0 - E_g) \times$
 $(1 + m_e/m_h)^{-1}$. These high excitation state thermoelectrons can rapidly lose
their extra energy and relax to the bottom of the conduction band. Studying
the relaxation process of these thermoelectrons can provide much information
on the electron-electron and electron-phonon interaction in semiconductors.

Generally speaking, under the action of an extremely short light pulse, high
excitation state nonequilibrium carriers first of all go through carrier-
carrier scattering, plasma yuan [0337] emission and LO phonon scattering to a
quasi-equilibrium state. At this time the electron temperature is much higher
than the temperature of the crystal lattice, the relaxation process is extreme-
ly short, as the latest experimental measurements have shown,² in GaAs,

$\text{Al}_{0.32}\text{Ga}_{0.68}\text{As}$ and GaAs duoliangzijing [1122 6852 1311 7088] structures are 35, 60, and 50 fs, respectively. Under the action of a picosecond laser pulse, experimentally, there is no way to observe the above-described femto-second relaxation process. The thermoelectrons produced by excitation are already in a quasi-equilibrium state, and the electron temperature is much higher than the crystal lattice temperature. The relaxation process after this is carried out primarily through emission of phonons, and the relaxation time is from several picoseconds to several tens of picoseconds determined by crystal lattice temperature, excitation intensity, electron energy, etc. The above-described relaxation process can be illustrated by Figure 1.

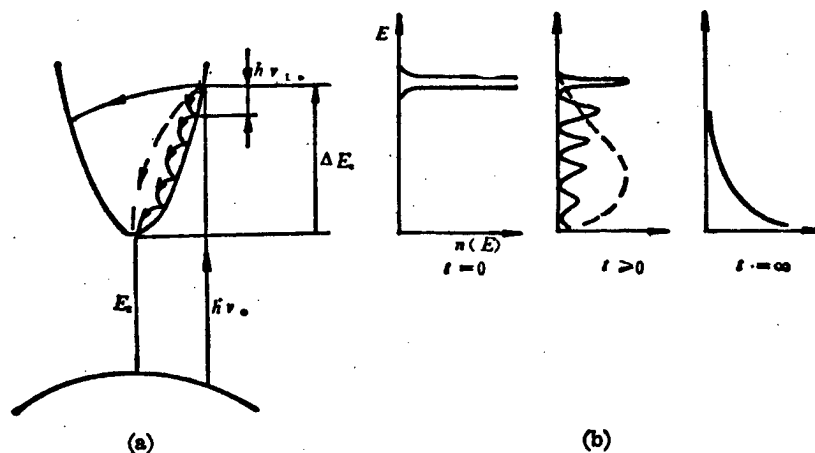


Figure 1. Schematic Drawing Showing (a) Various Relaxation Process Following Ultrafast Laser Pulse; (b) Carrier Distribution at Different Time Delays

The aim of this paper is to introduce the application of picosecond and femto-second laser spectroscopy in research on semiconductor physics, and to give some representative recent research results.

II. Picosecond and Femtosecond Lasers

To produce an ultrafast laser pulse it is necessary to use laser mode-locked technology. There are now several mode-locked lasers which produce ultrafast laser pulses of several hundred ps to 12 fs. Table 1 sets out the primary characteristics of various primary ultrafast pulse lasers.

Synchronous pump dye lasers and colliding pulse mode-locked dye lasers can produce continuous pulse sequence, high repetition frequency and permit use of signal averaging technique and are already widely used in measuring fast relaxation processes. The synchronous pump dye laser also has such advantages as a large tuning range, broad wavelength fugai [1788 5556 covering?] range, and can simultaneously synchronously pump two or even many dye lasers to implement synchronous output of many wavelengths. When an unusually high excitation is required (such as when studying such physical processes as

Table 1. Characteristics of Various Ultrafast Laser Systems

Laser type	Nd glass	YAG	Dye	Dye	Dye	Dye	Argon ion
Excitation mode	Flash-lamp	Flash-lamp	Flash-lamp	Continuous laser	Mode locked laser	Continuous laser	Discharge
Repetition frequency	0.1/s	10/s	10/s	Continuous	Continuous	Continuous	Continuous
Mode locked mode	Passive	Passive	Passive	Passive	Synchronous pump	Colliding pulse mode locked	Active
Working wavelength (nm)	1,060	1,060	450-800	580-620	420-900	620	515, 488
Pulsewidth (PS)	6-8	30	2-5	0.2-1.5	0.5-50	0.012 (0.55)*	150
Peak power	10^7	10^7	10^6	10^2	10^3	10^2	10^2

*12 fs is the latest result of Dr J.M. Halbout of IBM, and is currently the shortest light pulse. The system uses pulse compression technology. 55 fs is a research result reported by Cornell University's Professor Tang Zhongliang [3282 0112 5328] who has not yet adopted pulse compression technology.

exciton molecules and electron-hole drop) frequently a high power Neodymium glass and YAG solid-state laser is used.

The colliding pulse mode locked laser was proposed in 1981 by R.L. Fork, et al.,³ of Bell Laboratories. This is a ring laser. Within the chamber there are two pulses propagated in opposing directions precisely synchronous in saturation absorber. To produce a transient standing wave light field, a transient gate of absorber molecule and particle distribution thus effectively reduces loss within the chamber and functions as a synchronous, stable, compressed laser pulse. The greatest characteristic of this laser is that its structure is simple (see Figure 2) consisting of a continuously operating argon ion laser, gain dye jet (R6G, 40-50 μm) and saturation absorbing dye jet (DODCI, 10 μm). Its output pulse width is 100 fs, but using pulse compression technique the pulse width can be further reduced.

III. Measuring Technique and Its Application in Semiconductor Physics

Up to now there has not been a picosecond-femtosecond photoelectron detector. The only electronic device which can record picosecond processes is the streak camera, but this device is high-priced, has low resolution, and the stability and life are not very ideal.

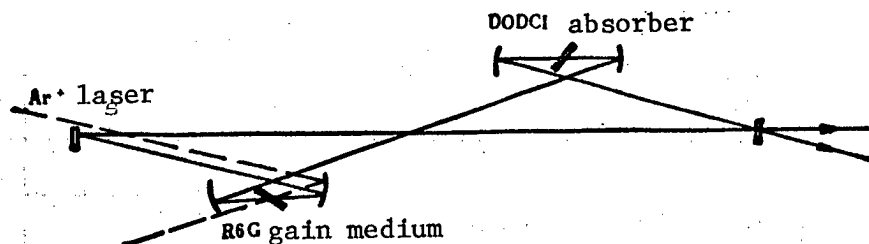


Figure 2. Schematic Representation of Colliding Pulse Mode-Locking (CPM) Dye Laser System

At present in ultrafast laser pulse measurement technique, nonlinear optical measurement technology, common correlation measurement technique, frequency up-conversion technique, and pump-probe technique are mainly used.

1. Correlation Measurement Technique

Correlation measurement technique is a newly developed picosecond spectral measurement technique which is very similar to the autocorrelation measurement technique used to measure picosecond laser pulses themselves. Here we will introduce photoluminescence correlation measurement technique,² and population mixture technique,⁵ and provide the experimental results of their use in measuring thermoelectron relaxation in GaAs and GaAs duoliangzijing and heavy doped P-GaAs shaozi [1421 1311] life.

(1) The photoluminescence correlation measurement setup is as illustrated in Figure 3. The 5 ps, 10^8 Hz laser pulse series emitted by the synchronous pulse dye laser (DCM dye, 650 nm) is divided by the polarizing prism into two beams of equal intensity and perpendicular polarized direction and after introducing a time delay τ , the two beam pulses may merge through a focused excitation sample, after the sample is excited it produces a large volume of thermoelectrons, and the thermoelectrons quickly relax to the bottom of the conductive band. Although the relaxation velocity far exceeds the radiative recombination velocity, there still exists a transition in the high energy band which forms a high energy tail in the photoluminescence spectrum (illustrated in the inset in Figure 3). Due to the dual molecular characteristic of the recombination luminescence, the luminescence intensity displays a nonlinear relationship with the excitation intensity, thus when the two pulses coincide ($\tau = 0$), the luminescence intensity intensifies the nonlinearity forming a hot luminescence correlation peak. Any change in the thermoelectron distribution is reflected in the luminescence correlation signal intensity. When τ greatly exceeds the thermoelectron relaxation time, the correlation peak disappears, and in experiments only DC background is seen. The relationship between luminescence correlation peak and the delay time τ between the two pulses can be expressed

$$PL(\tau) \sim \int_{-\infty}^{\infty} dx \exp(-|x|/T_e) AO(\tau - x), \quad (1)$$

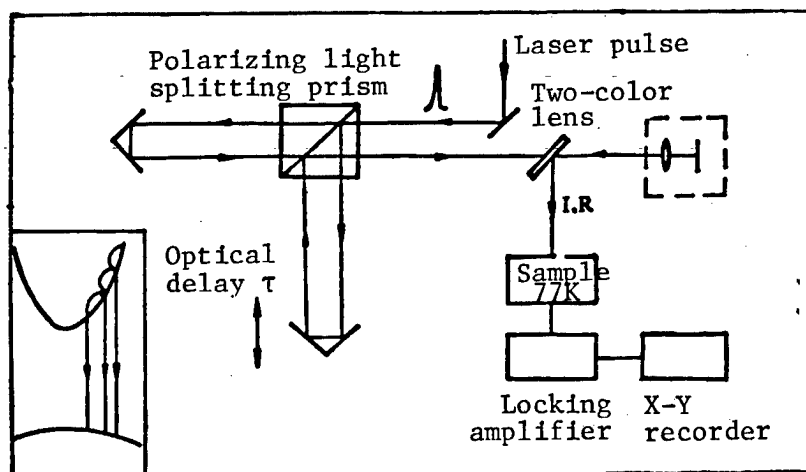


Figure 3. Experimental Setup of Hot Luminescence Correlation Technique

in which x is any variable, T_e is the thermoelectron relaxation time constant, $AO(\tau) = \int_{-\infty}^{\infty} dt I(t+\tau)I(t)$ is the correlation function of the laser pulse in which $I(t)$ and $I(t + \tau)$ is the intensity of the two pulses.

Equation (1) was derived on the basis of the changes in the time of carrier occupation density, and shows that the luminescence correlation signal is the convolution of the laser pulse autocorrelation function and the exponential function of time constant as T_e . When the laser pulse is far smaller than the thermoelectron relaxation time, $PL(\tau)$ is the time constant equivalent to the exponential function of electron relaxation time T_e ; yet when the electron relaxation function and the laser pulse width are analogous, it is necessary to solve the correlation function to find the relaxation time. The results of relaxation process of thermoelectrons experimentally measured in GaAs and GaAs-GaAlAs duoliangzijing showed that:

a) Under the same excitation conditions, the cooling velocity of thermoelectrons in liangzijing [6852 1311 7088 literally "quantum trap"] structures is slow and the relaxation time is long. This is because in the cooling process, the thermoelectrons emit a large amount of LO phonons, and the multilayered boundaries of the liangzijing material causes the thermoelectron system to encounter obstacles in crystal lattice energy conversion. Figure 4 is a typical hot luminescence correlation curve. The black dots in the figure represent the computer results, from the figure we obtain a 4.8 ps relaxation time for the GaAs semiconductor material thermoelectrons and 35 ps for the liangzijing structure.

(b) The electron relaxation velocity of different energy positions is different, thus this method can be used to conveniently study the relaxation processes of electrons in different energy states. Figure 5 illustrates the relaxation process of thermoelectrons of different energies in a GaAs

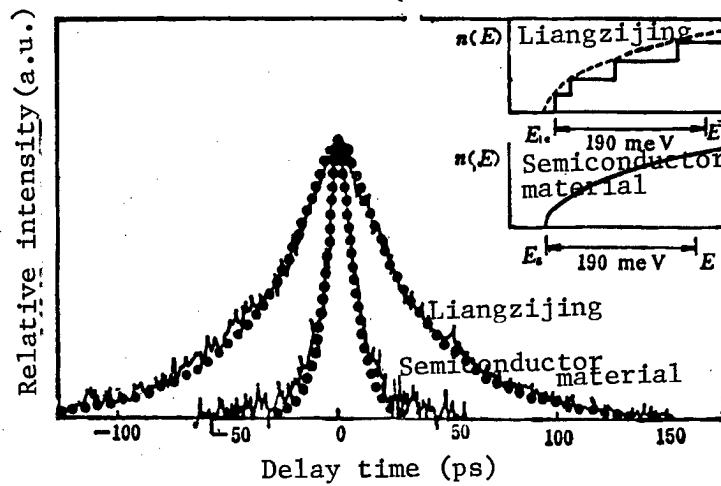


Figure 4. Typical Hot Luminescence Correlation Peaks of QW GaAs and Bulk GaAs

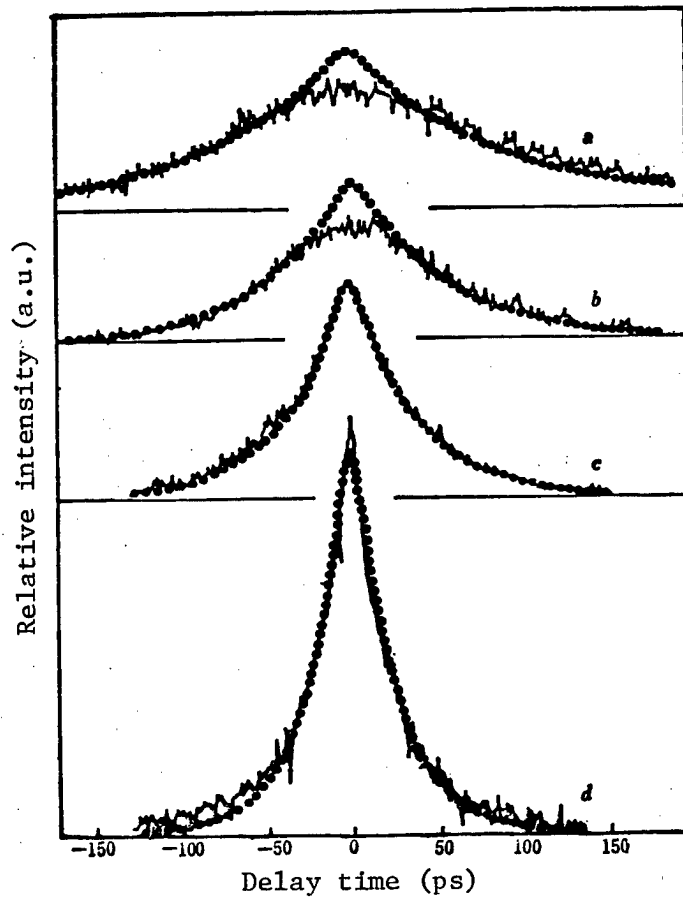


Figure 5. Comparison of Hot-Luminescence Correlation Peaks at Different Photon Energies for GaAs QW Under the Excitation Intensity of $\sim 3.8 \times 10^{18}/\text{cm}^3$

(a) $E_{1s} = 117 \text{ meV}$, $\tau_r = 84 \text{ ps}$; (b) $E_{1s} = 150 \text{ meV}$, $\tau_r = 51 \text{ ps}$;
(c) $E_{1s} = 190 \text{ meV}$, $\tau_r = 35 \text{ ps}$; (d) $E_{1s} = 220 \text{ meV}$, $\tau_r = 23 \text{ ps}$

liangzijing, the black dots in the illustration represent the computer results, the theoretical computation of polarization of the experimental curve near the low energy state $\tau = 0$ is created by the filling effect of the electrons going from high energy state to low energy state.

(c) The thermoelectron relaxation time is related to the excitation level: under high excitation, the relaxation process is slow. This is because the electron-phonon system screen greatly reduces the energy exchange between the carrier and the crystal lattice. Figure 6 summarizes the experimental results. In the figure, the numbers represent the energy of the electrons under study and it can be seen that at low excitation ($\sim 10^{17} \text{cm}^{-3}$) the relaxation time of the semiconductor materials and the liangzijing structure tend to be the same. If we use a CPM laser with a pulse width of 0.1 ps to replace the synchronous pump dye laser with a pulse width of 5 ps, we can observe the correlation peaks illustrated in Figure 7. Based on the above principles, we can obtain a relaxation time of the electron from high excitation state to quasi-equilibrium state of approximately ~ 100 fs. In addition, we also observe that when the excitation intensity increases, wings appear on the two sides of the correlation peak, the time constant is approximately 1 ps, the relative intensity increases as the excitation intensity increases, and it is the function of electron energy. When energy is low, the relative intensity of the wings increases.

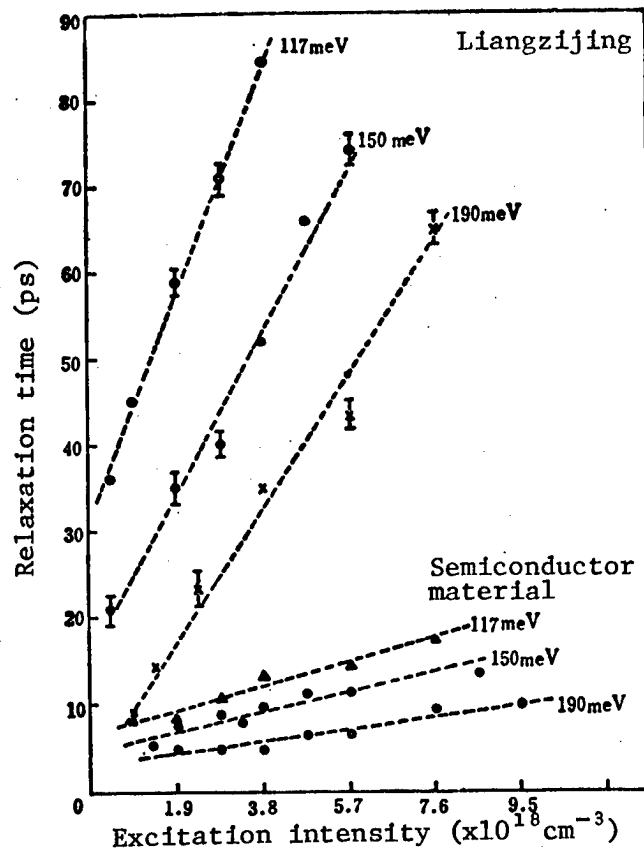


Figure 6. Hot Carrier Relaxation Time vs. Excitation Intensity for Both QW and Bulk GaAs at Different Energies

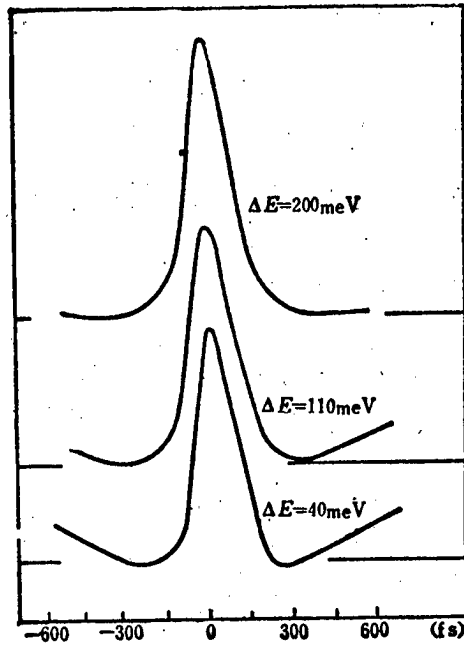


Figure 7. Rising Wings Due to Band-Filling Effect

The wings are formed because in the central energy valley electron relaxation, the electrons initially scattered to the energy valley jointly occupied by L and X largely leak towards Γ energy valley and produce the energy band filling effect. As it draws close to the bottom of the conduction band, the energy band filling effect becomes clear and the resultant relative intensity of the wings increases.

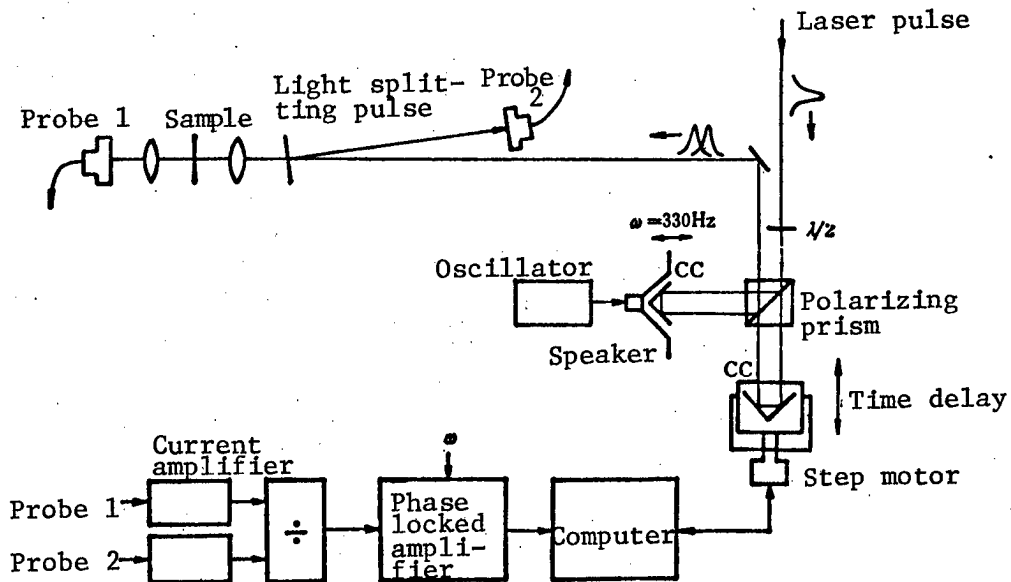


Figure 8. Experimental Setup for Transmission Correlation Technique

(2) Transmission correlation measurement technique is based on the absorption saturation effect,² see Figure 8. The coaxial focused excitation sample after the ~ 100 fs, 80 MHz laser pulse emitted by the CPM laser has undergone polarizing beam-splitting and time delay, the DC probe system probes the overall transmission intensity of the two pulses through samples. To improve the sensitivity of the probe and reduce noise the differential reception technique was adopted. The differential signal is as illustrated in Figure 9(a). Figure 9(b) is the transmission correlation peak after integration. The broken line is the autocorrelation signal of the laser pulse. The overall transmission intensity measured with changes in the delay time τ can similarly be expressed in the form of Equation (1).

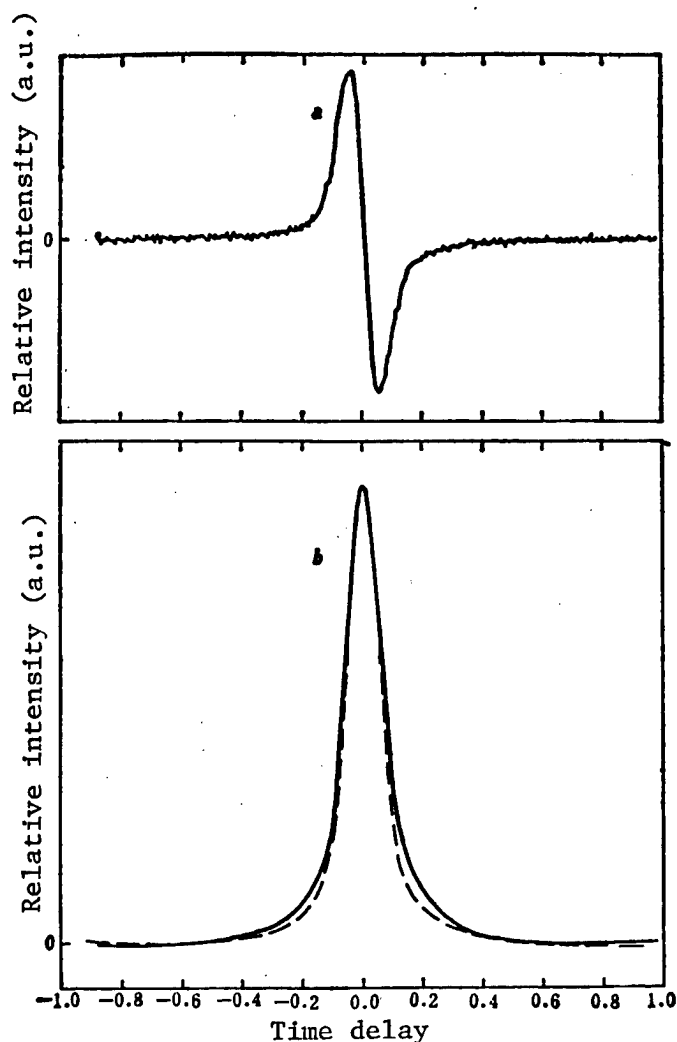


Figure 9. Transmission Correlation Curve
 (a) The derivative dither trace of transmission correlation peak;
 (b) The corresponding integrated curve of transmission correlation peak

The femosecond relaxation processes measured in GaAs, $\text{Ga}_{0.68}\text{Al}_{0.32}\text{As}$ liangzi-jing structures were 35, 60, and 50 fs, respectively. Note that these values are much smaller than the width of the 100 fs laser pulse itself. The energy of the photon emitted in the experiment was 2.02 eV, the emission intensity was $\sim 10^{17} \text{ cm}^{-3}$. This is the fastest relaxation time measurement at present. Wings on both sides of the correlation peaks were also observed in transmission correlation measurement. Their time constant was 1 ps.

(3) Population mixing technique is another correlation measurement technique used for measuring the carrier dynamics in semiconductors. As illustrated in Figure 10, after two laser pulses of equal intensity go through time delay τ , an excitation semiconductor sample is focused, producing photoluminescence. The two laser beams are modulated by a chopper which uses different frequencies, when the phase locked amplifier is adjusted to slip frequency (sum frequency) frequency, one can probe the transition which occurs between the electrons produced by the excitation of one beam and the hole produced by the excitation of the other beam and the electron-hole combined luminescence signal excited by the same laser pulse is isolated by heterodyne receiving technique. Supposing the background electron and hole concentration of the material is n_0 and p_0 , the concentrations of the carrier produced by the first laser pulse are $n(t)$ and $p(t)$, the concentrations of the carrier produced by the second laser pulse are $n(t + \tau)$ and $p(t + \tau)$, the overall combined luminescence intensity is

$$I(t, \tau) \sim [n(t + \tau) + n(t) + n_0] [p(t + \tau) + p(t) + p_0] \quad (2)$$

Since heterodyne reception was adopted, the signal intensity obtained was

$$I(\tau) \sim \int_{-\infty}^{\infty} n(t + \tau) p(t) dt + \int_{-\infty}^{\infty} n(t) p(t + \tau) dt, \quad (3)$$

i.e., the luminescence signal measured is in direct proportion to the correlation function of the carrier density, and clearly also is the correlation function of the delay time of the two laser pulses.

Rosen et al.⁵ used this technique to measure the life of a few carriers in highly doped P-GaAs (Zn: $6 \times 10^{18} / \text{cm}^3$). The laser used was a ring type dye laser (<0.5 ps, 610 nm). The results of the experiment are given in Figure 11. The electron life obtained was 39 ± 7 ps.

2. Frequency Up-Conversion Technique

The frequency up-conversion technique is also called the optical sum frequency technique. It uses ultrafast pulse as a time gate to measure the time change process of transient processes. Compared with the optical Kerr-cell, the frequency up-conversion technique is suitable for use in medium power, highly repetitive frequency continuous output pulse lasers (such as the synchronous pump dye laser) where the measurement signal may be very weak, the wavelength partition capability is strong, and the time-resolved precision is limited by the width of the laser pulse, thus it is especially suited to time-resolved spectrum measurement.

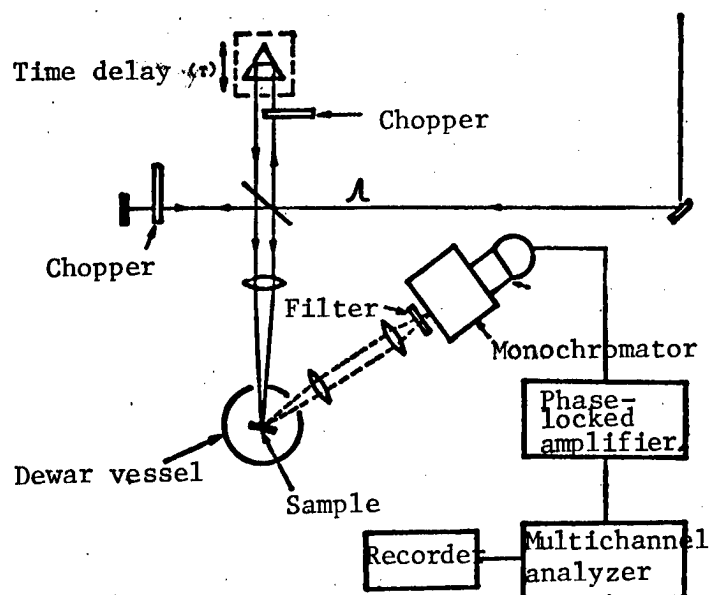


Figure 10. Schematic Diagram of the Population Mixing Technique

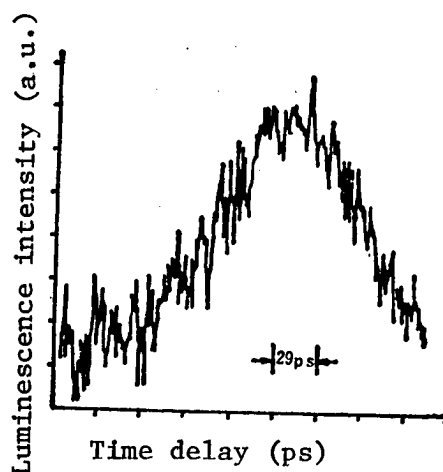


Figure 11. Measured Correlation Function for P-GaAs ($6.4 \times 10^{18} \text{Zn cm}^{-3}$) at 115 K and 840 nm

The basic experimental apparatus for frequency up-conversion is illustrated in Figure 12. To measure a transient spectrum, the laser pulse is divided into two beams: one is the excitation sample which produces the transient luminescence; the other beam is reflected back by the cube corner reflector and introduces time delay τ . The two beams operate coaxially in nonlinear crystals to produce a frequency which is a sum frequency the light of $\omega_3 = \omega_1 + \omega_2$ which when expressed as a wavelength can be written

$$\frac{1}{\lambda_3} = \frac{1}{\lambda_1} + \frac{1}{\lambda_2} , \quad (4)$$

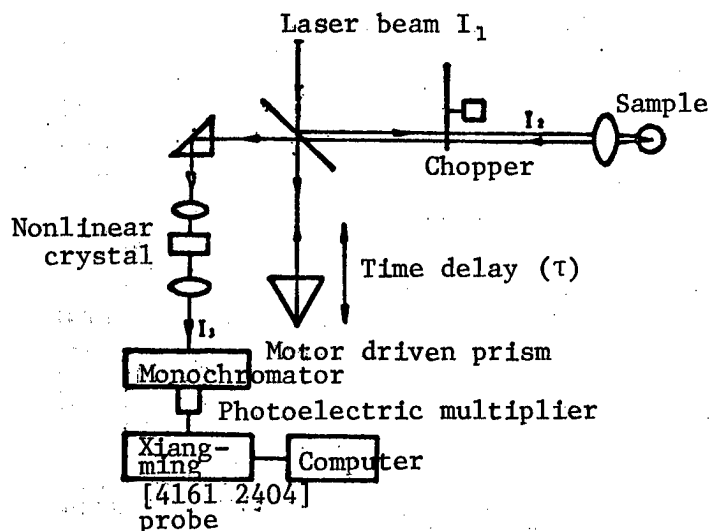


Figure 12. Schematic of the Up-Conversion Gate Technique

in which λ_1 is the laser wavelength; λ_2 is the wavelength of the luminescence measured; λ_3 is the wavelength actually measured and we can artificially set up a monochromator wavelength (λ_3) to achieve the aim of measuring different λ_2 . Clearly this can be used to obtain a group of spectrum curves of different delay times. On the other hand, if a monochromator is not used in the above apparatus to split the light but to measure the overall intensity of the luminescence, the process of changes in light intensity can be obtained for different time delays (luminescence decay process).

Daly and Mahr used this technique to measure the time-resolved spectrum of CdSe⁷ using a synchronous dye laser (10 ps) with excitation intensity of $\sim 5 \times 10^{-3}$ cm⁻³. Figure 13 is a graph of the time-resolved spectrum. When $\tau = 20$ ps the experiment observed that the central wavelength was 6280 Å wide luminescence peak, and as the delay time increased the luminescence peak became narrower and shifted towards the wavelength. After 90 ps, the position of the peak width and the peak value were basically unchanged, because in the process of cooling the plasma, the electron-hole formed liquid drops. Through this kind of time-resolved spectrum we could also obtain important information on the thermoelectron relaxation process. For example, we could obtain transient electron temperatures directly on the basis of the changes in intensity of the spectrum's high energy terminal and thus obtain the time evolution process of thermoelectron distribution.

3. Excitation-Probe Technique

Under a great many conditions, transient relaxation process is not accompanied by light emission (or there are difficulties in measuring light emission) and often accompanying the changes in some optical properties of the sample, such as changes in reflectivity and transmissivity, under these circumstances the excitation-probe technique is often used for measurements. In the excitation-

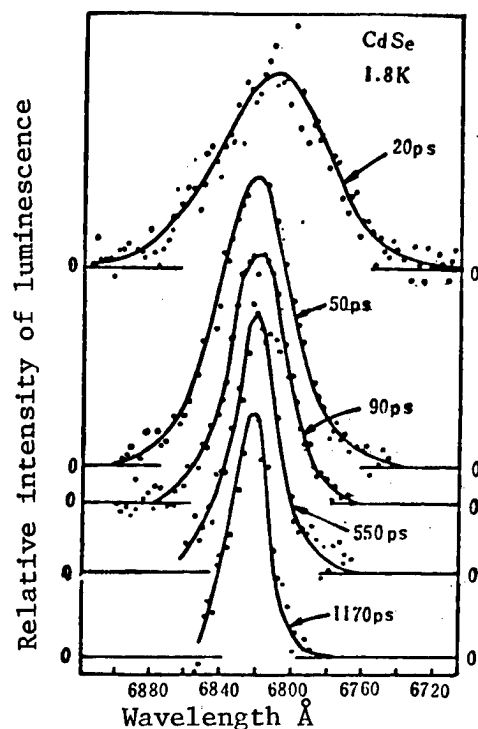


Figure 13. Luminescent Intensity Spectra From CdSe at 1.8 K for Fixed Time Delays After the Excitation

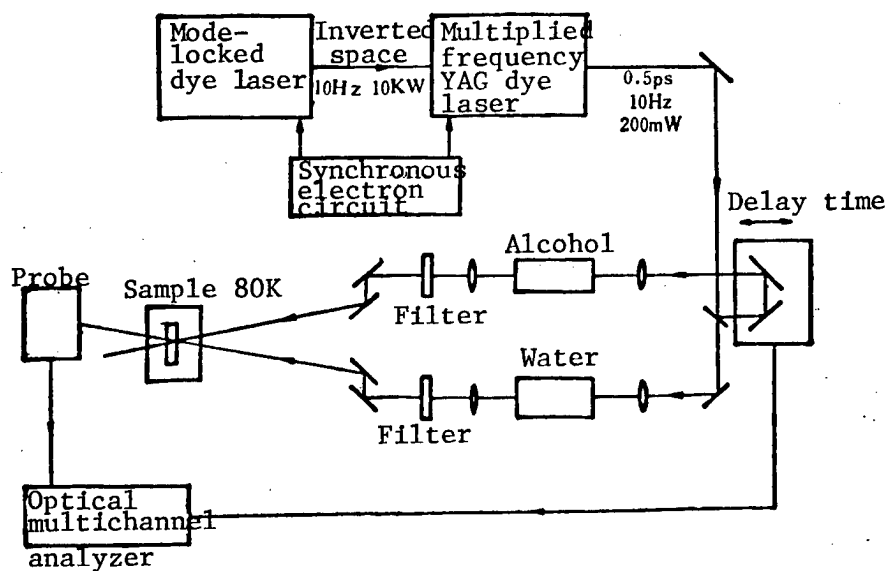


Figure 14. Experimental Arrangement of the Time Resolved Nearband Gap Absorption Spectroscopy

probe technique the first beam pulse puts the sample being studied into the excitation state, then the second pulse (time delay τ) probes the time succession process of the excitation state.

C.V. Shank, et al., used the excitation-probe technique to measure the process of absorption dynamics of the light excitation carrier in GaAs,⁸ and observed that the time constant of thermoelectron relaxation to the crystal lattice temperature was 4 ps, the exciton shield and band gap renormalization occurred within 0.5 ps. The experimental apparatus is illustrated in Figure 14. The light pulse produced by the mode locked dye laser goes through amplification, the synchronous alcohol pool and water pool, the former producing jilaman [3423 0812 2581 Gilman?] scattering producing a pulse light excitation sample of 7500Å, and the latter producing a white light pulse through interaction of the parameter's four photons to serve as a probe light with a sample of double heterojunction structure. From the results of analytical experiments we know that before excitation there is a definite exciton absorption line; when $\tau = 1$ ps the exciton peak disappears. This is because the great number of excitation carries creates an exciton shield; we observed that the absorption boundary shifted to undisturbed free excitons, this was caused by the carrier exchange interaction energy band compression; when $\tau = 12$ ps, energy greater than the transmission of exciton energy increases, this is caused by the energy band filling effect (see Figure 15).

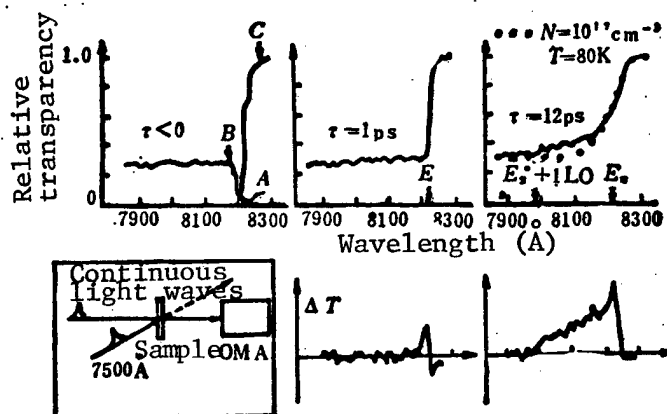


Figure 15. Time-Resolved Transmission Spectra and Difference Spectra of GaAs Near the Exciton Resonance

D. Von der Lindle, et al., used the excitation-probe technique to study the time-resolved phonon spectrum in GaAs and InP materials (77K),⁹ but the excitation light pulse and probe light pulse used came from the same light source (synchronous pump dye laser) and the excitation and the probe wavelengths were the same. The experimental apparatus is illustrated in Figure 16.

GaAs and InP belong to the T_d point group crystals. The polarization direction of the LO phonon scattering light which is scattered from (100) faces is perpendicular to the polarization direction of incidence light, therefore using a suitable polarization plate the scattering introduced by the

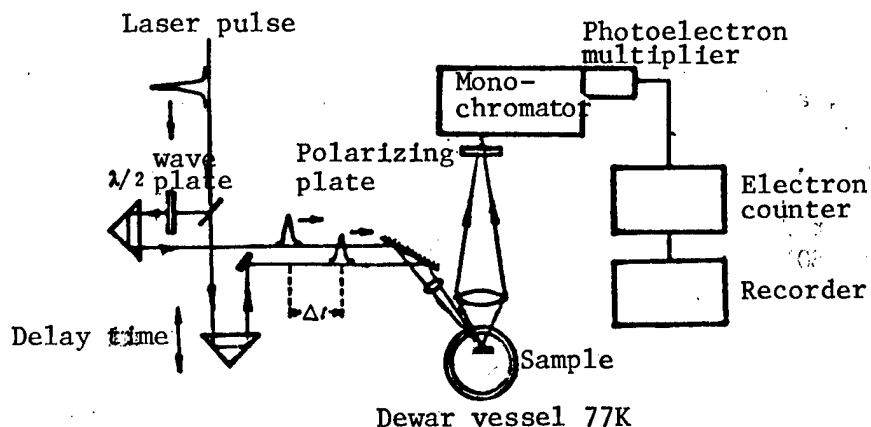


Figure 16. Schematic of Time-Resolved Phonon Spectroscopy

excitation light can be filtered out. The excitation light is only an excitation sample. It produces LO phonons and the probe light at the same time functions as excitation and probe, but the LO scattering light introduced by the probe light is unrelated to Δt , but is only structural background and the changes in LO phonons introduced by excitation light creates temporal changes in the scattering light intensity, thus information about LO phonon relaxation is obtained. In the experiment we obtained quasi-equilibrium LO phonon relaxation times in GaAs and InP of 7 ± 1 and 5 ± 1 ps, respectively.

IV. Conclusion

The application of ultrafast pulse lasers in semiconductors and other research areas is very lively, for example picosecond optical waveguide switches,¹⁰ physics research on amorphous materials,¹¹ research on semiconductor surface and boundary transient state processes,¹² etc. While introducing the dynamic state of research in this area, the key emphasis in this paper is on the experimental techniques and research content which the author has touched upon in past work.

REFERENCES

1. Shan, J., SOLID STATE ELECT., 21 (1978) 43.
2. Erskine, D.J., Taylor, A.J., and Tang, C.L., APPL. PHYS. LETT., 45 (1984) 45.
3. Fork, R.L., et al., APPL. PHYS. LETT., 38 (1981), 671.
4. Xu ZhongYing and Tang, C.L., APPL. PHYS. LETT., 44 (1984), 692.
5. Rosen, D., et al., APPL. PHYS. LETT., 39 (1981), 935.

6. Xu Zhong Ying, Kreismanis, V.G., and Tang, C.L., APPL. PHYS. LETT., 43 (1983), 415.
7. Daly, T., and Mahr, H., SOLID STATE COMM., 25 (1978), 323.
8. Shank C.V., et al., PHYS. REV. LETT., 42 (1979), 112.
9. D. Von der Lindle, et al., PROC. 15TH INT. CONF. PHYS. OF SEMICONDUCTORS, KYOTO (1980), 653.
10. Auston, D.H., et al., APPL. PHYS. LETT., 26 (1975), 101.
11. Vardeny, Z., et al., J. DE PHYSIQUE, C7 (1981), 477.
12. Hoffman, C.A., et al., APPL. PHYS. LETT., 33 (1978), 536.

8226/9365

CSO: 4008/48

ULTRAFAST IMAGE-CONVERTER CAMERAS: POWERFUL TOOLS FOR TRANSIENT RECORDING OF OPTICAL PHENOMENA

Beijing WULI [PHYSICS] in Chinese Vol 14 No 3, Mar 86 pp 168-172, 164

[Article by Zhou Xuan [0719 2467], Institute of Semiconductors, Chinese Academy of Sciences: "A Powerful Tool for Capturing Transient Optical Phenomena; Ultrafast Image-Converter Cameras"]

[Text] For some time many people have been familiar with the theory, performance and operation of ordinary camera, but still may be rather unfamiliar with ultrafast photographic technology. As the term suggests, ultrafast photographic technology is primarily for studying ultrafast moving targets or transient optical phenomena and complex (photographic) problems of elapsing processes. As photographic system, "ultrafast" refers to two aspects: one means that there is a very high shooting frequency (described as the number of images that are shot within a unit of time); the other meaning is the time resolution ability, i.e., how fast a transient process the camera can capture (for a shutter camera, described as the shortest exposure time). When higher shooting frequencies are required, it actually also demands higher time resolution.

For ordinary cameras with mechanical shutters, the shortest exposure time is several thousandths of a second, and this is sufficient time resolution for shooting most moving targets in daily life. But the many optical phenomena and elapsed processes involved in scientific research are much shorter, so that using an ordinary camera to shoot such high-speed phenomena is completely impossible. In addition to demanding extremely short exposure times, another difficulty encountered by high-speed photography is the problem of the light intensity of the target object. The essence of the photographic process is to cause the recording photographic plate to receive a certain exposure to light. When the exposure time is extremely short (which is necessary in shooting high-speed phenomena), to obtain a certain light exposure requires extremely high intensity of illumination. To adapt to the development of modern science and technology various kinds of high-speed photographic equipment has appeared, such as focusing cameras, Kerr cell (or Pockel's cell) camera and holocameras which use laser light sources. These cameras are all applied to different degrees. However, until the appearance of high-speed cameras using modern imaging tubes which have microchannel plates as information conversion components, no one camera (such as the image-converter camera) could resolve sufficiently the contradiction between high-speed response and high sensitivity.

Here we describe two ultrafast image-converter cameras--a one-time shutter type and a scanning streak camera--which are the main trends in current ultrafast camera development. The time resolution of the scanning streak camera in particular is smaller than 1 ps, and it is almost the only instrument that can be used for studying high-speed phenomena within the picosecond range. It can be anticipated that high-speed image-converter cameras will be more widely used in scientific research as a new optical measurement instrument the more they develop.

I. Basic Problems of High-Speed Photography Capturing One-Time Optical Phenomena

We will explain some of the basic problems which must be resolved in high-speed photographic technology using photoelectric study of gas electric discharge as an example.

Using a spark gap to study the gas electric discharge process is one of the basic methods of understanding the characteristics of gas breakdown under high pressure. Gas electric discharge has the following characteristics:

(1) Gas breakdown is determined by many factors such as the voltage between spark gap electrodes, degree of gas purity [4418 0553] and thus it is difficult to determine accurately the time at which breakdown will occur before the fact. The gas breakdown process can be divided into three stages. In the initial stage, even though a DC voltage is applied to the spark gap electrodes, there is still a delay before it produces the initial electrons which are used for avalanche multiplication. When the avalanche multiplication begins, the avalanche current rapidly rises to its critical value. Then the gas in the spark gap is completely broken down and forms a conduction channel. There is no doubt that if we can record the entire breakdown elapse process we can obtain a great deal of useful information from it. But, before gas electric discharge reaches its critical point, it is only accompanied by production of a very weak light radiation, and thus shooting the gas pre-discharge process required a camera with extremely high sensitivity.

(2) The duration of the gas discharge process is very short, especially in a compressed gas with a very high dielectric constant (such as SF_6) the duration has already entered the range of nanoseconds. Thus, to capture this transient process, a camera must have a correspondingly short possible exposure time. Gas breakdown is actually a single phenomenon and the time when the breakdown occurs is also hard to predict in advance. Thus to record such a process, the camera's shutter must be activated by the measured event itself. For this reason, there must be a delay time from the time the event occurs until the camera shutter opens. And this time must be as short as possible so that it can record the initial process of the measured phenomenon. Of course, by lengthening the optical path between the measured phenomenon and the camera lens the influence of the above mentioned delay time can be augmented (in air, 1 ns corresponds to 30 cm of optical path). However, technologically this is not always feasible, because it makes the already weak light radiation even weaker. The best method of solution is for the camera itself to have the ability to intensify the light.

(3) Along with the light radiation of gas discharge there may be a very broad optical spectrum range. Thus, the camera also should have a corresponding light spectrum response range, and it is best if it can convert incoming light of a very broad range directly into the visible light spectrum suited to observation by the human eye or recording ordinary film.

(4) The aim of photography is to reproduce accurately the measured target. To study the spark gap discharge channel in detail, the camera also should have a high enough spatial resolution and small enough distortion.

On the basis of the above characteristics, the camera system for researching the gas discharge process can be reduced to the following basic demands:

1) have a very high time resolution; 2) have a very high, adjustable optical gain; 3) can be triggered by the measured event itself and have the smallest possible trigger delay and wobble; 4) have a broad optical spectrum response range; 5) have a high spatial resolution; 6) have abundant information processing functions; and 7) have a structure which is compact, small and light.

The above basic demands are important issues which high-speed photographic technology has been trying to resolve for a long time. The image-converter camera can take into account the above basic demands and has already become a powerful tool for capturing, recording, and analyzing transient optical phenomena, and is playing a very important role in research on high-speed phenomena.

II. Comparison of Several Common High-Speed Optical Shutters

Light shutters (optical shutters) are the central part of any type of shutter camera. The shortest transient optical time provided by mechanical shutters is generally about 50 ns.¹ The Kerr cell and Pockel's cell were the earliest electrooptical components to use an optical shutter, but they both have the shortcomings of narrow optical response range, high opening voltage, and considerable loss in transmitting light energy. The appearance of the new image-converter based on the principles of electronoptics added new driving force to the development of high-speed photographic technology.

The types and structure of image-converters are very varied. However, all types of image-converters encompass one basic principle: First of all, an electron analog of the target image to be measured is formed with the help of a photocathode, then the photoelectrons released by the photocathode are controlled so that they are accelerated by the action of a strong electron field. Finally, these high-energy electrons collide with a fluorescent screen (anode) exciting the fluorescence and forming a secondary optical image. This image can be observed by the human eye or recorded using conventional photographic technology.

Since it is relatively easy to control and amplify the electron beam, the image converter can be used to approximate a high-speed inertia-less optical shutter. Image-converter types are differentiated mainly by the different method adopted for controlling the electron beam. One worth mentioning is

a recently developed method called the close-frame focusing method, which in essence makes the distance between the photocathode and the optical screen electrode surface extremely close (only several mm) so that there is formed in the vicinity of the photocathode an electron cloud which can be accelerated by a strong electrical field and travel directly toward the optical screen electrode along the electrical field gradient and does not cause obvious dispersion. This image-converter, which contains only a photocathode and an optical screen electrode, is called a diode image-converter. When it is used as an optical shutter, a 5-10 kV pulse voltage is applied between the two electrodes. If a third electrode (control grid) is added in this image-converter, then it forms a triode image-converter. The control grid requires only several dozen volts to be able to control the electron beam effectively. In the past dozen years a new close-frame focus image-converter which has a microchannel board has also appeared. Since it has an extremely fast reaction time, a very high optical gain and flexible control ability it has been applied extensively in high-speed photography technology. See Table 1 for a comparison of the typical performance of the different electrooptical high-speed optical shutters.

Table 1. Comparison of Typical Performance of Different Optical Shutters

Item	Optical gain	Response time	Control voltage	Mode of application
Kerr cell	0.1	100 ps	15-30 kV	single frame
Pockel cell	0.5	100 ps	1-5 kV	single frame
Diode image-converter tube	10	<1 ns	5-10 kV	single frame
Triode image-converter tube	100	<1 ns	200 V	multiframe or streak recording
Close-focus image-converter with MCP	10^4 - 10^5	<1 ns	200 V	single frame

III. The Simplest Diode Image-Converter

The basic structure of the diode image-converter is illustrated in Figure 1. The incident light shines on the photocathode P and through it releases photoelectrons which form an electron cloud in the vicinity of the photocathode surface. If a DC high voltage is applied between the photocathode P and the anode A, then the photoelectrons will be accelerated by the strong electron field and through the appropriate electron optical system O also be focused on the optical screen electrode (anode) A, and thus release electrons a second time, with the result being that an optical image is formed on the optical screen electrode. From the above-described optical-electron and electron-optical conversions, the incident optical image is enhanced. This image-converter which has image-enhancing capability is called an image enhancer.

It should be pointed out that there is no added electron optical system O for the close-frame focus image-converter with an extremely close distance between the photocathode and the anode. It is only because the distance between the photocathode and the anode is extremely close (several millimeters), when a voltage of several kV is applied between the electrodes, the field intensification is extremely high. Thus the photoelectrons released by the photocathode will move in a uniform electron field which is similar to a parallel plate capacitor, and the accelerated electron field reaches the optical screen electrode almost parallel and thus the electron beam is focused.

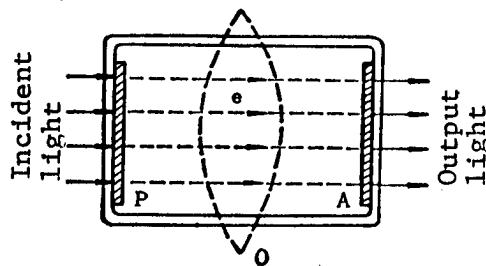


Figure 1. Diode Image-Converter

The principles of one-time high-speed photography using the close-frame focus diode image-converter as an optical shutter are illustrated in Figure 2.

The light emitted by the measured object G is focused through the objective lens O on the surface of the photocathode P . On the other hand, the optical signal synchronous with the measured optical phenomenon is changed through photoelectric conversion into an electron trigger signal which initiates the high-voltage narrow-pulse exciter. The high-voltage narrow-pulse output by the exciter is applied between the photocathode and optical screen electrode of the image-converter. Within the pulse width action time (i.e., the exposure time) the photoelectrons emitted by P are accelerated by the strong electron field and then new electrons are excited by collision with the optical screen electrode forming a new visible image. Through lens O_2 , the optical image formed on the optical screen electrode is recorded as an image on film F .

Each incident high-energy electron which collides with the optical screen electrode surface can produce many photons (typical value is 100-200) and thus the image-converter itself is a component with a very high optical gain. However, this light amplification which comes from electron excitation is almost completely canceled out by the two following factors. First, the typical quantum efficiency of the photocathode is only about 20 percent; second, the photon produced by collision of high-energy electrons with the optical screen electrode scatters in all directions completely irregularly, thus the intensity distribution of the output light created is also dispersed. After taking these factors into consideration, the overall light gain of the photographic system illustrated in Figure 2 is close to 1, thus performance cannot be satisfactory, and it is especially not suited to weak light targets.

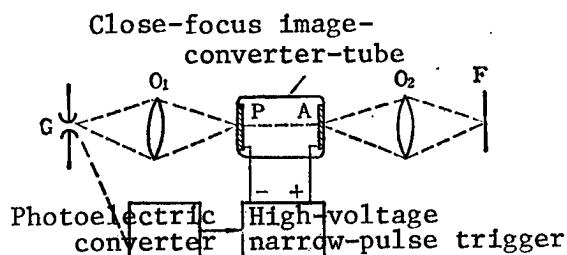


Figure 2. Principles of Single Event High-Speed Photography Using an Image-Converter as Optical Shutter

IV. New Image-Converter Tubes With Microchannel Plate and Optical Fiber Coupling Window

Two major technological advances which have been made in recent years have greatly improved the performance of the diode image-converter tube described above. The first advance benefited from achievements in optical fiber technology. Using an optical fiber window to replace the ordinary output rear window of the diode image-converter tube permitted transmitting the optical image produced on one plane to another plane almost without distortion. Since the optical image transmission efficiency was improved, the overall optical gain of the photographic system improved from nearly 1 to 15-30. The second advance in technology was the adoption of the so-called microchannel plate (MCP) structure.²

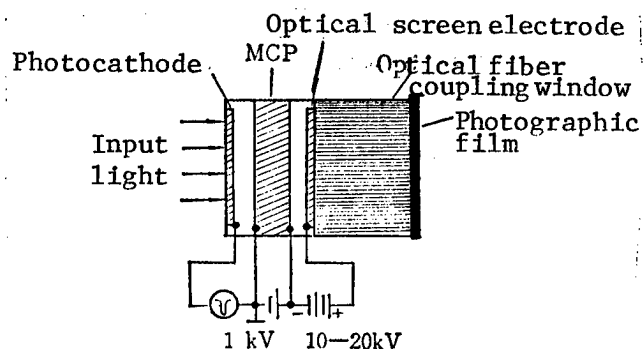


Figure 3. Shutter Tube With MCP and Optical Fiber Output Window

The structure of a new close focus shutter tube with an MCP and optical fiber output window is illustrated in Figure 3. The distance between the photocathode and the MCP input plane and between the optical screen electrode and the MCP output plane are several millimeters (i.e., close frame focus). The photocathode potential should be lower than the MCP input terminal potential, the photoelectrons which come from the photocathode and carry the image information project onto the input terminal surface of the MCP, and enter the microchannel. An acceleration voltage typically about 1 kV is applied between the MCP's input and output terminal surfaces. After the electrons entering the microchannel have been multiplied they appear again at the MCP's output

terminal. The electrons output from the MCP are again accelerated by a high voltage of 10-20 kV and cross a gap of several millimeters to reach the optical screen electrode where they excite fluorescence. The fluorescent image is transmitted to the photographic film by optical fibers. The photographic system thus constructed obtains an overall optical gain of several hundred thousand-fold between the photocathode and the photographic film! It must be pointed out that when this type of image-converter tube is used as an optical shutter, what is applied between the photocathode and the MCP input terminal is a pulse voltage, and the exposure time is determined by the gating pulse width, ordinarily in the range of nanoseconds. Thus, this new image-converter with MCP and optical fiber coupling window is especially suited to testing high-speed weak optical targets.

V. Streak Image-Converter Tube With Microchannel Plate

The streak image-converter is a component constructed with a streak camera at its center. Figure 4 shows the simplest scanning streak camera system.³ The main difference between the streak image-converter and the shutter tube illustrated in Figure 3 is that to the former are added a pair of scanning deflecting plates and the necessary additional electrodes. Simply described, the operating principle of the streak camera are as follows: the light to be measured (such as a group of laser pulses) is divided into two paths by a light beam-splitting device. One path forms an image on the photocathode through a narrow (typically 10 μm) and auxiliary optical system and the photoelectrons produced by this excitation enter the deflecting plates through focusing and acceleration. At the same time, the other path light signal is optically converted to an electrical contact signal which initiates the operation of a high-voltage slope wave (scan voltage) generator. A pair of push-pull high-voltage slope wave pulses which accelerate rapidly output by this generator are applied to the electrodes of the two deflecting plates, thus the photoelectric beam entering the deflecting plates is developed in time in a direction perpendicular to the deflecting plate plane. Then, the photoelectron beam developed enters the MCP and after considerable amplification reaches the optical screen electrode and excites fluorescence. Then an intensified optical image is obtained on the optical screen electrode. Since the input optical signal is a group of light pulses, what is obtained on the optical screen electrode will be a streak of varying brightness and changes in this streak reflect the changes in the light intensity with time. Waveforms of the measured optical pulse can be obtained by conversion through a microdensimeter.

The time resolution of the streak camera is not only determined by the physical design of the image-converter itself, but also is related to the external scanning path. The current time resolution is smaller than 1 ps, and it is reported that it can reach 10 fs.⁴

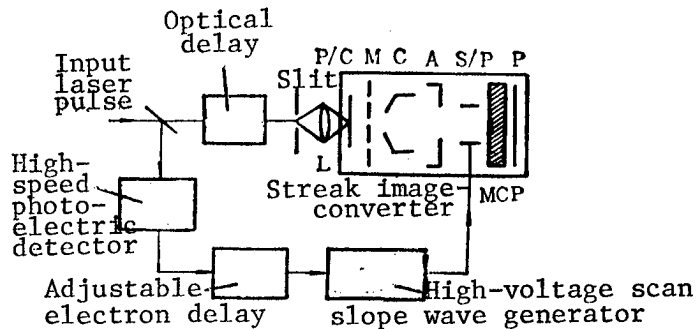


Figure 4. Simple Scanning Streak Camera System

L is lens; P/C is photocathode; M is aperture plate; C is focusing electrode; A is anode; S/P is deflecting plate; MCP is micro-channel plate; P is optical screen electrode

VI. Image-Converter Tube Pulse Control

The shutter-type image-converter tube and the gating pulse generator are combined to form the simplest shutter-type image-converter camera with high optical gain and rapid response. Similarly, the scanning streak image-converter tube and the scan generator which controls the photoelectron beam deflection are combined. There is no doubt whatsoever that the performance of these two image-converter cameras is primarily determined by the image-converter used itself, but here there is also the problem of how to use the image-converter performance effectively. In particular, the two important performance norms of the shutter-type image-converter camera--optical gain and exposure time--are directly determined by the gating pulse amplitude and width; and the most important performance norms of the scanning streak camera--streak speed--is directly determined by the scan voltage pulse amplitude and ascent time. In sum, at bottom the two are summed up in the demands of high voltage-high-speed pulse, and after deciding to use the image-converter, image-converter pulse control becomes one of the key technical questions in image-converter research and development.

The basic demands for an image-converter controlled pulse generator can be summarized as follows: 1) have a very high output pulse amplitude and the polarity demanded; 2) have the pulse shape demanded (for shutter-type cameras it must be a slope wave of excellent linearity) and narrow pulse width (or rapid ascent); 3) the generator is triggerable (electronic or optical) and have the smallest possible trigger delay and trigger wobble; 4) have strong tolerance negative load ability; and 5) have small mass, light weight, and long-range reliable application.

For a fairly long time a thyatron or a spark gap was used as the control pulse source of the image-converter. The trigger delay and wobble involved with this are comparatively large. With the appearance of several new types of high-speed semiconductor components, the image-converter's control pulse source has gradually been replaced by a solid-state pulse source with excellent performance.⁵⁻⁶

VII. Basic Organization and Application of Ultrafast Image-Converter Cameras

As we said above, there are a variety of ultrafast photographic systems. The image-converter and the corresponding control pulse trigger are two indispensable basic constituent parts of a high-speed camera which uses an image-converter as the information conversion component. Figure 5 illustrates the basic block diagram of an ultrafast image-converter camera system. The design of the image information processing element in the system is very flexible and can be determined depending on the specific situation.

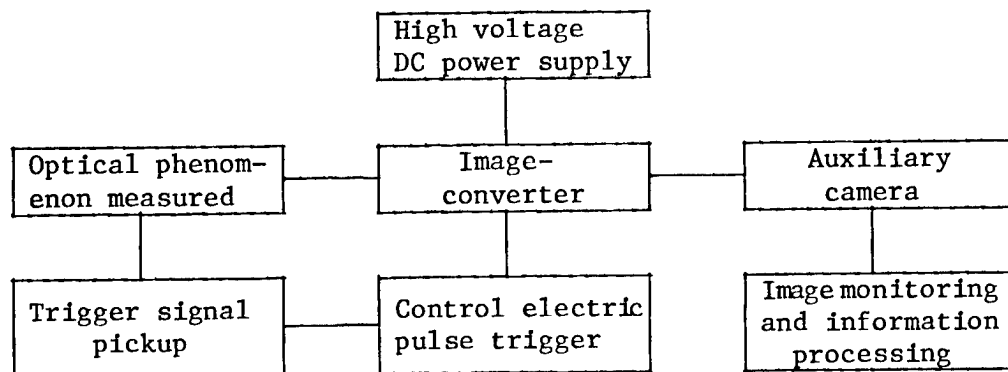


Figure 5. Composition of Ultrafast Image-Converter Camera

The high-speed camera introduced so far is called the "single frame" camera, i.e., corresponding to one trigger signal (synchronous with the measured optical phenomenon) there is produced a gating narrow pulse to be used by the shutter-type image-converter or a high-voltage fast slope pulse to be used for a streak image-converter scan, causing the high-speed camera within the corresponding time to photograph an image of the target and obtain one photographic frame. Although the exposure time (or scan time) is very short, the time interval between the two neighboring exposures (or two scans) is very long, thus in reality it can be accepted that the camera was operated only once. In practical applications, sometimes it is necessary to carry out continuous photographing of the measured target, i.e., one hopes to obtain many photographic frames. At such times it is necessary to add additional control electrodes and corresponding control circuits to the foundation of the image-converter described above. For example, for a shutter type image-converter, after each exposure, a step voltage deflecting electron ray can go to another position on the fluorescent screen to make the next exposure. In this way, each exposure not only is staggered in time but in space is also located in a different place on the fluorescent screen. After many exposures, a photograph of a certain size can be obtained. This multiple frame operation method has very important significance in actual applications. For example, the changes in attitude of a flight body (such as a guided missile) and the changes in spark gap discharge channels, etc., can be photographed. Of course, the more pictures a fluorescent screen of fixed dimensions is divided into, the smaller the images. Reference 9 also describes a new image dissection type special image division image-converter, which can record three frames in one

image, with a division cycle smaller than 100 ps. The picture division camera using this image-converter has been used in laser fusion research. To use scanning streak cameras to study highly repetitive high-speed optical phenomena (such as checking continuous mode-locked laser pulse sequence) high frequency sine wave voltage can be used to replace linear slope wave voltage as the streak image-converter's scan signal. This scanning mode is called "synchroscan."¹⁰ Present standard commercial scanning streak cameras (such as the IMACON 675) is already equipped with this type of synchronous scanning device.

Since ultrafast image-converter cameras with MCP have extremely high optical gain and extremely short time resolution they have become indispensable tools for high-speed phenomena research and their range of applications involves many important technical areas. In addition to the above described applications of ultrafast image-converter cameras in gas breakdown, laser fusion and ultrashort light pulse measurement, they have also been applied in such areas as measurement of laser produced plasma, research on molecular activated states, X-ray diagnosis, nonlinear optics, picosecond spectroscopy, fluorescent spectroscopy, synchronous accelerator radiation, explosions, optical communications and optical information processing and photobiology, photochemistry, and photophysics. Of course, to adapt to different application goals, it is necessary to adapt and expand the basic photographic system illustrated in Figure 5 and the image-converter type used should also be selected with a view to the research object, but as far as the basic problems involved with image-converter cameras is concerned, generally they are as described in this paper.

REFERENCES

1. Bacchi, H. and Eschard, G., PHILIPS TECHN. RDSCH., 30 (1969/70), 248-258.
2. Pan Guangdan [3382 1639 3225], WULI [ACTA PHYSICA], 13 (1984) 26-32, 81-85.
3. Kinoshita, K. and Suzuki, Y., Proc. 13th Int. Congr. High-Speed Photography and Photonics, Tokyo, Japan, (1978), 504-507.
4. Zavoisky, E.K. and Fanchenko, S.D., APPL. OPT., 4 (1965), 1155-1167.
5. Lundy, A., et al., IEEE. TRAN. NUCL. SCI., NS-25 (1), (1978), 591-597.
6. Zhou Xuan [0719 2467], DIANZI KEXUE XUEKAN [ELECTRONICS SCIENCE JOURNAL], 6 (1984), 448-455.
7. Zhou Xuan, Li Jinlin [2621 6930 2651], and Bao Bingqian [7637 4426 0051], YIQI YIBIAO XUEBAO, 5 (1984), 360-365.
8. Knox, W. and Mourou, G., OPT. COMMUNICATION, 37 (1981), 203-206.
9. Kalibjian, R. and Coleman, L.W., Proc. 13th Int. Congr. High-Speed Photography and Photonics, Tokyo, Japan, (1978), 447-480.
10. Hadland, R., Helbrough, K., and Huston, A.E., Ibid., 443-446.

APPLIED SCIENCES

BEIJING ELECTRON-POSITRON COLLIDER PROJECT DETAILED

Hong Kong LIAOWANG OVERSEAS EDITION in Chinese No 14, 7 Apr 86 pp 4-5

[Article by Gu Mainan] [7357 6701 0589]]

[Text] The Beijing Electron-Positron Collider (BEPC) project which attracted a great deal of attention from the international scientific community has been under construction for over 2 years. Recently, this reporter traveled to the construction site and had an interview with the three gentlemen in charge of the project: Gu Yu, Xie Jialin, and Fang Shouxian.

In the project coordination room, group leader Gu Yu briefly summarized the current project status. For detailed questions, he referred the author to professors Xie Jialin and Fang Shouxian, who are experts in particle accelerators.

Pointing to a large BEPC schedule and progress chart on the wall, the two experts said: "Since October 1984, when director Deng Xiaoping personally endorsed the project, dozens of organizations and thousands of engineering and technical personnel had dedicated their efforts to the project; during this time, the prototypes of six key facilities used for the collider had been developed and certified; other equipment is also being developed. The near 1-km tunnel is partially finished. In short, the completion date of the entire project is nearly in sight. A large national laboratory which will attract physicists around the world to explore the secrets of the microscopic world will soon be erected on Chinese soil!

In the office of the front-line project director Fang Shouxian, the reporter noticed a lunch box on the desk and blankets on the sofa.

"Do you use your office as your living quarters?"

"To build such a high-technology facility is not only unprecedented in China but also a very challenging task internationally. Director Deng Xiaoping had requested that our accelerator must be completed on or ahead of schedule. Now that the completion date is in sight and this gold medal for the state is nearly at hand, the entire staff on this project are working around the clock.

Since project leaders must be present right at the front line, all our coordination meetings are now being held after normal hours!" said Prof. Fang with a smile.

To build this collider has been the dream of Chinese scientists for the past few decades. In the last 1940's, Xie Jialin crossed the Pacific to study engineering in the United States. As he was ready to return to China after receiving a doctor's degree from Stanford University, the Korean war broke out. When his ship reached Hawaii, he and seven other passengers were detained by officials of the U.S. Immigration Service, who said: "According to U.S. law, students whose fields of study are related to military applications are prohibited from leaving the country." Anxious to return home, Xie Jialin immediately called the President of the United States to protest, but to no avail. Consequently, he had to go back to the U.S. mainland and later became the director of a project to build an accelerator for one of the medical centers in Chicago. In the summer of 1956, he received a notice from the U.S. Government giving him two options: one was to leave the country before a certain deadline, the other was to remain in the U.S. and become a permanent resident. Xie Jialin chose the first option; his reasoning: "I am a Chinese, and therefore I have a responsibility to help China in its national construction." So it was that he returned to this country.

In the early days of the People's Republic, everything was waiting to be developed, and all the key components required to build an accelerator were sanctioned by other countries. Under this very difficult condition, Xie Jialin recruited eight recent college graduates, and after much hardship and struggle, they succeeded in building China's first electron linear accelerator.

When China decided to build this collider, some skeptics questioned whether China was able to tackle this job with its underdeveloped science and technology and rather weak industrial base. Xie's reply was: "We have been through a lot of hard times before and overcome all kinds of difficulties. Today, all the conditions are much improved compared with the early days; besides, we have the full support of the Party Central Committee and the cooperation of other industries and organizations, what is there to worry about?" Thus, under his confident leadership, the project took off.

"During the preliminary design stage, the BEPC project received enthusiastic support from major accelerator centers of the United States, the European Nuclear Research Center and from West German scientists. During the initial planning phase, Zhu Hongyuan and I made a special trip to the United States to consult with our American colleagues. Prof. Li Zhengdao invited all the leading accelerator experts in the U.S. for a meeting at the Fermi Laboratory where they participated in discussions and contributed their ideas. Experts at the Stanford Linear Accelerator Center contributed a great deal of their time to outline a preliminary design plan as a reference for our project." said Prof. Xie.

"What is an electron-positron collider? What is it used for?" These are probably the questions that most readers would like to know the answers to.

Prof. Xie and Prof. Fang gave the following explanation: "A collider is a large research apparatus which consists of thousands of precision parts connected together in series. When the power is turned on, each component must perform in exactly the prescribed manner. Two beams of electrons and positrons each 0.1 mm thick, 1 mm wide, and 10 cm long revolve in the accelerator along a 240-m acceleration tube. At every revolution a collision occurs, and there are more than 1 million collisions per second. In order to achieve collision, the collider design must meet very stringent requirements.

This collider is expected to be ready for beam generation by the end of next year, and the first electron-positron collisions are expected to take place in 1988. The collider consists of the following components: the injector, the storage ring, the detector, the synchronous radiation test region, and the computing center. The basic objectives for building the collider were: 1) to promote the research of high-energy physics in China, and 2) to promote the application of synchronous radiation.

Sketching a schematic diagram on a piece of paper, Xie Jialin proceeded to explain the extreme importance of basic research. The discovery of television, radar, X-ray's, the atomic bomb and atomic energy all hinged on a good understanding of the structure of atoms and nuclei. The appearance of these things unquestionably had profound effect on human lives. The particles that make up the microscopic structure of matter are so small that they are not visible to human eyes or microscopes. Therefore, scientists invented different types of accelerators to study these "fundamental particles"--the smallest units of matter. The collider is a new type of accelerator which was developed in the 1970's. Everytime a breakthrough occurs in these studies, human knowledge about nature takes a giant step forward. In the early 1970's, the well-known Chinese-American physicist Ding Zhaozhong discovered the J particle using a proton cyclotron at the Brooke Haven Laboratory. At about the same time, American scientist (Lichter) also found this particle in a positron-electron collider at the Stanford Linear Accelerator Center. In the latter case, the signal was loud and clear, and the noise background was low. This illustrates the superiority of the electron collider.

The collider can also be used in the study of the application of synchronous radiation. Synchronous radiation is the light emitted by high-energy electrons traveling along a circular orbit in a synchronous cyclotron. This light source provides the basic tool for studying a variety of scientific topics such as surface physics, atomic-molecular physics, solid-state physics, material science, biochemistry, biophysics, genetic engineering, catalytic chemistry, environmental science, medicine, X-ray microscopy and photo-etching.

At this point, Prof. Xie showed us a silicon chip covered with crisscrossing integrated circuits and said: "The connections of today's integrated circuits are several microns wide; by using synchronous radiation, the width of the connections can be reduced to less than 1 micron, thus greatly increasing the

level of integration. Synchronous radiation can also be used in medicine. To detect the blockage of coronary arteries of elderly persons because of cholestral accumulation, one of the methods is to take two pictures of the heart with adjacent wavelengths using synchronous radiation, and process the information using computers. Thus, the patient runs no risk of surgery, and is exposed to very little radiation dosage. Therefore, it could very well become a widely used tool for treating arteriosclerosis.

Today there are more than 10 positron-electron colliders in the world. The United States is planning to spend 6 billion dollars over a 10-year period to build a 100-km super-conducting super collider (SSC). The European Nuclear Research Center is in the process of constructing a 27-km positron-electron collider. China's current economic resources do not allow expenditure of this magnitude. But while its energy level is rather moderate, our collider will have a unique place in the international community because the energy level of this collider (2.2 billion eV to 2.8 billion eV) allows the study of certain problems in physics that cannot be investigated with other types of accelerators. At present, our collider has the highest design brightness in the world in this energy region.

The director of the project office, Liu Huaizu explained that the project guidance group organized by the government is composed of members from the Chinese Academy of Sciences, the National Planning Commission, the National Economic Commission, and officials of Beijing City. This is a group with clearly defined responsibilities and high operating efficiency; it not only provides the day-to-day project guidance from the Chinese Academy of Sciences, but is also responsible for coordinating the activities of nearly 100 units from more than 10 ministries and committees around the country. Because of the good coordination effort, the project is progressing rapidly. He pointed out that of the nearly 10,000 parts and components of the collider, 70 percent are non-standard, special-purpose devices which must meet high precision requirements, and are technically very different to build. But the prototypes of most of these special-purpose devices had been developed in about a year, and they are already being mass-produced. The civil construction work is also moving at a rapid pace. The 200-m tunnel of the electron linear accelerator and the large hall containing the accelerator tube have already been completed. Such speed of construction is unprecedented in China and considered above average based on international standards. On this project, we not only took full advantage of the most advanced technologies available to us, but also saved considerable amount of money for the state.

After the interview, the reporter was given a tour of the construction site. Directors of Research Yan Taixuan and Luo Yingxiung pointed to a large curved magnet being tested and said: "Each of these magnets is made of 3,000 pieces of 0.5-mm thick silicon steel plates pressed together. The collider requires 40 of such magnets. Technicians at the Xian Feng Electric Motor Co. in Shanghai can produce 3 to 4 high-quality magnets per month, and they are working around the clock. In the past, we never attempted to make this type of magnet. In order to guide the electrons along a prescribed track, the collider also needs 60 focusing magnets. These magnets must satisfy even higher precision requirements, and each piece is pressed together with 1,00

silicon steel plates. They are being built by workers of the High Energy Institute, and are scheduled to be installed in the tunnel by the end of this year. In addition, 56 precision acceleration tubes which are 3-m long and made of oxygen-free copper, 16 high-power speed regulation tubes, modulators, and banks of linear accelerators are also needed. Therefore, this is truly a rare scientific and technological challenge for this country. To ensure that the project will be on schedule, thousands of technical personnel and workers have devoted their lives to the project; some scientists give up the opportunity to study abroad and spend their holidays working on the project.

Speaking of the enthusiasm exhibited on this project, Fang Shouxian said: "Many of us have worked abroad because we did not have our own accelerator and had to use other country's accelerators for research. Since returning home from the Dubna Joint Institute for Nuclear Research of the Soviet Union, I have participated in the design of several accelerators with my colleagues over the past 20 years, but all of them were abandoned because of lack of adequate preparation. Therefore, the colleagues of my generation are determined to make our dream come true, i.e., to successfully build an accelerator within our lifetime so as to boost the pride of the Chinese people and to reserve a place for China's high-energy physics on the international stage."

3012/13104
CSO: 4008/95

THE TIME PROJECTION CHAMBER: NEW CONCEPT IN PARTICLE DETECTION

Shanghai HE JISHU [NUCLEAR TECHNIQUES] in Chinese No 5, May 86 pp 19-23, 37

[Article by Chen Chaoqing [7115 2600 3237]]

[Text] I. Introduction

The time projection chamber (TPC)¹ is a new detection device that can simultaneously measure the three-dimensional position, momentum of charged particles and perform discrimination of particle types. It differs from a conventional cylindrical drift chamber in that inside a TPC, the electric field is parallel to the magnetic field, thus the force $E \times B$ has little effect on electron drift; the detection surfaces are located on the two end covers, and because there are no metallic wires along the axial direction of the cylinder, the sensitivity volume can be made very large, which can accommodate several hundred sample measurements of the energy loss (dE/dx), thus providing good discrimination capability. It has extremely good spatial and momentum resolution, dE/dx resolution, and facilitates pattern recognition; it is a relatively advanced high-energy detector which can be used in collision physics experiment or stationary target experiment. The same principle can also be used to build a simpler TPC which would have sufficiently good performance to be used as a powerful tool in the study of medium-energy physics, nuclear physics, and heavy ions.

The basic concept of TPC was proposed in 1974 by Dr D.R. Nygren³ of the Lawrence Berkeley Laboratory (LBL), and it was first developed and built at the LBL.³⁻⁵ Over the last 10 years, many laboratories around the world had designed and built various types of TPC's based on the requirements of the individual physics experiments.¹⁹⁻²⁵

Under the guidance of Dr Nygren, the author participated in part of the construction work and testing of the LBL-TPC. This article briefly describes the structure, operating principle, and performance test results of the LBL-TPC.

II. The Structure of LBL-TPC

Figure 1 shows a structural diagram of the time projection chamber. It is a special cylindrical drift chamber which is 2m long and has an inside diameter

of 40cm and an outside diameter of 2m. The cylinder is divided into two completely symmetric sections by a thin-film electrode. The thin-film electrode is a mesh electrode made of stainless steel wires; it offers low resistance to airflow and is transparent to particles. A high negative voltage is applied to the electrode; the maximum design value is -200 kV. The inside and outside walls of the cylinder are covered with copper-plated annular electrodes, called the electric field cage. A resistance voltage divider is used to form a uniform drift field.

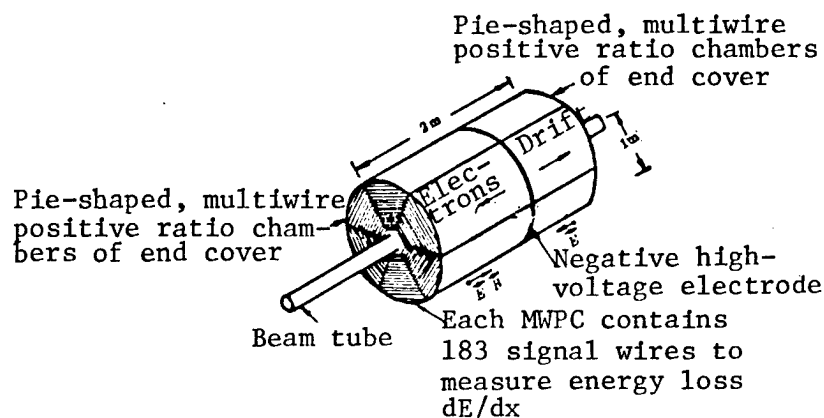


Figure 1. Structural Diagram of a Time Projection Chamber

The two end covers of the cylinder each has six pie-shaped multiwire positive-ratio chambers (MWPC). Each MWPC contains four planar electrodes: the cathode, the anode, the screen grid, and the gate grid, as shown in Figure 2. The distance between the anode and the cathode are both 4mm; the distance between the gate grid and the screen grid is 8mm. The grid mesh is made of 76 μm beryllium copper wire which is separated by 1 millimeter. The screen grid wires perform two functions: one is to separate the drift region from the amplification region; the other is a funnel-like function, which "focuses" the electric field lines onto the signal wires. Thus, the ionizing electrons produced by each of the 4mm-long particle tracks are drifted to the corresponding signal wire. The gate grid^{6,7} is used to prevent the feedback of positive ions and to reduce the effect of space charge. It performs the function of an electronic switch. Normally, this gate is always closed, which blocks the drift electrons; the gate is opened only when a favorable event occurs to let the drift electrons reach the anode mesh in order to induce an avalanche. To reach this goal, a common negative bias voltage \bar{V}_G is applied to all the gate grid wires, so that the drift field lines can freely pass through the gate grid, as shown in Figure 3a; to close the gate grid, two low voltages with opposite gate grid wires to prevent the electric field lines and hence the drift electrons from passing through the gate grid, as shown in Figure 3b. The opening and closing of the gate grid has 183 signal wires and an equal number of electric field wires. The signal wires are made of 20 μm gold-plated tungsten wires, and are used to measure the energy loss dE/dx . The distance between signal wires is 4 millimeters. The electric field wires are made of 76 μm beryllium-copper wires; they are placed between neighboring signal wires to reduce crosstalk. The cathode plane is made of 1 cm-thick plates with copper coatings on both sides. Fifteen rows of cathode pads are etched on

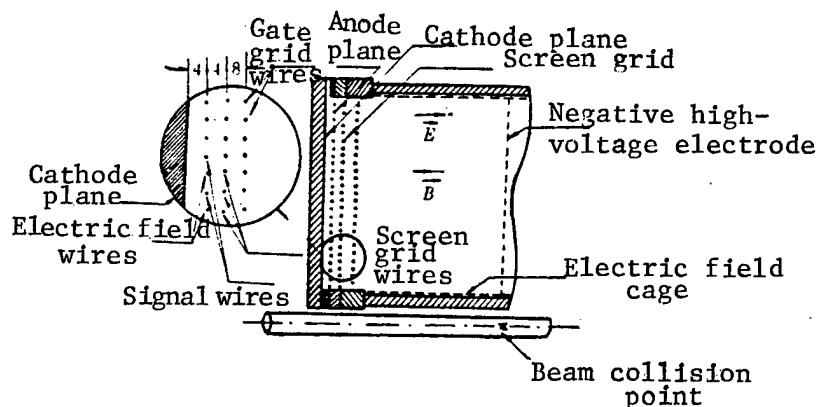


Figure 2. Arrangement of Electrodes in a TPC

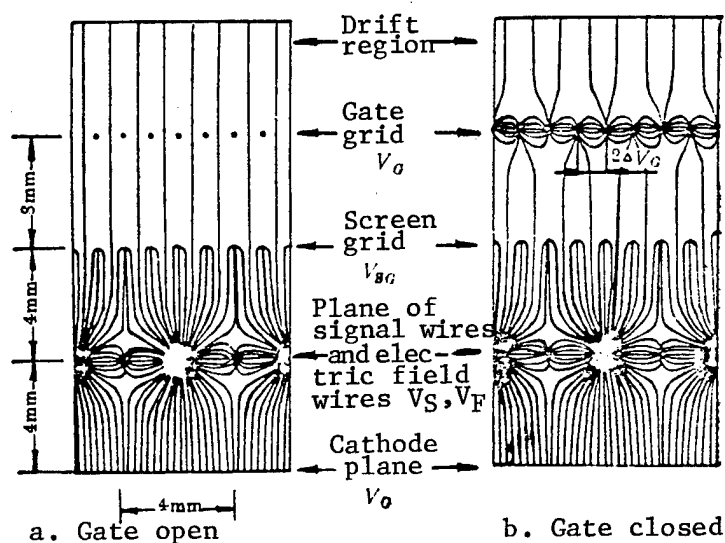


Figure 3. Switching States and Electric Field Distribution of the Gate Grid

the copper-coated plates, each pad has an area of 7.5mm x 7.5mm and the insulated gap is 0.5 millimeters. These 15 rows of pads are located directly below the corresponding 15 signal wires to measure the coordinates along the wires.

Each pie-shaped MWPC carries 1,335 low-noise preamplifiers which are installed on the back side of the cathode plate. In order to lower the temperature rise caused by preamplification, each MWPC is equipped with a water cooling system on the back side.

The entire TPC is housed inside a high-pressure container filled with a mixture of argon (80 percent) and methane (20 percent). The maximum design pressure is 10 atm. The high-pressure container is enclosed by a magnetic coil.

III. Operating Principle

When charged particles pass through the chamber, an ionized track is formed in the gas. Under the action of the electric field, the electrons are drifted toward the MWPC of the end cover. During the drift process, lateral dispersion of the electrons is constrained by the axial magnetic field which is parallel to the electric field; hence the electrons can drift over a long distance without significant dispersion. The amount of dispersion is determined by the magnetic field strength B and the gas pressure P :

$$\sigma_D(B) = \sigma_D(0) / \sqrt{1 + (\omega\tau)^2}$$

where $\sigma_D(B)$ and $\sigma_D(0)$ are, respectively, the RMS lateral dispersion distance with and without magnetic field, $\omega = eB/cm$ is the gyromagnetic ratio of the electrons, τ is the mean collision time of the electrons, which is inversely proportional to the gas pressure P . Clearly, when the magnetic field strength B is sufficiently large so that $\omega\tau \gg 1$, then lateral dispersion can be effectively compressed.

When the drift electrons reach the MWPC of the end covers, ionization avalanche occurs in the vicinity of the anode wire, thus generating a negative pulse signal. At the same time, a positive pulse signal is induced on the pad below the anode wire, as shown in Figure 4. Each avalanche on the signal wire will produce an induced signal above the threshold on 2 to 3 pads below the signal wire. The magnitude of the signal is proportional to the solid angle subtended by the pad relative to the position of avalanche. The barycenter of the induced signal determines the position of the avalanche on the signal wire.

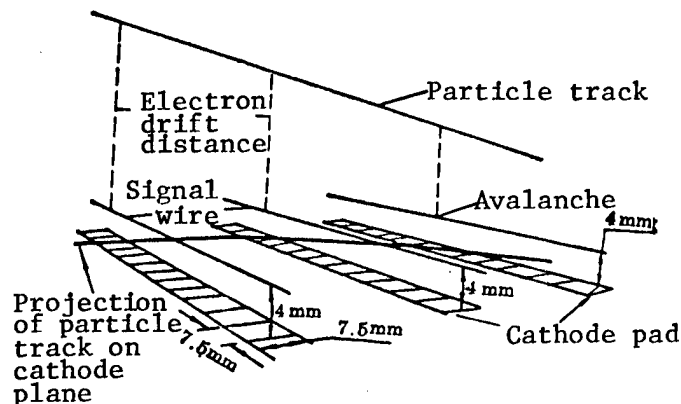


Figure 4. Measurement Technique for Determining Three-Dimensional Coordinates of Particle Tracks in a TPC

After amplification by the low-noise FET preamplifier, the negative pulse generated on the signal wire and the positive pulse generated on the pad are transmitted to the remote shaping amplifier⁸ where they are subject to further amplification and discrimination, and then stored into a charge couple device (CCD).⁹ CCD is an analog shift storage device that contains 455 charged

storage elements. Under the control of external timing pulses, the charge (pulse height) signal moves from one storage element to another. The frequency of the external timing pulse at write-in time is 10 MHz, hence the time for a signal to move from one element to another is 100 ns; a CCD can store an analog signal 45.5 μ s in duration. The maximum drift distance in a TPC is 1 m, the electron drift speed is 5cm/ μ s, hence the maximum drift time is 20 μ s. The delay time of a CCD is capable of storing all the analog signals within the drift time of the TPC. At read-out time, the frequency of the external timing pulse drops to 110 KHz to facilitate digital conversion of the analog signals. The converted data are stored in the buffer storage unit for computer processing.¹⁰⁻¹²

1. Coordinate Measurement

We define the X coordinate to be along the direction of the signal wire, the Y coordinate to be in the anode plane and perpendicular to the signal wire, and the Z coordinate to be along the axial direction of the chamber. The X and Y coordinates of the particle track are determined by the position of the barycenter of the signal on the cathode pad, and the predicted measurement accuracy (RMS deviation) is 150 μ m. The Z coordinate is determined by the drift time of the ionizing electrons from the particle track to the MWPC of the end cover; the predicted measurement accuracy is 350 μ m.

2. Momentum Measurement

Having determined the three-dimensional coordinates of the charged particle track, one derives its radius of curvature R on a plane perpendicular to the magnetic field, and determines the lateral momentum of the particles $P = 0.03 BR$ (where the unit of P is GeV/C, the unit of the magnetic field is T, and the unit of the radius of curvature is m). The range of momentum that can be measured by the LBL-TPC is from 100 MeV/C to 15 GeV/C. When the magnetic field strength is 1.5 T, the predicted momentum resolution is $\Delta P/P^2 = 0.4$ percent (GeV/C)⁻¹.

3. Particle Discrimination

The output pulse height from the signal wire indicates the magnitude of the energy loss dE/dx suffered by the particles in passing through the 4mm-high pressure gas. The energy loss dE/dx of a charge particle is related to its speed. Once the particle momentum is determined, the charge-to-mass ratio of the particle can be determined by measuring its energy loss dE/dx, hence the type of particle can be identified.

Figure 5 shows the relationship between the most probable energy loss and momentum for several different types of particles over a distance of 4mm in an 8.5-atm gas mixture of argon (80 percent) and methane (20 percent). It can be seen that as the momentum increases, the particle energy loss can be divided into three different regions,¹³ i.e., the nonrelativistic region ($\beta\gamma < 2$), the relativistic region ($2 \leq \beta\gamma < 100$), and the super relativistic region ($\beta\gamma \gg 100$). Here $\beta = v/c$, $\gamma = (1 - \beta^2)^{-1/2}$, v is the particle velocity, and c is the speed of light in vacuum. In the nonrelativistic region, dE/dx

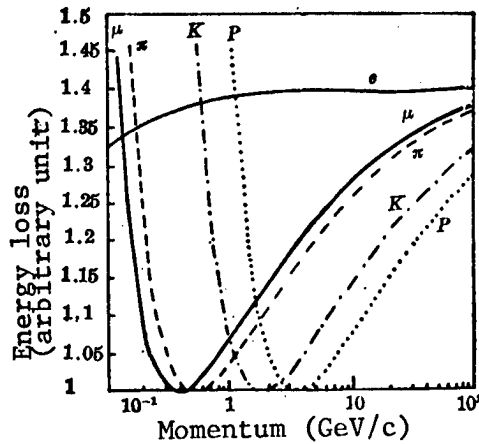


Figure 5. Relationship Between the Most Probable Energy Loss of Charged Particle and Its Momentum

Note: The gas mixture contains 80 percent argon and 20 percent methane, the pressure is 8.5 atm, and the sample thickness is 4mm

varies with β^{-2} , and particle discrimination is relatively easy. In the super relativistic region, dE/dx does not vary with momentum, hence one cannot use dE/dx for particle discrimination. In the relativistic region, dE/dx increases logarithmically with $\beta\gamma$. Figure 5 shows that in this region (where momentum varies from 1 GeV/c to several hundred GeV/c), the rise in energy loss is only around 40 percent. Although the energy losses for different types of particles at the same momentum value are not the same, the differences are quite small. Therefore, if the particles are to be distinguished by the relativistic rise in ionization energy loss, the detector must have extremely high dE/dx resolution.

But in a thin gas medium, there are considerable fluctuations in the particle energy loss, which is referred to as the "Landau tail." It is formed by the energy spectrum of the " δ electrons" produced by the particles passing through the medium. Therefore, the dE/dx resolution of a single sample is very poor. The key to improving dE/dx resolution is to perform multiple independent measurements of the energy loss of each particle. In general, if the number of samples is N , then the resolution can be improved by a factor of \sqrt{N} . Each pie-shaped MWPC on the end cover has 183 signal wires, hence as many as 183 dE/dx samples can be taken along each track. Furthermore, the high-pressure gas of a TPC ensures that each sample contains a sufficient number of ionizing electrons, and that the dE/dx resolution of a TPC can exceed the 3 percent requirement so that within the momentum range from 100 MeV/c to 15 GeV/c, it can discriminate such particles as π mesons, K mesons and protons as well as the low-momentum electrons and μ mesons.

IV. Performance Results

1. Spatial Resolution^{14,15}

The spatial resolution σ_{xy} on the XY plane depends on many factors. Based on the results of cosmic ray measurements, this relationship can be expressed in the following form:

$$\sigma_{xy}^2 = \sigma_A^2 + \sigma_B^2 \frac{L}{L_M} e^{\gamma L} \sec \alpha + \sigma_C^2 e^{\gamma L} \cos \alpha \tan^2 \alpha$$

where L is the drift distance (m); L_M is the maximum drift distance (1m); α is the subtended angle between the projected track on the MWPC and the Y axis; γ is the electron capture rate per meter. The first term σ_A represents the inherent spatial resolution of the chamber, which is determined by the electronic noise and other system effects. The second term is due to electron lateral dispersion, and the third term is due to ionization fluctuations.

Measurements are made in the chamber with a gas mixture of 80 percent argon and 20 percent methane under the following conditions: gas pressure--8.5 atm, drift electric field strength--75 kV/m, and magnetic field strength--0.4T; the results are $\sigma_A = (160 \pm 2) \mu\text{m}$, $\sigma_B = (105 \pm 6) \mu\text{m}$, $\sigma_C = (249 \pm 7) \mu\text{m}$. Therefore, when $L = 0$ and $\alpha = 0^\circ$, $\sigma_{xy} = 160 \mu\text{m}$, which is very close to the predicted value of 150 μm . If a superconducting magnet (1.5T) is used instead of the conventional magnet (0.4T), further improvement can be expected.

The measured resolution in the z direction σ_z is $(340 \pm 5) \mu\text{m}$, which is better than the predicted value of 350 μm . The resolution of the dual tracks is 1 cm.

2. Momentum Resolution

Under the above conditions, the momentum resolution based on cosmic ray measurements is:

$$dP/P^2 = (6.4 \pm 0.3) \text{ percent } (\text{GeV}/c)^{-1}$$

For a magnetic field strength of 0.4T, the predicted momentum resolution is 1.6 percent $(\text{GeV}/c)^{-1}$, which differs from the measured value by approximately a factor of 4. This is due to the imperfect design of the chamber which causes the particle tracks to be twisted in the vicinity of the inner and outer walls because of electric field distortion. Consequently, in the data analysis only the untwisted segment of the track can be used, which degrades the momentum resolution. Later, improvements have been made to the electric field cage, and a gate grid has been added to the MWPC on the end cover, thus eliminating the twisting effect and greatly improving the momentum resolution.

3. Resolution of dE/dx ^{16,17}

Measurements are made using cosmic rays. A particle track with 155-183 dE/dx samples is chosen, but in the data analysis, only 65 percent of the samples with the lowest pulse height are included in the averaging process. Under the

pressures of 8.5, 4.0, and 1.0 atm, the measured dE/dx resolution $\sigma_{dE/dx}$ are respectively 3.0 ± 0.1 percent, 4.2 ± 0.3 percent, and 6.5 ± 0.5 percent.

4. Measurement of Relativistic Rise

The relativistic rise of dE/dx is measured using the μ mesons of the cosmic rays. The relativistic rise is represented by the ratio between the 3.5 GeV/c κ - π separation and the minimum ionization. The energy loss of the π meson and κ meson with a momentum value of 3.5 GeV/c is equivalent to the energy loss of μ mesons with momentum values of 2.65 GeV/c and 0.75 GeV/c in the same gas medium:

$$\kappa\text{-}\pi \text{ separation} = \frac{[(dE/dx)(2.65\text{GeV/c}) - (dE/dx)(0.75\text{GeV/c})]}{[(dE/dx)(\text{minimum value})]}$$

The measured results are listed in the table below. If we want to achieve a 4-standard deviation κ - π separation, the dE/dx resolution must be better than 3.5 percent, and the systematic error must be smaller than 1 percent. Therefore, fluctuations in the signal wire gain with voltage, gas pressure, and temperature must be carefully controlled and corrected.¹⁸

Table

Gas pressure (atm)	3.5GeV/C	κ/π separation
	Percent	Standard deviation
8.5	14.6 ± 0.3	4.8 ± 0.25
4.0	16.6 ± 0.5	3.9 ± 0.5
1.0	18.4 ± 0.3	2.8 ± 0.3

REFERENCES

1. PEP Experiment No 4, SLAC report pub-5012 (1976).
2. Nygren, D.R., "Proposal To Investigate the Feasibility of a Novel Concept in Particle Detection," LBL internal report, February 1974.
3. Nygren, PEP, 144 (1974), in PEP summer study.
4. Ibid., 198 (1975).
5. Fancher, D., et al., NUCL. INST. METH., 161, 383 (1979).
6. Nygren, D.R., PHYSICA SCRIPTA, 23, 584 (1981).
7. Ishibashi, A., TPC-UT-83-1, March 1983.
8. Landis, D.A., et al., IEEE TRANS. NUCL. SCI., 29, 1, 573 (1982).
9. Jared, R.C., et al., Ibid., 29,1, 282 (1982).

10. Ibid., 29, 1, 57 (1982).
11. Loken, S.C., et al., Ibid., 30, 1, 162 (1983).
12. Ronan, M., et al., Ibid., 29, 1, 427 (1982).
13. Marx, J.N. and Nygren, D.R., PHYS. TODAY, 31, 10 (1978).
14. Barbaro-Galtieri, A., SIAC-250, 46 (1982).
15. Madaras, R.J., et al., IEEE TRANS. NUCL. SCI., 30, 1, 76 (1983).
16. Lynch, G.R., et al., SLAC-250, 85 (1982).
17. Gabioud B., et al., IEEE TRANS. NUCL. SCI., 30, 1, 63 (1983).
18. Chen Chaoqing, selected articles from the Second High-Energy Experimental Physics Conference, 1983.
19. Benso, S., et al., NUCL. INST. METH., 187, 355 (1981).
20. Ibid., 217, 194 (1983).
21. CERN ALEPH Collaboration, Technical Report, 1983.
22. CERN DELPHI Collaboration, CERN/LEPC/83-3.
23. Osaki, S., Tristan project, invited talk presented at workshop on colliding beam physics, Beijing, 12-22 June 1984.
24. Hilke, H.J., NUCL. INSTR. METH., 217, 189 (1983).
25. Chapin, T.J., et al., Ibid., 197, 305 (1982).

3012/9365

CSO: 4008/74

SAFETY CONCEPT, SAFETY DESIGN OF SHIP NUCLEAR PROPULSION SYSTEM

Chengdu HE DONGLI GONGCHENG [NUCLEAR POWER ENGINEERING] in Chinese Vol 7 No 3, Jun 86 pp 33-38

[Article by Yen Jun [7346 0193]]

[Text] I. Introduction

The activities of nuclear-powered ships reach every port around the world; but today's technology cannot completely eliminate the possibility of an accident which would release radioactive materials into the environment. Consequently, the operational safety of a nuclear ship is an issue of world-wide concern. If the nuclear propulsion system is to become a reliable power source, not only must its utilization efficiency be improved, but the safety problem must be solved. The safety requirements of a land-based nuclear power plant generally need only be approved by the country using the power plant, but the safety requirements of a nuclear ship must be approved by a world organization. Therefore, a more stringent requirement must be imposed on the safety of nuclear propulsion systems; this requirement must be such that "the use of this system will not produce greater danger to the crew members, the passengers, and the environment than a ship using conventional propulsion system." Otherwise, nuclear ships may ultimately be forced out of the shipping business due to various limitations imposed on the design and operation in the name of safety.

This article briefly addresses several important problems that must be understood in carrying out the safety design of nuclear propulsion systems, the safety concept of nuclear-powered ships and the nuclear propulsion system, as well as the key methods used in safety design.

II. Safety Concept of Nuclear-Powered Ships

As a safety system, the "safety concept of nuclear-powered ships" is developed from a combination of the traditional safety concept of sea-going ships and the safety concept of nuclear power plants.

The traditional safety concept of sea-going ships is as follows: most disasters and accidents over the ocean produce primarily local consequences; they mainly endanger the ship itself, the ship crew and passengers, but have

very little effect on the general public and the environment. Therefore, the basic concept of treating conventional ship safety problems is "survival of the ship is the ultimate guarantee of the crew members' lives; protecting the ship from destruction means protecting the environment," i.e., "the ship's safety comes first." The guidelines derived from this concept for ship design and operation are: 1) minimize the probability of getting into an accident; 2) mitigate the consequences of a ship disaster and minimize the probability of ship destruction; 3) increase the rate of survival and the rate of rescue in case of a ship destruction and abandonment.

The basic concept of treating safety problems in nuclear systems is: "the nuclear reactor's safety comes first." It requires that "under normal operation or in case of an accident, the amount of radioactive materials released by the nuclear devices shall not exceed a level that will endanger the health of the residents or cause pollution to the environment." Therefore, in the design and operation of a nuclear facility, 1) we must minimize the probability of accident occurrence; 2) once an accident has occurred, we must first protect the reactor from being damaged; 3) if the reactor is damaged, we must do everything possible to prevent radioactive materials from being released into the environment.

From the above discussion, one can see that whether we adopt the nuclear safety concept or the traditional ship safety concept, the ultimate goal is to protect human lives and well-being, as well as properties and the environment. But there are two different approaches to achieve this goal: one insists that the safety of the nuclear reactor comes first, the other insists that the safety of the ship comes first.

The early designs of nuclear ships and their propulsion systems (e.g., the Savannah, the Otto Hahn, and the Luau) basically adopted both safety concepts and design guidelines. Specifically, the ship design followed the guidelines and standards established for ships powered by conventional fuels, and the design of nuclear propulsion system followed the guidelines and standards for large nuclear power plants.

However, using two different concepts simultaneously to guide the design and operation of a nuclear ship generally cannot produce the desired overall safety standards; under certain conditions it may even lead to handling errors. For example, consider a scenario where the ship is traveling in bad weather or through a dangerous zone in the ocean, and at the same time an accident has occurred which may cause damage to the reactor, using both safety concepts in this case will lead to a chaotic situation. If we follow the rule that reactor safety comes first and shut down the reactor, then the ship will lose power and begin drifting, thereby running the risk of striking a reef, running aground or even sinking; if we follow the rule that ship safety comes first and force the reactor to continue operation, then we run the risk of damaging the reactor or causing leakage of radioactive materials.

In recent years, a safety concept has evolved which considers the ship and its nuclear propulsion system as an integral unit; this concept is based on comprehensive studies of the safety concept of land-based nuclear power plants

and large ships and adopts the traditional approaches of handling the safety problem. It treats the nuclear ship as a "floating nuclear facility designed to carry out a special mission." This is the "nuclear ship safety concept," which requires that: "the design, construction and operation of a nuclear ship must meet the criterion that under all possible conditions, normal or abnormal, it shall not release radioactive materials which may cause damages to the crew members, the general public, or the environment. Under abnormal conditions, the first priority is to protect human lives."¹ Clearly, this emphasizes protection against radioactivity, but it has the implication that ship safety comes first, and that survival of the ship is the most important consideration in ensuring the ultimate safety of the reactor and preventing the leakage of radioactive materials. Using this concept to handle the relationship between ship safety and reactor safety, the following guidelines can be established:

1) The reactor is allowed to operate beyond its technical specifications or to suffer limited damage if it is judged to be necessary or beneficial for the overall safety of the nuclear ship. Because it is much safer for a ship to be powered by a slightly damaged (still controllable) nuclear propulsion system than to lose power and drift freely over the ocean.

2) If the ship is already beyond the point of salvageability, then from the point of view of preventing radioactive leaks, the reactor should be shut down. It is much safer to have the reactor safely shut down than to have a damaged reactor if the ship were to run aground or sink. This implies that the reactor is only allowed to be shut down under the following conditions: (a) the accident has completely damaged the reactor, thus power will be lost in any case; (b) even if power is available or the reactor can be forced to operate beyond its technical specifications, the ship will still sink or be destroyed by other means.

III. Safety Design of Nuclear Propulsion System

1. Important Factors in the Safety Design of Nuclear Propulsion System

The safety concept of nuclear ship does not imply that the safety of a ship reactor is not as important as that of a land-based nuclear power plant or need not be taken seriously, neither does it advocate the idea that the reactor can be forced to operate beyond its technical specifications or to operate in a mode which may be damaging to the reactor if the ship is not subject to any danger. On the contrary, this concept requires that other factors should be considered in designing a nuclear propulsion system; specifically, in addition to a comprehensive safety design nominally required for nuclear power plants, one should also consider the effects of the following factors.

(1) Possible sea disasters. They include collision, striking a reef, running aground, water leakage, sinking and fire. According to the statistics published by the Liverpool Insurance Co. on sea disasters of ships above 20,000 tons between 1949 and 1959² (Table 1), the probability of sea disaster that may endanger the reactor room is as high as 7×10^{-3} .

Table 1. Disasters That Occurred on Above 20,000-Ton Ships

<u>Type of disaster</u>	<u>Number of occurrences</u>	<u>Number of disasters that may endanger the reactor</u>
Fire	9	8
Collision	15	13
Running aground	19	11
Weather	3	2
Mechanical failure	5	0
Total	51	34

Note: For high-speed, large ships, the probability of encountering a disaster that may endanger the reactor is 0.007.

(a) The Effect of Collision and Striking a Reef and the Corresponding Protective Measures

A strong collision can damage the reactor, and also cause failure in the cooling system or other safety equipment, thereby creating a serious problem of radiation leakage. Therefore, a nuclear ship must be equipped with a special collision avoidance system and a highly reliable emergency cooling system; furthermore, the cabin layout and seal design must meet the sink-proof requirement.

There are two types of collision avoidance measures: active collision avoidance and passive collision avoidance. The active measure involves the installation of high-quality navigation instruments and various navigation systems to minimize the probability of collision caused by human error, the use of highly reliable propulsion system and control system to ensure that the nuclear ship will not lose its mobility under any circumstances, and the installation of emergency propulsion system to provide emergency propulsion for a sufficiently long time in case the main propulsion system is damaged. The passive measure is used to mitigate damages to the ship and the reactor in case of a collision. There are two types of commonly used passive collision avoidance structures: the deformable type structure and the rigid frame (with shock reducing device) type structure. The former relies on non-linear plastic deformation to achieve shock reduction, the latter relies on linear response to achieve shock reduction.³ In order to minimize the probability of failure of the emergency core cooling system due to collision, it has been suggested that 3-4 different emergency cooling systems should be installed, each with 100 percent capacity; furthermore, they should be located in cabins which are isolated from one another.

(b) Effect of Fire

Fire not only threatens the ship's survivability, but may also cause failure to the reactor protective system and the emergency cooling system, and lead to serious disaster. Fire prevention on a nuclear ship should be given special attention because unlike a land-based power plant, external assistance

is generally not available. Fire prevention measures include various techniques for preventing water loss, cabin isolation, fire detection and prediction and a reliable fire extinguishing system.

(c) Effect of Water Entering in the Ship Cabin

When water enters in the ship cabin, the emergency power supply, the reactor protective system, and various safety equipment may all be adversely affected.

(2) Loss of Mobility

We must fully realize the serious consequences that once the nuclear propulsion system stops working, the ship will lose its mobility which may lead to destruction of the ship as well as the nuclear propulsion system. For this reason, the nuclear propulsion system must be designed with much higher reliability than a land-based power plant. In addition, to ensure the overall safety of the ship when it is traveling under dangerous conditions, the propulsion system may be required to operate beyond its technical specifications or to operate at the risk of being slightly damaged. Therefore, the design safety margin of the propulsion system should be sufficiently high.

(3) Effect of Other Factors

(a) We must realize that because of the limited space on a ship, it is not possible to install a safety system as sophisticated and as large as that of a land-based power plant. Consequently, we should not and cannot use the safety measures of nuclear power plants to achieve the safety standards of nuclear ships.

(b) The ship has limited resources for handling an accident; in general it cannot rely on external assistance.

(c) The living conditions on a ship are far inferior than those on land; hence the mental conditions of ship reactor operators are generally not as sound as their counterparts working in a land-based power plant, and the possibility of human-induced accident is greater.

(d) Because the possible combinations of ship disasters and nuclear accidents, the probability of occurrence, the resulting consequences, the method of control, and the ultimate social risks are all difficult to predict, in practice it is impossible to implement a perfect emergency plan. Therefore, the ultimate authority to allocate safety measures between the ship and the reactor should be reserved for the captain, who has the best knowledge about the nature and seriousness of the accident, the development process, and the possible social risks.

2. Ways To Improve the Safety of Nuclear Propulsion System

The "In-Depth Defense" method used to prevent accidents from occurring in land-based reactors can also be used in the safety design of ship reactors. Generally, such a defense system contains three layers of defense.

The first line of defense is to prevent accidents from occurring by minimizing the probability of malfunctions and errors that may cause accidents. The important technical guidelines include the following: 1) the design, construction and management of each system must strictly comply with very high standards; 2) the design malfunction rate and failure rate of each system must be extremely low; 3) all systems and equipment must have high degree of tolerance for operator errors; 4) all materials and components must be thoroughly tested; and 5) all monitoring and control systems should have sufficient margin.

The second line of defense is to prevent a minor malfunction or error from developing into a major accident. The key approach is to maintain safe operation of the reactor or to execute safe reactor shutdown in case of an operator error or equipment malfunction. The practical measures to carry out this mission include the following: 1) provide multi-channel electric power supply for the nuclear facility; 2) install a sensitive detection system that can identify a damaged housing of the fuel elements or broken pressure boundary of the cooling system; 3) install an automatic or manual system that can shut down the reactor based on information obtained from various detection systems.

The third line of defense is to prevent radioactive materials from being scattered into the environment once a major accident has already occurred. The key measures for accomplishing this task include the following: 1) a sealed "safety container" for isolating the nuclear island, on a ship there is also a safety isolation cabin; 2) an emergency cooling system; 3) a heat removal system in the safety container; and 4) a system inside the safety container for disposing radioactive materials.

Because of the various considerations mentioned above, the relative emphasis for the different lines of defense and the actual implementation of the safety concepts and measures for a ship nuclear propulsion system differ from those of a land-based nuclear power plant. For example, because of the possibility of collision and water leakage, the probability of loss of power is much higher for a nuclear propulsion system than for a land-based power plant; because of the limited space on a ship, it is not possible to install a sophisticated safety system, hence the probability of failure of the system is higher. Consequently, we cannot rely on the second and third lines of defense to ensure the propulsion system's safety; rather, we should strive to strengthen the first line of defense, i.e., minimizing the probability of accident occurrence and increasing the reactor's own ability to guard against accidents, in other words, increasing the reactor's inherent safety.

The inherent safety of a reactor can be improved by using the following approaches: 1) Using reliable fuel elements and increasing the thermodynamic and hydrodynamic design margin, e.g., using low-temperature and low heat capacity fuel elements (increasing the surface area to fuel volume ratio), lowering the surface thermal loading of the elements, and lowering the running parameters of the heat-carrying agents. 2) Using a more reliable, reserve-reactivity control technique, so that reserve reactivity is introduced gradually as the fuel is being burned up. This technique reduces the

use of control rods, and therefore reduces the probability of accidents due to control rod failure. The best technique is to use a solid diffusion type burnable poison for reactivity control. This technique not only provides high reserve reactivity, but occupies no heat-release surface area; with the proper design, even cold sea water can enter the reactor core without causing critical accidents. 3) Increasing the natural circulation of the primary circuit, thus reducing or eliminating the requirement for external emergency cooling system in case of an accident. A good design will provide a certain level of output power for emergency propulsion.

IV. Safety Analysis of Nuclear Propulsion System

Because the mission and operating environment of a nuclear propulsion system are different from those of nuclear power plant, the operational conditions and accidents encountered by the two systems are also different. Therefore, different procedures are used for safety analysis and evaluation. Ref. 4 presents a method for classifying the types of operational conditions and gives a description of each of the conditions. The bases for classifying operational conditions are the frequency of accident occurrence, the possible consequences, and the degree of difficulty for recovery. In consideration of the unique features of ship accidents, the operational condition IV is further divided into two sub-conditions IV A and IV B (Table 2).

Table 2. Bases for Classifying the Operational Conditions of Nuclear Propulsion Systems

Operational condition	I	II	III	IV
Illustration	Normal operation	Minor accident	Major accident	Serious accident
Frequency of occurrence	Continuous or frequent (many times/year)	Infrequent (once/year)	Rare	Extremely rare (10 ⁻⁷ /year)
Consequence classification	1	2	3	4
Consequence treatment	Possible reduction in power	Reduction in power or reactor shutdown	Fast shutdown plus residual heat removal	Fast shutdown plus emergency cooling or residual heat removal
Restarting	Immediate	After repair	After dock repair	Not possible
Release of radio-activity	Less than normal limiting value			Less than accident limiting value

Note: Operational condition IV can be divided into two categories: IV A is the case with design power supply; IV B is the case without design power supply.

The definition of consequence classification in Table 2 is as follows:

Consequence level 1: the level of radioactivity of the ship and its steam supply system is within the specified limits for normal operation.

Consequence level 2: it is caused by an accident, but operation of the ship is not seriously affected, and the level of radioactivity is lower than the allowable radiation level for reactor technicians.

Consequence level 3: it is caused by single or multiple accidents; the ship structure or propulsion system is damaged, and there are human injuries; the ship is partially put out of service and requires external assistance, but the level of radioactivity does not exceed the allowable radiation dosage for reactor technicians.

Consequence level 4: it is caused by single or multiple accidents; it may lead to death of personnel and sinking of ship, but the level of radioactivity in the hull and on the deck above the reactor does not exceed twice the allowable radiation dosage for reactor technicians.

Table 3 presents detailed descriptions of the four classes of operational conditions. The purpose of safety analysis is to provide quantitative answers to the consequences of these operational conditions and accidents.

Table 3. Examples of Classification of Operational Conditions of a Nuclear Propulsion System

Classification of operational conditions	Name of operational conditions
I (normal)	Starting, stopping, low-power operation, full-power operation, variable load, regular maintenance, bad weather, loading and unloading cargos, refueling, and overload operation, which has already been considered in the design and operation procedures.
II (infrequent minor accidents)	Component failures or errors which lead to loss of power or loss of mobility; e.g., sudden shutdown of generator, sudden shutdown of a main engine, sudden shutdown of a condenser, cut-off of sea water cooling unit, cut-off of water supply, shut-off of main steam valve, malfunction in the main electric system, malfunction in the steering mechanism or anchoring mechanism; accidental starting of main coolant pump or water pump, primary operator error, malfunction in the reactor protective system or safety system, error in operating the pressure relief valve or safety valve of the primary system, accidental withdrawal of control rod, temporary power outage, and minor leak in the primary system.

[Continued on following page]

Classification of
operational
conditions

Name of operational conditions

III (rare occurrence)	Leaks in the primary circuit pressure boundary which does not cause pressure drop in the primary circuit but requires activation of the emergency cooling system and safety shield for isolation; leaks in the radioactive waste treatment system and storage system; leakage of primary water into the secondary system, which requires reactor shutdown; malfunction in the control rod drive mechanism; jammed control rod; malfunction in the forced circulation system of the primary circuit; malfunction in the water supply system of the secondary circuit; exhaust from the primary system; malfunction in the coolant supply system in the docks; striking a reef with no damage to the ship integrity and no loss of coolant; collision which causes water leakage between two neighboring cabins; fire or explosion with no serious damage to the reactor room; fire in the machine room or operations room; unusually bad weather along the designated course.
IV A (rare occurrence of extreme accidents)	Loss of water accident; destruction of the waste storage tank; striking a reef, which may cause tilting of the ship and intermittent loss of coolant, but still maintain integrity; extremely bad weather; ejection of control rod; running aground, which can cause partial damage to ships with large, double-layered bottoms or ships with long hulls; collision which causes fire or explosion.
IV B (rare occurrence of extreme accidents)	Capsizing; ship sinking in deep or shallow waters, causing failure in emergency power supply system.

V. Concluding Remarks

We see from the previous discussions that nuclear ship is a unique system which has the technical and safety problems of both the shipping industry and the nuclear power industry. In view of the public's concern about nuclear safety, this system should be considered as a "floating nuclear facility with a special mission." The ultimate goal of safety measures should be to prevent radiation damages, but we must assign first priority to the survival of the ship and establish an overall nuclear ship safety concept.

In case there is a conflict between reactor safety and ship safety, the overall system safety should be the ultimate guideline. Unless the reactor is completely damaged or it will destruct even if the ship is still under power, the reactor should continue operation.

Because a ship disaster and a reactor failure affect one another, an accident in either will lead to very grave consequences. Therefore, the safety requirement for a nuclear ship and its propulsion system should be higher than that for a ship with conventional power or a nuclear power plant. The key approach to improving the safety of a nuclear propulsion system is to improve the safety of the reactor itself. The safety procedures of a nuclear propulsion system cannot simply be copied from those used for nuclear power plants; they should be determined by careful study of the particular ship application.

Since one cannot predict every type of accidents and establish protective measures to guard against all possible combinations of potential problems, the ultimate authority to allocate safety measures between the ship and the reactor should be reserved for the captain, who has the best understanding of the seriousness of the accident, the development process and the possible consequences.

It should be pointed out that the analyses presented in this article are primarily aimed at nuclear-powered commercial ships. For a military vessel, the effect of mission safety (which is often more important than the safety of the propulsion system) should also be analyzed; but the final result is similar.

3012/6091
CSO: 4008/90

PULSE CALIBRATION TECHNIQUE OF X-RAY DETECTOR

Beijing WULI XUEBAO [ACTA PHYSICA SINICA] in Chinese Vol 35 No 7, Jul 86
pp 864-873

[English abstract of article by Sun Jingwen [1327 2529 2429] of the Southwest
Institute of Fluid Physics, Chengdu]

[Text] A pulsed CuK X-ray source with flux intensity 10^{18} - 10^{19} K X-rays per sr per s has been produced using the high current electron beam technique. It has been employed to calibrate the response of the silicon PIN diode detector to pulsed X-ray photons. An absolute X-ray monitor, a P10 gas pulse ionization chamber, has been used as a standard for the pulsed X-ray flux density. The automatic pulsed charge measuring instrument is controlled and corrected in real time by a microcomputer. The measured uncertainty of the flux density is ± 5 percent. This chamber is suitable for the energy flux rate range of $4 \times 10^{-9} - 2 \times 10^2$ W/cm² and the photon energy range of 1.5 - 10 keV. The calibrated accuracy of the detector is ± 7.0 percent. It is found that the pulsed sensitivity of the silicon PIN diode is about 30 percent higher than the sensitivity calibrated by steady X-ray beams.

STABLE REGION OF TOKAMAK DEVICE FEEDBACK CONTROL (I). THEORETICAL

Beijing WULI XUEBAO [ACTA PHYSICA SINICA] in Chinese Vol 35 No 7, Jul 86
pp 874-881

[English abstract of article by Zheng Shaobai [6774 1421 4101] and Shen
Zhongqing [3088 0112 0615] of the Institute of Physics, Chinese Academy of
Sciences]

[Text] In this paper, the evolution equations of feedback control of plasma
current and horizontal displacement simultaneously in a tokamak device are
presented. Under the assumption of slight disturbance and linear approxima-
tion, the stability criterion and the stable region of the CT-6B tokamak
feedback control are given.

STEADY-STATE ELECTRIC FIELD STRUCTURE AND DENSITY PROFILE IN A PLASMA
IRRADIATED BY DOUBLE-FREQUENCY LASER

Beijing WULI XUEBAO [ACTA PHYSICA SINICA] in Chinese Vol 35 No 7, Jul 86
pp 882-888

[English abstract of article by Zhu Shitong [2612 5535 6639] of Shanghai
Institute of Optics and Fine Mechanics, Chinese Academy of Sciences; and
Shen Wenda [3088 2429 6671] of the Department of Physics, Shanghai University
of Science and Technology]

[Text] The analytic expressions for steady-state electric field intensity
and local scale length in a plasma irradiated by a double-frequency laser are
derived. It is shown that the ponderomotive force due to the double-frequency
laser field would lead to the local density dip near the critical surface and
the anomalous increase and fluctuation of the critical scale length in some
region of field intensity value.

COMPARISON OF TWO COLLISION MODELS IN PLASMA

Beijing WULI XUEBAO [ACTA PHYSICA SINICA] in Chinese Vol 35 No 7, Jul 86
pp 947-952

[English abstract of article by Zhang Chengfu [1728 2110 4395] of the
Department of Physics, Beijing University]

[Text] In this paper, the effects of collision on the dispersion equation of plasma are discussed for two kinds of collision models (the BGK model and the LB model). Analysis shows that the main effect of collision is to change the usual dispersion function $Z(\xi)$ into a generalized one $W(\xi, \bar{\nu})$. The properties of the W function have been analyzed and compared for the two models. The effects of collision on the low frequency drift wave (local mode) and ion-acoustic wave are discussed. It is shown that the LB model is not only more reasonable physically than the BGK model, but also simpler in calculation and expression.

9717

CSO: 4009/113

ELECTRONMICROSCOPIC IMMUNOFERRITIN TECHNIQUE AND ITS APPLICATION

Shijiazhuang ZHONGHUA WULI YIXUE ZAZHI [CHINESE JOURNAL OF PHYSICAL MEDICINE] in Chinese Vol 8 No 2, 25 Jun 86 pp 88-90

[English abstract of article by Yu Chengzhi [0151 3397 0037] of the Institute of Microbiology and Epidemiology, Academy of Military Medical Sciences, Beijing]

[Text] Immunoferritin indirect staining of ultrathin sections in electron microscopy was established on BHK-13 cells infected with Sindbis virus. The author observed HFRS virus particles isolated in Vero E-6 cells from a patient with HFRS using this method. In addition, this method has been successfully applied to the observation of the surface structure of the Jinghe strain of spotted fever rickettsiae in the yolk sac section which could not be detected with ordinary electron microscopy. (Paper received April 1985.)

REFERENCES

1. Morgan C. The use of ferritin-conjugated antibodies in electron microscopy. *Int Rev Cytol* 1972; 32:291.
2. Sternberger LA. Immunoferritin and Immunocytochemical methods, in *Immunocytochemistry* 2th ed, New York: John Wiley & Sons, 1979:59.
3. 施谓康, 等. 铁蛋白标记抗体技术及其对细胞表面抗原定位的应用. *生物化学与生物物理进展* 1975; 4:8.
4. Siess E A simple method for the preparation of pure and active r-globulin-ferritin conjugates using glutaraldehyde. *Immunology* 1971; 20:659
5. Otto H. A two stage method for cross-linking antibody globulin to ferritin by glutaraldehyde. Comparison between the one-stage and two-stage method. *J Immunol meth* 1973; 3:137.
6. 贺师麟. 免疫电子显微镜技术. 北京医学院微生物学教研组编: 实验免疫学, 第一版, 北京: 人民卫生出版社, 1981:286.
7. Mclean IW, Nakane PK. Periodate-Lysine-Paraformaldehyde fixative. A new fixative for immunoelectron microscopy. *J Histochem Cytochem* 1974; 22:1077.
8. Ellis DS. Congo/Crimean hemorrhagic fever virus from Iraq 1979:1. Morphology in BHK-21 cells. *Arch Virol* 1981; 70:189.
9. 余澄之, 等. 从病人分离的肾综合症出血热(HFRS)病毒的形态学研究. *中华流行病学杂志* 1985; 6(2): 119.
10. Silverman DJ. External layers of rickettsia prowazekii and rickettsia rickettsii: Occurrence of a slime layer. *Inf Immunol* 1978; 22:233.
11. 余澄之, 等. 斑点热立克次体的表面结构(摘要). *电子显微学报* 1984; 3(3):52.

RATE-CONTROLLED LIQUID NITROGEN COOLING EQUIPMENT

Shijiazhuang ZHONGHUA WULI YIXUE ZAZHI [CHINESE JOURNAL OF PHYSICAL MEDICINE] in Chinese Vol 8 No 2, 25 Jun 86 pp 93-96

[English abstract of article by Wan Guoying [8001 0948 2019], et al., of the Academy of Military Medical Sciences]

[Text] A rate-controlled cooling apparatus has been reported. It can be used for freezing bone marrow cells, blood cells, hematopoietic cells of embryonic liver, cornea and skin, etc. After cryopreservation of cells, the cell viability is more than 80 percent. The equipment consists of three parts: (1) a program-controller; (2) a system for storage and transfer of LN₂; (3) a freezing chamber. There are seven cooling rates in the equipment. Start-freezing temperature and end-freezing temperature can be adjusted continually and chosen freely. The cooling rate is controlled automatically during the freezing process. The temperature of the freezing sample and in the freezing chamber is shown digitally. The equipment is applicable to cryobiological research and cryopreservation of biological materials. (Paper received 1 February 1985.)

REFERENCES

1. Mazur P and Schmidt J J. Interactions of cooling velocity, temperature, and warming velocity on the survival of frozen and thawed yeast. *Cryobiology* 1968, 5(1):1.
2. Mazur P, et al. A two-factor hypothesis of freezing injury. *Exp Cell Res* 1972, 7(2):345.
3. Leibo S P, et al. Factors affecting survival of mouse embryos during freezing and thawing. *Exp Cell Res* 1974, 89(1):79.
4. Cavins J A, et al. Recovery of lethally irradiated dogs following infusion of autologous marrow stored at low temperature in dimethyl-sulphoxide. *Blood* 1962, 20(6):730.
5. Leibo S P and Mazur P. The role of cooling rates in low-temperature preservation. *Cryobiology* 1971, 8(5):447.
6. Kelley F D, et al. Controlled-rate liquid N₂-microwave biological freeze-thaw device. *Cryobiology* 1982, 19(4):372.
7. 万国应. 半导体PN结在测温应用中的性能分析. *医疗技术* 1984, 12:21.

9717

CSO: 4009/1005

POSITRON EMISSION TOMOGRAPHY---A NEW NUCLEAR MEDICINE TECHNIQUE

Shanghai ZIRAN ZAZHI [NATURE JOURNAL] in Chinese Vol 9 No 4, Apr 86 pp 269-271

[Article by Yu Renkang [0205 0088 1660], Jiaotong University, Shanghai]

[Abstract] PET stands for positron emission tomography, which merges the biochemical evaluation of pathology in early nuclear medicine methods with the reconstructed precise positioning using computer graphics. There are many unique features in medical diagnosis and physiological research; therefore, research on its clinical applications is vigorously under way in West Europe and the United States. Research on PET will widely develop in China with the radioactive-isotope technique and computer tomography. This paper presents the fundamental principle of PET and its tracers. The PET system requires a medical cyclotron and the corresponding chemical equipment, a detector array for receiving gamma photons, and a computer. Cooperation is required among personnel specialized in physics, chemistry, computer, physiology, and medicine. More than 40 PET research centers have been established throughout the world. The author saw a PET model IV system at the Medical College of the University of Washington in the United States. The system was jointly developed by the university and a private company. The PET system can be used to examine the human head and trunk. In the newer-generation PET system, an important research direction is the addition of photon transition-time data in the graphic reconstruction process. This requires an accurate measurement of time difference of two trapped photons between their arrivals at the receiver in order to enhance the signal-to-noise ratio and the graph's resolving power. PET's development prospects are promising in biology and medicine. Five figures show gamma photons picked up by a ring-shaped detector, a positron transmission source at the intersection of a group of straight lines, a projection-recording radioactivity distribution, wave filtration, and the reconstruction of radioactive distribution with an inverse projection.

10424/6091

CSO: 4009/1056

STUDY OF THE CHARACTERISTICS OF PATHS IN Ar_2F^* FORMATION PROCESSES*

Shanghai GUANGXUE XUEBAO [ACTA OPTICA SINICA] in Chinese Vol 6 No 8, Aug 86
pp 679-687

[English abstract of article by Gu Zhiyu [7357 0037 3768], et al., of Anhui
Institute of Optics and Fine Mechanics, Chinese Academy of Sciences, Hefei]

[Text] The kinetic processes in Ar/He/ F_2 mixtures excited by fast discharge
have been analyzed. A mathematical description, which could reveal the
characteristics of paths in the kinetic processes, is given based on a sim-
plified kinetic model. Characteristics of paths in Ar_2F^* formation processes
are studied by comparing the experimental data with the results of numerical
calculations. (Received 28 February 1985; revised 31 January 1986.)

* Supported by the Science Fund of the Chinese Academy of Sciences.

OFF-RESONANT-PUMPING AC STARK EFFECT IN OPTICALLY PUMPED FIR LASER

Shanghai GUANGXUE XUEBAO [ACTA OPTICA SINICA] in Chinese Vol 6 No 8, Aug 86
pp 688-694

[English abstract of article by Lin Yikun [2651 6318 1024], et al., of the
Department of Electronics, Zhongshan University, Guangzhou]

[Text] The interactions among R_{35} , T_{34} and S_{54} processes in a six-level system have been studied. Near the cross point of the resonant curves of these processes in the multiphoton resonance diagram of the six-level system, such interactions should be very strong. We found theoretically that in the case of off-resonant-pumping, the interactions among these multiphoton processes should also lead to splitting of the laser spectral line, which is called the off-resonant-pumping AC Stark effect. Because the influences of the saturation effect and electric dipole transition enhancement effect were not the same for different multiphoton processes, contributions of different multiphoton processes to the off-resonant AC Stark effect could be distinguished by the injection of the FIR signal into the system. (Received 7 October 1985; revised 4 February 1986.)

NEW METHOD FOR ON-RESONANT TWO-PHOTON ABSORPTION SPECTROSCOPY

Shanghai GUANGXUE XUEBAO [ACTA OPTICA SINICA] in Chinese Vol 6 No 8, Aug 86
pp 708-713

[English abstract of article by Zhu Zhenhe [2612 2182 0735] of the Department of Mathematics and Physics, Central Nationalities Institute, Beijing]

[Text] A new experimental method for on-resonant two-photon absorption spectroscopy is presented in this paper. The experimental set-up is the same as that of the two-photon fluorescence experiment used in measuring durations of ultrashort laser pulses. A picosecond laser pulse is divided into two beams which then travel in opposite directions in the sample. The signal intensity measured along the laser trace will be a wide plateau overlapped by a narrow peak. The ratio of the on-resonant two-photon absorption section to the two-step single-photon absorption section can be deduced from the contrast ratio of the peak intensity to the shoulder intensity. The theoretical calculation shows that this method is valid for various cases. (Received 2 August 1985; revised 13 February 1986.)

GROWTH AND CHARACTERISTICS OF ALEXANDRITE CRYSTALS

Shanghai GUANGXUE XUEBAO [ACTA OPTICA SINICA] in Chinese Vol 6 No 8, Aug 86
pp 734-743

[English abstract of article by Ma Xiaoshan [7456 4562 1472], et al., of
Shanghai Institute of Optics and Fine Mechanics, Chinese Academy of Sciences]

[Text] The opaque sample and transparent alexandrite crystals have been analyzed by different techniques, such as the fluorospectrometer, X-ray fluorospectrometer and ESCA. The measured data support the authors' previous suggestion concerning the formation mechanism of Lienard's "melt aging." It follows that the transparent crystal can be grown with good reproducibility.

Inclusions and dislocations in the crystals have also been investigated, leading to the growing of high quality alexandrite crystals. The optical homogeneity of laser rods is $0.25\lambda/\text{in}$ to $0.40\lambda/\text{in}$ and is free from scattering centers. The laser threshold is 34.1J. The line width is 0.01Å after Q-switch with a color center crystal.

The annealing effect pressure effect of R_1 and R_2 fluoroline and striations in alexandrite crystals have also been studied. (Paper received 19 December 1985; revised 28 February 1986.)

A PICOSECOND GaAs PHOTOCONDUCTIVE SWITCH

Shanghai GUANGXUE XUEBAO [ACTA OPTICA SINICA] in Chinese Vol 6 No 8, Aug 86
pp 744-747

[English abstract of article by Zhu Shidong [2612 0013 2767], et al., of
Changchun Institute of Optics and Fine Mechanics, Chinese Academy of Sciences]

[Text] The development of a picosecond GaAs photoconductive switch is reported. The switch consists of a microstrip transmission line formed on Cr-doped semi-insulating GaAs with a small gap ($\sim 20 \mu\text{m}$) in the stripline. As the source of optical pulses used for preliminary evaluation of the switch, a synchronously pumped Rh6G dye laser was used. The rise time of the signal observed on a sampling oscilloscope was 120 ps and the FWHM was 230 ps. We measured the dependence of peak voltage of the switch electric pulse on the energy of the incident laser pulse for a bias voltage of 30 V and incident energy range of 38 pJ \sim 320 pJ. (Received 9 January 1986; revised 13 February 1986.)

9717

CSO: 4009/1

APPLICATION OF MONTE CARLO METHOD IN RADIATIVE HEAT TRANSFER

Shanghai ZIRAN ZAZHI [NATURE JOURNAL] in Chinese Vol 9 No 4, Apr 86 pp 250-254

[Article by Bian Bohui [0593 0130 4940] and Li Hao [2621 3185] of Qinghua University]

[Abstract] The Monte Carlo method relies on random variable statistical testing to solve problems in mathematics, physics, and engineering technology. For nearly 100 years this random simulation method has a history of use in approximate numerical calculations. In its early history, however, there were limitations in simulation-testing tools; relatively few practical problems could be solved. In the past 2 decades, what with the rapid progress in computer technology, propitious conditions were provided for the Monte Carlo method. Gradually, the method is being applied to the problem of calculating radiative heat transfer, as illustrated in five figures. To a great extent, the method's accuracy depends on the number of sampling values of the random variables in the simulation. The more the sampling values in the random variables, the higher the accuracy. Therefore, the method demands a large storage capacity in the computer used; this is a drawback of the method. However, the result accuracy in random simulation is not related to the number of dimensions; thus, the method is suitable to calculating multi-dimensional and complex problems. The basic features of the method are as follows: First, the surface radiative heat energy is considered as composed of a large number of energy beams (possessing the same energy for each beam) emitted from the surface. The random emission process of each energy beam is traced until its absorption by the surface or its emission into the ambient space. Finally, the number of energy beams absorbed by each surface is statistically determined; this is the radiative heat transfer between surfaces. According to References 2 through 4, the Monte Carlo method can also be used in calculating gas radiation. One table shows a comparison between radiation transfer coefficients and radiation angle coefficients; in the calculation, the total number of energy beams is 10,000.

10424/6091

CSO: 4009/1056

END